Master of Science Thesis

Residual-based variational multiscale modeling in a discontinuous Galerkin framework

K.F.S. Stoter

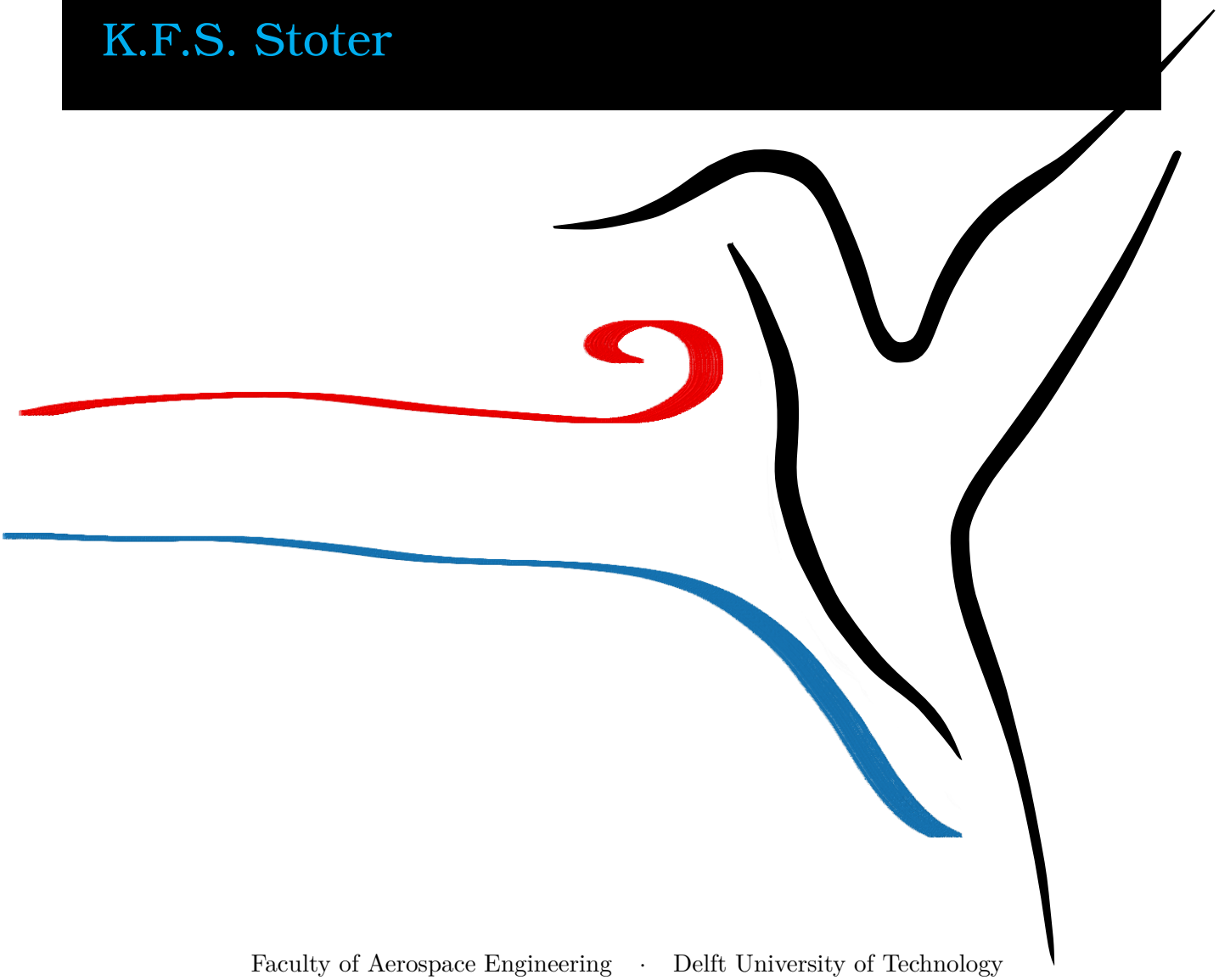

Faculty of Aerospace Engineering · Delft University of Technology

TU Delft Delft University of Technology

Residual-based variational multiscale modeling in a discontinuous Galerkin framework

Master of Science Thesis

For obtaining the degree of Master of Science in Aerospace Engineering
at Delft University of Technology

K.F.S. Stoter

29th June 2017

Faculty of Aerospace Engineering · Delft University of Technology

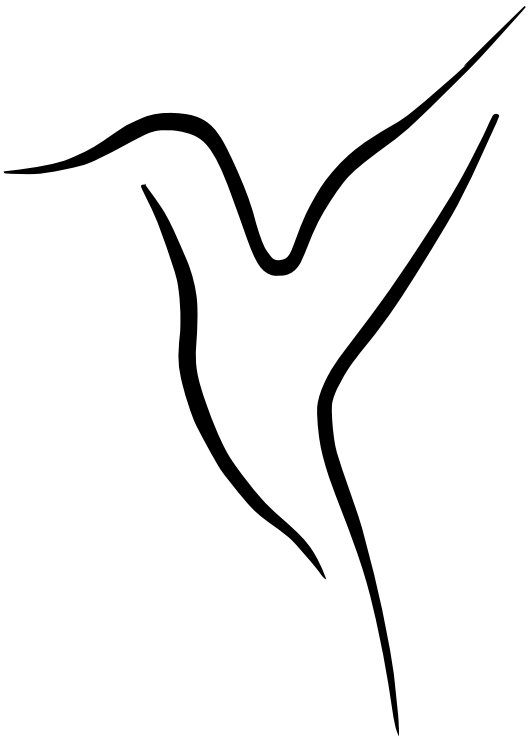

TU Delft Delft University of Technology

Delft University of Technology
Faculty of Aerospace Engineering
Department of Aerospace Structures and Materials

GRADUATION COMMITTEE

Dated: 29th June 2017

Committee chair:

Dr. S.R. Turteltaub

Committee members:

Dr. S.J. Hulshoff

Dr. R.P. Dwight

Dr. D. Schillinger

Abstract

In this work the residual-based variational multiscale method is presented in a discontinuous Galerkin framework. This so-called 'DG-RVMS' strategy is developed, extensively verified, and tested on a more complex case.

The proposed DG-RVMS paradigm consists of three principle components. First, the per-element weak form is coupled by manipulation of the fine scale element boundary terms. Next, a fine scale surface model is introduced to make the global coarse scale weak formulation well posed. Finally, the coarse scale jumps and residual can be leveraged to formulate a new volumetric fine scale model. This volumetric fine scale model incorporates the fine scale effects onto the coarse scale solution.

The verification efforts will focus on a number of 1D test cases, concerning linear differential equations. In particular the Poisson equation and an advection-diffusion problem will be investigated. Within a controlled environment the finite element solution can be manipulated at will, by using explicit expressions for the fine scale terms. As an example the H^1 and L^2 projections of an exact solution are recollected. Each term in the obtained multiscale formulations will be verified by means of these numerical experiments.

Additionally, the multiscale principles will serve to develop fundamentally new insights into the nature of known discontinuous Galerkin formulations. It will be shown that classical formulations, such as the well known interior penalty method, can be interpreted as a specific fine scale model. It will also be shown that upwind numerical fluxes serve as an impromptu solution for the lack of a volumetric fine scale model.

Finally, the DG-RVMS framework will be utilized for a more complex partial differential equation. Thereby its effectiveness as a multiscale model can be assessed. For this purpose the nonlinear transient Burgers equation will be considered. Numerical experiments will consistently show a near order of magnitude decrease in the error in total solution energy. The experiments will make use of discretizations of polynomial order $p = 2$ to $p = 4$. The increase of performance is observed for all polynomial orders, and for the complete range of degrees of freedom in the convergence study.

Table of contents

List of figures

List of tables

Glossary

Acronyms

Symbol	Description
CFD	Computational fluid dynamics
CG	Continuous Galerkin
DG	Discontinuous Galerkin
DNS	Direct numerical simulation
Dof(s)	Degree(s) of freedom
FFT	Fast Fourier transform
HDG	Hybridizable discontinuous Galerkin
IP	Interior penalty
LDG	Local discontinuous Galerkin
LES	Large-eddy simulation
NIPG	Nonsymmetric interior penalty Galerkin
NURBS	Non-uniform rational B-spline
PDE	Partial differential equation
R-VMS	Residual-based variational multiscale
RANS	Reynolds-averaged Navier-Stokes
RK	Runge-Kutta
VMS	Variational multiscale

Latin symbols

Symbol	Description	Reference
a	Advection vector (multi-D) or velocity (1D).	Eq. (3.51)
$B(\cdot\,,\cdot\,)$	Bilinear form of the respective PDE.	Eq. (2.5)
C_1, C_2, C_3	Coefficients for the construction of τ, γ_0 and γ_0.	Eq. (4.38)
d	Arbitrary distance.	–
E_{tot}	Total energy in the solution.	Eq. (4.7)
$E(k)$	Spectral energy density.	Eq. (4.8)
f	Body force.	Eq. (3.18)

$g(x, y)$	Green's function of some PDE.	Eq. (2.11)
$g'(x, y)$	Fine scale Green's function.	Eq. (2.12)
h	Element width.	–
K	An element volume or reference.	Tab. 3.1
∂K	Boundary of element K.	Tab. 3.1
k	Wave number.	Eq. (4.8)
$\mathscr{L}$	Differential operator associated to the respective PDE.	Eq. (3.21)
$\mathscr{L}^*$	Adjoint differential operator of $\mathscr{L}$.	Eq. (3.23)
$L(\,\cdot\,)$	Linear form of the respective PDE.	Eq. (2.5)
$\overline{\mathscr{M}}$	Coarse scale finite element space of $\mathbb{Q}$.	Eq. (4.9)
$\tilde{\mathscr{M}}$	Intermediate scale finite element space of $\mathbb{Q}$.	Eq. (4.9)
$\mathscr{M}'$	Fine scale finite element space of $\mathbb{Q}$.	Eq. (4.9)
N	Number of elements.	–
n	Normal vector.	Eq. (3.10)
$\mathscr{P}$	A projector onto the coarse scale space $\mathscr{P} : \mathscr{V} \to \overline{\mathscr{V}}$.	Eq. (2.13)
p	Polynomial degree of coarse scale basis functions.	Eq. (3.2)
p, q	Dummy functions.	–
$\mathbb{Q}$	Function space of continuous functions.	Eq. (3.2)
$\bar{\mathbb{Q}}$	Sufficiently smooth coarse scale components of $\mathbb{Q}$.	Eq. (3.2)
$\mathbb{Q}'$	Function space of fine scale components of $\mathbb{Q}$.	Eq. (3.2)
Q	Space-time domain.	Tab. 4.1
Q^n	Space-time slab.	Tab. 4.1
Q_K^n	Space-time element domain.	Tab. 4.1
$\mathscr{R}$	Residual of some solution.	Eq. (2.9)
$\mathscr{T}$	Computational mesh. The set of elements.	Tab. 3.1
u	Solution variable. Exact solution.	Eq. (2.3)
$\bar{u}$	Coarse scale solution.	Eq. (2.3)
$\tilde{u}$	Intermediate scale solution.	Eq. (4.10)
u'	Fine scale solution.	Eq. (2.3)
u_h	Approximate coarse scale solution. Finite element solution.	Eq. (4.18)
u_D	Dirichlet boundary condition.	Eq. (4.18)
$\mathscr{V}$	Function space of element-wise discontinuous functions.	Eq. (3.4)
$\overline{\mathscr{V}}$	Function space of coarse scale components of $\mathscr{V}$.	Eq. (3.4)
$\mathscr{V}'$	Function space of fine scale components of $\mathscr{V}$.	Eq. (3.4)
w	Test function.	Eq. (2.4)
$\bar{w}$	Coarse scale test function.	Eq. (2.4)
$\tilde{w}$	Intermediate scale test function.	Eq. (4.10)
w'	Fine scale test function.	Eq. (2.4)

Greek symbols

Symbol	Description	Reference
α_i	A Runge-Kutta time integration coefficient.	Tab. 4.2
$\beta_{i,j}$	A Runge-Kutta time integration coefficient.	Tab. 4.2
χ	Space constant part of the element space-time domain Q_K^n.	Eq. (4.34)
ε	Perturbation series factor.	Eq. (2.9)
ϵ	Infinitesimal distance.	–
η	Penalty factor of the IP or NIPG method.	Eq. (3.36)
Γ	Sum of element boundaries.	Tab. 3.1
γ_0, γ_1	Element averaged surface Green's function.	Eq. (A.10)
ν	Viscosity or diffusion coefficient.	Eq. (3.51)
ν_T	Eddy viscosity.	Eq. (4.13)
Ω	Space domain of definition of the PDE.	Tab. 3.1
$\partial\Omega$	Boundary of the domain Ω.	Tab. 3.1
Ω_E	Sum of element interior volumes.	Tab. 3.1
Φ	Fine scale surface model for the average of u'.	Eq. (3.14)
τ	Element averaged volumetric Green's function.	Eq. (A.9)
Θ	Fine scale surface model for the average of $\nabla u'$.	Eq. (3.14)
Υ^n	Time constant part of the element space-time domain Q_K^n.	Eq. (4.34)

Chapter 1

Introduction

The residual-based variational multiscale (R-VMS) method is an approach for incorporating the effect of the unresolved *fine scale* solution onto the computational *coarse scale* solution [1, 2]. For many problems in physics and engineering, the multiscale nature of the problem is of fundamental importance to the behavior of the global system [3–7]. For such problems, the R-VMS method helps improve the stability and accuracy of the numerical scheme [8]. Typical examples are advection based partial differential equations. The general strategy is to split the weak formulation of the partial differential equation into its fine scale and its coarse scale components. Next, the fine scale effect onto the coarse scale solution must be modeled. It can be shown that the fine scale solution is driven by the residual of the coarse scale solution [9]. This notion motivates the residual-based modeling of the fine scale effects. Since the R-VMS method originates from a weak formulation, it can be utilized in a finite element framework.

The discontinuous Galerkin (DG) method is a finite element method that makes use of discontinuous basis functions [10, 11]. This numerical method has proven particularly suitable for computational fluid dynamics (CFD) applications. Compared to the continuous Galerkin (CG) method, it does not suffer from the typical stability issues [12]. Compared to a finite volume method, the DG framework allows a higher-order discretization of an arbitrary mesh topology. High-order approximation spaces will conserve the advection of important flow structures, such as vorticity, over larger distances and times [13]. A clear downside of the DG framework is the increase in computational cost. On the same mesh, a DG implementation will use considerably more degrees of freedom than a CG equivalent. A promising recent development is the static condensation of many degrees of freedom [14–16]. In a highly parallelizable post-processing step, the DG solution can be retrieved. This leads to superconvergence in the L^2 error norm. The hybridizable DG (HDG) method can compete with CG implementations in terms of accuracy versus computational cost [17, 18]. Overall the DG method has found its way into many state-of-the-art research fluid dynamics codes [19].

Both the R-VMS method and the DG method have shown much potential, particularly for CFD applications. However these frameworks have not yet been combined. The classical R-VMS method leans heavily on the level of continuity of the computational trial space.

Therefore, early adaptations of the method proposed the use of higher order continuous NURBS as basis functions [2, 20]. When the approximation basis is not sufficiently smooth, the R-VMS model dictates the formation of Dirac layers between elements. These are not accurately taken into account by a typical finite element implementation. In turn, this leads to inconsistent integration. In a DG setting the problem is more significant. Second derivatives would result in derivatives of Dirac layers at element interfaces. In the weak formulation these Dirac layers, and their derivatives, act on a discontinuous fine scale field. The fine scale field is undefined at the location of the Dirac layer. Additionally, the classical R-VMS method assumes zero element boundary values for the fine scale solution. This approximation is no longer appropriate for a coarse scale approximation space that permits discontinuities on element interfaces. All these issues will have to be mitigated to make the R-VMS method suitable for a DG framework.

Throughout the development of the DG-RVMS approach it will be shown that the strategy provides a different point of view for developing, evaluating and understanding DG methods. It is argued that the multiscale nature of the solution lies at the core of the coupling of the per-element weak formulations to form a global weak formulation. The obtained global formulation is exact, but still includes fine scale element surface terms. It is shown, and experimentally verified, that classical DG formulations (e.g. upwind techniques, interior penalty methods, etc.) can be interpreted as implicit constraints on the fine scale solution. Thereby the remaining fine scale element surface terms are removed from the formulation. Finally a new residual-based fine scale model is proposed that models the volumetric effect of the fine scales onto the computational solution. All these steps are carefully verified with reference computations, and the final model is tested on a more complex partial differential equation to asses its performance.

The thesis is structured as follows. Chapter 2 is a literature review of the classical R-VMS method. Of particular importance is Section 2.3. This section goes into the importance of the continuity of the approximation basis. There, the core of the problem for use of discontinuous basis functions is discussed in detail. Additionally, this section contains a review of prior work in a variational multiscale setting, that concerns some measure of discontinuity of the trial space.

Once the state-of-the-art is reviewed, Chapter 3 provides the core of this thesis work. The DG-RVMS methodology is proposed. Section 3.1 lays the foundation of the method, which is then applied to a Poisson equation in Section 3.2 and an advection-diffusion reference problem in Section 3.3. In these sections the method is verified step by step, while a number of existing DG formulations are investigated in a new light. Next, the obtained model is tested for the more complex, transient, nonlinear, viscous Burgers equation in Chapter 4.

The DG-RVMS strategy that is introduced in this work opens up many routes for future research. A number of research topics are suggested in Chapter 5. This chapter also includes a summary and concluding remarks.

Chapter 2

Prior work on the residual-based variational multiscale method

Before the residual-based variational multiscale (R-VMS) method is adapted to suit a discontinuous Galerkin (DG) framework, it is important to understand how this method is normally introduced. To this end, the current chapter will provide an historic overview of the development of the method. The goal is to understand its application and its limitations. In particular, the issues that arise when one aims to make use of discontinuous basis functions will be investigated.

To keep this literature review relatively short, this chapter will refrain from going into too much mathematical detail. Instead it aims to provide a conceptual view of the residual-based variational multiscale method. Exact formulations and rigorous mathematical detail will be left to the following chapters.

First, the general principles of the variational multiscale (VMS) paradigm are introduced in Section 2.1. Then, the residual-based modeling of the fine scale effect is discussed in Section 2.2. Finally, the importance of the level of continuity of the solution space is looked at in Section 2.3. Understanding these implications will prove important to extend the method to support the use of discontinuous basis functions.

2.1 The variational multiscale paradigm

Generally a discrete representation of an exact solution will not be able to capture the fine scale behavior of the system. Often this is not a problem; the error that is introduced by neglecting the fine scale solution will be insignificant compared to the range of approximations and uncertainties inherent to engineering practice. However, there are many problems in the field of engineering where the fine scale effects are fundamentally tied to the coarse scale response of the system. Two examples of such problems are:

1. The plastic deformation of a geometrically complex structure. When such a structure is discretized with too coarse a mesh, then the stress concentrations will not be properly represented. Yet, the level of plastic deformation is directly tied to the peak stresses. The result is artificial stiffening of the structure [3, 6].
2. Turbulent fluid flow. The small scale vortical structures that are developed due to wall interaction propagate and grow until they have a dominant effect on the global flow pattern [4]. Additionally, the kinetic energy of the flow is, on average, transported from large flow patterns to smaller flow structures. Eventually it is dissipated in the form of heat in the fine scale range through viscous effects [5].

In both these cases the fine scale nature of the problem has a direct, non-negligible, effect on the coarse scale solution. As such, omitting the fine scale effects will yield inaccurate results. The variational multiscale (VMS) method is a framework for computational mechanics problems which aims to resolve this shortcoming. It offers a strategy for incorporating the effect of subgrid scale behavior of the exact solution onto the computational (coarse scale) solution.

The VMS solution procedure was introduced in 1995 [21]. The initial approach focused on weak formulations that could be obtained from (energy) minimization problem of the form shown in Eq. (2.1). The solution u is the function that minimizes the functional J while in the space $\mathbb{Q}(u_D)$. This function space satisfies the Dirichlet boundary condition $u = u_D$ on (part of) the domain boundary. Such a problem set-up encompasses many solid mechanics problems, where the total strain energy in the continuum body is minimized. The standard functional analysis approach is to equate the functional derivative (or Gâteaux derivative) to zero, as shown in Eq. (2.2). Note that w must be zero on the Dirichlet boundary such that $u + w$ still satisfies the original Dirichlet condition. This yields a weak formulation that includes a trial and a test function. In the standard Bubnov-Galerkin finite element method the test and trial function are confined to the same finite dimensional function space. Thereby a square system of equations can be derived which defines the matrix problem associated to the finite element problem. It is at this stage that the VMS method proposes a different strategy.

$$u = \min_{u \in \mathbb{Q}(u_D)} \int_\Omega J(x, u, \nabla u, \nabla^2 u, \cdots) \tag{2.1}$$

$$\frac{\mathrm{d}}{\mathrm{d}\epsilon} \int_\Omega J(x, u + \epsilon w, \nabla(u + \epsilon w), \nabla^2(u + \epsilon w), \cdots) \Big|_{\epsilon=0} = 0 \qquad \forall\, w \in \mathbb{Q}(0) \tag{2.2}$$

The confinement of the trial and test functions to the finite element spaces is the nature of the discretization, and hence the source of the problem. The variational multiscale method proposes to split the solution into its coarse scale and fine scale components according to Eq. (2.3). Here $\bar{u}$ denotes the solution that can be represented in the solution field obtained from the computational mesh and basis functions. The component u' is the remainder that cannot be represented in this function space. It is thus called the subgrid scale or fine scale solution.

$$u = \bar{u} + u' \tag{2.3}$$

$$u = \bar{u} + u' + \epsilon\,(\bar{w} + w') \tag{2.4}$$

Based on the same principle, the decomposition of Eq. (2.4) is used in the functional derivative of Eq. (2.2). The obtained weak formulation must hold for arbitrary $\bar{w}$ and w' in their respective function spaces. As such, they can be split into two different weak formulations:

$$\begin{cases} B(\bar{w}\,, \bar{u} + u') = L(\bar{w}) & \forall\, \bar{w} \in \bar{\mathbb{Q}}(0) \\ B(w', \bar{u} + u') = L(w') & \forall\, w' \in \mathbb{Q}'(0) \end{cases} \tag{2.5}$$

$B(\,\cdot\,,\,\cdot\,)$ is the bilinear form of the corresponding partial differential equation (PDE), and $L(\cdot)$ is the linear form. The first line in Eq. (2.5) constitutes the weak formulation corresponding to the finite element problem that will be solved. In its current form, this weak formulation captures the true scale interaction that governs the system. The second line is referred to as the fine scale problem, or fine scale weak formulation. In order to close the coarse scale weak formulation, a model of the fine scale solution must be substituted. Formulating a suitable fine scale model is the fundamental challenge of the VMS strategy.

The solution procedure just described was introduced by Hughes in 1995 [21]. In a follow-up paper in 1996, the term variational multiscale was coined [22]. Two years later the principles were more formally introduced in the paper *The variational multiscale method - a paradigm for computational mechanics* [1]. The theory was expanded to include weak formulations that are obtained by the method of weighted residuals. For linear problems, the coarse scale weak formulation may be written in the form of Eq. (2.6). In this equation Ω is the domain of definition. $\mathscr{L}$ is the differential operator and $\mathscr{L}^*$ its adjoint. It is assumed that the coarse scale solution satisfied the Dirichlet boundary conditions strongly. Then all the fine scale boundary terms disappear in the case of second order PDEs. Notice that the fine scale solution is only important in a weighted sense, in a separate term in the formulation.

$$\int_\Omega \bar{w}\,\mathscr{L}\,\bar{u} \;+\; \int_\Omega \mathscr{L}^*\bar{w}\,u' = \int_\Omega \bar{w}\,f \tag{2.6}$$

This method encompasses a broader range of mechanics applications, including advection (first order) problems. However, since these formulations do not recover minimization solutions at their core, the finite element method is less robust. It is argued that the lack of robustness is, in part, due to the lack of incorporation of the fine scale effects. The VMS method becomes a tool for the development of stabilized methods. The art of developing such stabilized methods again lies in the formulation of the fine scale model [8, 21].

Early adaptations of the VMS principle employed a fine scale model that predominantly aimed to capture the physical interpretation of the fine scale behavior of the solution. In the case of turbulence modeling, typical practice was to replace the fine scale solution with an appropriately scaled diffusion term [23–25]. The aim was to mimic the dissipative effect of the fine scales. This concept was loaned from the well known eddy viscosity models that are used often in the large-eddy simulation (LES) and Reynolds-averaged Navier-Stokes (RANS) turbulence modeling techniques. More sophisticated fine scale models are analytically inspired by the fine scale problem in Eq. (2.5). These will be the focus of Section 2.2.

2.2 Residual-based fine scale modeling

Most of the attention dedicated to the VMS method focuses on CFD problems. This is in part due to the strong multiscale nature of fluid flow, and in part due to the importance of stabilizing the finite element formulation for advection based PDEs. It is thus in the framework of turbulence modeling that the *residual-based* fine scale modeling principle was introduced. More specifically, residual-based formulations for subgrid scale models were first proposed in Calo's 2004 PhD dissertation [9]. Bazilevs built on this work in his PhD thesis in 2006, where he focused more on the use of Green's functions to invert the fine scale problem [26]. In 2007, this new modeling approach was published with a strong mathematical foundation [2]. A summary of the ideas proposed in these manuscripts follows below. Then, the ties to stabilized methods are investigated.

2.2.1 The driving effect of the coarse scale residual

The fine scale problem can be written in its weak form according to Eq. (2.5). In this equation, $B(\,\cdot\,,\cdot\,)$ is the bilinear form associated to the PDE. The linear nature of this construct allows manipulation of Eq. (2.5) into the following form.

$$B(w', u') = L(w') - B(w', \bar{u}) \equiv \mathrm{Res}(w', \bar{u}) \tag{2.7}$$

The right hand side of Eq. (2.7) is recognized as the residual of the course scale solution in the dual of the fine scale space, paired with w'. Even for nonlinear PDEs, a similar structure of the fine scale weak formulation can be developed. In Chapter 4, this is shown for the nonlinear Burgers equation. The form of Eq. (2.7) indicates that the fine scale solution is driven, or 'forced', by the coarse scale residual. An analytical expression for u' is sought that fits Eq. (2.7). Inspired by its residual-based forcing, a certain scaling with the coarse scale residual is expected. The following arguments for the expected scaling behavior of u' are proposed in [2, 9, 26].

↪ When the coarse scale residual is zero throughout the complete domain, $\mathscr{R}_{\bar{u}} = 0$, then the exact solution is recovered and $u' = 0$

↪ With finer discretization, the space $\bar{\mathbb{Q}}$ becomes larger. Larger $\bar{\mathbb{Q}}$ should mean that $\bar{u}$ is a better approximation to u which should lead to lower $\mathscr{R}_{\bar{u}}$.

↪ Lower $\mathscr{R}_{\bar{u}}$ should mean smaller u'.

These arguments suggest a perturbation series of the following form,

$$u' = \sum_{k=1}^{\infty} \varepsilon^k u'_k \tag{2.8}$$

where:

$$\varepsilon = \left\| f - \mathscr{L}\bar{u} \right\|_{L^2} \equiv \left\| \mathscr{R}_{\bar{u}} \right\|_{L^2} \tag{2.9}$$

Note that, different from typical perturbation series methods, the ε already occurs in the first term of the series. This ensures that $u' = 0$ when $\mathscr{R}_{\bar{u}} = 0$. For the Navier-Stokes equation, which was the focus of [2,9,26], it can be shown that the fine scale weak form can be dissected into different orders of ε. Each term in the perturbation series of Eq. (2.8) corresponds to a separate order of ε. This dissection simplifies each of the individual fine scale PDEs [2].

Bazilevs *et al.* truncate the perturbation series at the first term, which effectively omits all small scale square terms [2]. Thereby, they obtain the fine scale model shown in Eq. (2.10). In the initial work by Calo, an asymptotic series approximation was proposed that took into account all the perturbation terms [9]. Calo's asymptotic series approximation has the same form as Eq. (2.10). However, in his work he proposes a recursive equation for τ that also depends on $\mathscr{R}_{\bar{u}}$.

$$u' \approx \tau \mathscr{R}_{\bar{u}} \tag{2.10}$$

The model for the fine scale solution can be substituted into the coarse scale formulation of Eq. (2.6) in order to close the system of equations. The fidelity of the coarse scale solution depends on the definition of the scaling parameter τ. Different approaches for developing the scaling parameter have been proposed. The most mathematically rigorous procedure deals with constructing fine scale Green's functions to invert the fine scale problem. Another approach is to enrich the finite element space with special basis functions that have a shape that is inspired by Eq. (2.10) [27]. Thereby, enough approximation freedom is obtained to stabilize the finite element formulation.

2.2.2 The scaling parameter inspired by the fine scale Green's function

The fine scale problem can be dealt with in its strong form, where the solution and forcing are restricted to a confined function space. This strong form can be solved analytically by means of a fine scale Green's function. The classical Green's function $g(x, y)$ is the PDE dependent function for which:

$$u(x) = \int_{\Omega} g(x, y) f(y) \, \mathrm{d}y \tag{2.11}$$

Where Ω is the domain of interest and f is the forcing function. Following the same structure, the fine scale Green's function is defined as:

$$u'(x) = \int_{\Omega} g'(x, y) \mathscr{R}_{\bar{u}}(y) \, \mathrm{d}y \tag{2.12}$$

The details of obtaining Green's functions are left to Appendix A. In this appendix, the Green's functions are derived for the PDEs that will be of importance in Chapters 3 and 4. This appendix also argues that in the case of linear basis functions on a 1D domain, the classical Green's function *is* the fine scale Green's function. Higher order discretizations would require alternative methods for constructing the fine scale Green's function. The relation between the classical Green's function and the fine scale Green's function is given by Eq. (2.13). This equation is derived from a Lagrange multiplier formulation that ensures u' lies in the fine scale space [28]. In this relation, $\mathcal{P}$ is the projector that defines the projection of u into the finite element space.

$$g' = g - g\mathcal{P}^T(\mathcal{P}g\mathcal{P}^T)^{-1}\mathcal{P}g \tag{2.13}$$

In essence, the fine scale problem is a global problem. The boundary conditions are defined on the boundary of the global domain and the residual-based forcing acts throughout the complete domain. Thereby, the integral in 2.12 spans the global domain. Yet, this is not suitable for a closure measure of the finite element formulation. There, a localized fine scale model is sought. This will ensure that the global stiffness matrix remains scarce, and the assembly cheap. The approach is to define a per element Green's function solution. If one aims to do this without meaning to introduce an approximation, it would require the consistent satisfaction of per-element fine scale boundary conditions. However, the fine scale boundary values are unknown. Therefore, these are ignored, which introduces the first approximation. This is indicated in Eq. (2.14), where K denotes the element interior domain.

$$u'(x) \approx \int_K g'(x,y)\mathcal{R}_{\bar{u}}(y)\,\mathrm{d}y \tag{2.14}$$

The second approximation is introduced by the averaging of the integral in Eq. (2.14). This is an expensive integral and the coarse scale residual is not known a priori. A linear scaling with the coarse scale basis is preferred to fit well into the finite element implementation. Therefore, the coarse scale residual is extracted from the integral. Although this is a substantial approximation, it does yield a fine scale model of the form expected from the scaling discussed in Section 2.2.1.

$$u'(x) \approx \frac{1}{|K|}\int_K u'(x)\,\mathrm{d}x \approx \frac{1}{|K|}\int_K\int_K g'(x,y)\,\mathrm{d}y\,\mathrm{d}x\ \mathcal{R}_{\bar{u}}(x) \equiv \tau\mathcal{R}_{\bar{u}}(x) \tag{2.15}$$

Appendix A and Chapter 3 discuss that the above mentioned approximations become identities for certain restricted sets of computational problems. Therefore, and due to its rigorous mathematical foundation, this method is the preferred method for obtaining the τ values in a controlled environment. It will thus be used to verify certain steps in the development of the discontinuous Galerkin residual-based variational multiscale framework in Chapter 3.

2.2.3 Ties to stabilized formulations and residual free bubbles

Much literature has been written about the similarity of known stabilized methods, the use of residual free bubble functions and the residual-based variational multiscale method [8,29,30]. A brief summary of the main findings in this area of research is provided. As this is slightly out of the scope of this report, the review will be kept concise. However, due to the deeply

rooted stabilization interpretation of the R-VMS method, it is felt that these principles should be touched upon for the sake of completeness.

When Hughes introduced the VMS method in 1995, his initial objective was to develop a more rigorous mathematical foundation for stabilized finite element formulations. This initiative followed from his earlier work on stabilized methods. In 1982, he and Brooks proposed the streamline-upwind Petrov-Galerkin (SUPG) stabilization technique [31]. The technique was developed for use in finite element formulations of the Navier-Stokes equation. The approach incorporates the upwind idea of Petrov-Galerkin weighting functions, while balancing the artificial diffusion that plagues such weighting functions. Later work showed that the method can be interpreted as the addition of the term in Eq. (2.16) to the weak formulation [30].

$$\sum_{K\in\mathcal{T}} \int_K \mathscr{L}_{\mathrm{s}} w \; \tau \, \mathscr{R}_{u_h} \tag{2.16}$$

The differential operator $\mathscr{L}_{\mathrm{s}}$ that acts on the test function w carries the upwind weighting. The parameter τ is called the stabilization parameter. Equation (2.16) is a sum over all element domains K in the computational mesh $\mathcal{T}$. The lack of continuity of the finite element basis means that higher order derivatives are ill defined on element interfaces. Hence, the element interfaces are excluded in Eq. (2.16).

Different stabilization methods make use of different differential operators. The original SUPG method applied in the context of an advection-diffusion equation makes use of the operator from Eq. (2.17). Equation (2.18) corresponds to the Galerkin least-squares (GLS) stabilization technique developed in 1989 [32]. Also the least-squares incompressibility constraint (LSIC) and the pressure-stabilized Petrov-Galerkin (PSPG) can be formulated within the same framework. They involve the pressure trial and test function in the Navier-Stokes equations [33, 34].

$$\mathscr{L}_{\mathrm{s}} = a \cdot \nabla \qquad \text{for SUPG} \tag{2.17}$$

$$\mathscr{L}_{\mathrm{s}} = a \cdot \nabla - \nu\Delta \qquad \text{for GLS} \tag{2.18}$$

The formalism of Eq. (2.16) directly indicates the similarity of these stabilization techniques and the R-VMS model that was just introduced. With proper choice of $\mathscr{L}_{\mathrm{s}}$ and τ, the stabilized methods yield an identical expression to substitution of Eq. (2.15) into Eq. (2.6). In particular, the stabilization parameter must equal the element average fine scale Green's function as per Eq. (2.15). The relation between the stabilization parameter τ and the Green's function is investigated in [29]. Disregarding the element interfaces in Eq. (2.16) corresponds to the per-element homogeneous boundary conditions of the fine scale problem. This was described in the previous section. Even though the stabilization techniques were initially introduced with an 'upwinding' and diffusion-balancing interpretation in mind, in retrospect, it can be shown that the formulation actually incorporates the multiscale nature of the solution.

Another stabilization technique that has received considerable attention in the scientific community is the use of so-called 'residual free bubbles'. These are additional basis functions that are used to enrich the finite element space. They are called 'bubble functions' because their complete support lies within one element. In the general sense, the space of potential bubble functions is infinitely dimensional. The initial approach was to restrict the space of bubble functions to a polynomial subset, and derive the enlarged weak formulation. By means

of static condensation, the degrees of freedom associated with the bubble functions can be removed from the final system of equations [35,36]. The final system of equations only solves for the original finite element basis functions.

Later work focused on finding optimal shapes of the bubble functions. It was recognized that the weak formulations can be split into test functions that involve the finite element basis w^{FEM}, and test functions that involve the infinite dimensional bubble function basis w^{BBL}. The optimal shape of the bubble functions is defined by the second line in Eq. (2.19). It can be found by inversion of this equation. Often, this inversion is as difficult as the initial problem itself, so the associated bilinear form has to be simplified.

$$\begin{cases} B(w^{\mathrm{FEM}}, u^{\mathrm{FEM}} + u^{\mathrm{BBL}}) = L(w^{\mathrm{FEM}}) & \forall\, w^{\mathrm{FEM}} \in \mathbb{Q}^{\mathrm{FEM}} \\ B(w^{\mathrm{BBL}}, u^{\mathrm{FEM}} + u^{\mathrm{BBL}}) = L(w^{\mathrm{BBL}}) & \forall\, w^{\mathrm{BBL}} \in \mathbb{Q}^{\mathrm{BBL}} \end{cases} \tag{2.19}$$

Clearly, the split shown in Eq. (2.19) is very similar the one proposed in Eq. (2.5). Generally, the space of fine scales is broader than the space of bubble functions. However, with the assumption that the fine scales are zero on element boundaries, these spaces are identical. The inversion required to find the optimal shape of the bubble functions is equivalent to the Green's function method for defining the fine scale solution, Eq. (2.12). The difference lies in the static condensation proposed for the residual-free bubbles concept, verses the homogenization of the fine scale Green's function in the R-VMS method. The similarities between the VMS method and the method of bubble functions was realized quite early, in 1997, even before the residual-based modeling of the fine scales was formally introduced [29].

The stabilization interpretation of the R-VMS method might be a reason why the method has never been implemented in a discontinuous Galerkin formulation. DG methods are less prone to the stabilization issues observed in continuous Galerkin implementations [10]. Still, as will be seen in Chapter 3, a multiscale perspective of the DG method proves very insightful. Another potential reason for why this has not been looked at before, is the importance of continuity of the coarse scale approximation space. This continuity is completely released in a DG finite element space. The importance of the continuity in the classical R-VMS method is the focus of the following section.

2.3 On continuity of the coarse scale solution basis

The level of continuity of the coarse scale basis is an important point in the R-VMS framework. In its most general form, the VMS framework for linear problems requires the addition of the following term.

$$\int_{\Omega} \mathscr{L}^{*}\bar{w}\, u' \tag{2.20}$$

The order of continuity of the finite element basis functions must match the order of the adjoint differential operator $\mathscr{L}^{*}$. If the smoothness of the finite element basis is insufficient, then Dirac layers will form between elements. This already occurs when the differential operator includes second derivatives that act on a finite element mesh of Lagrangian basis functions. A standard finite element implementation would not accurately capture these Dirac layers, leading to inconsistent integration.

A similar problem occurs in the definition of the fine scale solution:

$$u'(x) = \int_{\Omega} g'(x,y)\mathscr{R}_{\bar{u}}(y)\,\mathrm{d}y \tag{2.21}$$

Note that this equation spans the global domain Ω. In a typical $\mathscr{C}^0$ finite element implementation, the residual includes Dirac layers. From a theoretical point of view, these are not necessarily problematic. Equation (2.21) shows that these Dirac layers in the residual are spread out across the domain, guided by the fine scale Green's function [8]. However, in practical applications this effect is often omitted.

The simplest approach for mitigating both issues is to use a finite element basis that is sufficiently smooth. Hence the use of non-uniform rotational B-splines (NURBS) in the introductory work on the R-VMS method [2]. These are higher order continuous functions that will not develop the Dirac layers between elements.

Within a standard continuous Galerkin implementation, the Dirac layers are generally not taken into account. Effectively, this ties into the assumption of per-element homogeneous fine scale boundary conditions. When the fine scale solution is assumed to vanish on element boundaries, then the Dirac layer from the differential operator in Eq. (2.20) is multiplied by zero. Additionally, the Dirac layers from Eq. (2.21) no longer play a role, since the equation is split up into per-element integrations.

However, the coarse nature of the finite element space would never permit truly zero fine scale element boundary values. Also for a NURBS implementation this would lead to an approximation. For a framework that suffers from the Dirac layer problem (i.e. a typical CG implementation), this approximation is particularly erroneous. The severity of this issue is investigated in [20]. The R-VMS method is used as a turbulence model. Benchmark problems are solved on a mesh of $\mathscr{C}^1$ quadratic NURBS, and a mesh of $\mathscr{C}^0$ quadratic Legendre basis functions. Indeed the NURBS implementation consistently outperforms the CG equivalent.

For a completely discontinuous set of basis functions, this issue becomes significantly more severe. The Dirac layers occur already for first derivatives. The second derivatives of the differential operator lead to derivatives of Dirac distributions. The discontinuity of the coarse scale basis implies a discontinuous fine scale solution. As such, the Dirac layers (and derivatives thereof) in Eq. (2.20) act on a fine scale solution that is undefined at their location. Within a DG setting, the model formulation of Eq. (2.20) is thus unsuited. Additionally, the jumps in the coarse scale solution field are a direct indication that the fine scale solution does not vanish on element boundaries. This assumption is thus particularly unsuitable in a DG setting. All these issues will be mitigated in the framework that is developed in Chapter 3.

Different approaches that involve discontinuous basis functions of some sort have already been proposed. These are touched upon first.

Collis and Ramakrishnan have presented a number of publications on a discontinuous Galerkin VMS turbulence model [37–39]. Their work stems from before the introduction of the R-VMS model in 2007. Instead, they use a so-called three-scale formulation. The solution is split up into a coarse scale, an intermediate scale and a fine scale field. The coarse scale and intermediate scales are computed, while the fine scales are modeled. It is assumed that the fine scales only interact with the intermediate scales. Their effect on the coarse scale solution is neglected. This is based on known scale interaction of Navier-Stokes turbulence. Then,

the effect on the intermediate scale range is modeled by means of a dissipative energy sink. Implementation wise they use an eddy viscosity model, which is known from LES and RANS computations [40]. The same model will be implemented in Section 4.2. Collis and Ramakrishnan reported better results on a per-degree-of-freedom basis compared to classical turbulence models. This was achieved by making use of the superior adaptive meshing capabilities that come with discontinuous basis functions.

A recent publication proposed the use of discontinuous basis functions as bubble functions [41, 42]. This is more in the spirit of residual-based modeling, as argued in Section 2.2.3. The coarse scale function space is composed of NURBS. The fine scale field is assumed to be spanned by the set of per-element continuous functions (the bubble function interpretation). In turn, this function space is compressed to a single low order polynomial function for each element. These may be discontinuous across elements. The original problem dictates zero values of the fine scale solution on element boundaries. This boundary condition is enforced weakly on the discontinuous fine scale basis through an interior penalty approach. Weak satisfaction of the homogeneous fine scale boundary conditions is argued to more accurately capture per-element boundary layer effects of the fine scale problem. Potentially, the discontinuous fine scale degrees of freedom could be statically condensed from the set of equations. This would yield a formulation purely dependent on the coarse scale NURBS. The use of discontinuous subscales is reported to stabilize the coarse scale formulation, even for a $p = 1$ polynomial order for the fine scale field. Optimal rates of convergence are proven and obtained.

The above mentioned method, proposed in 2017, is heavily based on the 'multiscale discontinuous Galerkin' method introduced in 2006 [43]. The discontinuous approximation obtained from a DG formulation is decomposed in a continuous part, and a discontinuous part. The goal is to find the continuous part. Thereby, the added degrees of freedom that plague a DG implementation are discarded, while the robustness of the DG framework is retained. Promising results are obtained, and further analysis is performed in [44, 45].

The previously mentioned methods make use of discontinuous fine scale bubble functions [41, 42], or a decomposition of a DG approximation into a continuous and a discontinuous part [43–45]. These approaches are fundamentally different from the decomposition of the *true solution* into a DG functions space, and an accompanying fine scale function space. That would be DG equivalent of the variational multiscale approach discussed in Section 2.1. Indeed, such a split of basis functions will be the point of origin for the development of the DG-RVMS strategy in Chapter 3.

Chapter 3

Discontinuous Galerkin residual-based variational multiscale modeling

Now that the residual-based variational multiscale method has been introduced from a historical point of view, it will be extended to a discontinuous Galerkin (DG) setting. In the DG framework, this method will be abbreviated as the DG-RVMS method. The importance of the continuity of the solution field was reviewed in Section 2.3. These points will need to be mitigated in order to make the method suitable for a DG framework. Thereby, the DG-RVMS method will be conceptually different on a number of points.

As the core of the proposed methodology will be developed in this chapter, it will be considerably more mathematically oriented. The predominant focus will be on 1D, linear, second order differential equations. The finite element function space will consist of linear basis functions. In this setting, many of the principles of the R-VMS method can be treated analytically. As such, the proposed steps can be verified and understood. The extension to higher order discretizations and multidimensional domains will be discussed briefly. The subsequent chapter will provide a study of the performance of the method in a more complex case.

This chapter will start with a study on a function space level. The split into a coarse scale and fine scale function spaces will be looked at. It will become apparent that this split is not well defined in a DG framework. An additional constraint must be imposed on the fine scale solution in order to make the method well posed. This constraint will act on the element boundaries and is a modeling choice. As such, it is called the fine scale surface model. On top of the fine scale surface model, a fine scale volumetric model is also required. This corresponds to the R-VMS model of the previous chapter. However, in a DG framework the per-element fine scale boundary conditions should not be equated to zero. Therefore, the fine scale volumetric model is reformulated while taking these into account. The first section concludes with a 5-step roadmap that embodies the DG-RVMS strategy.

Section 3.2 will apply the method to a Poisson problem. For such a problem the volumetric term may be omitted, as shown in Sections 3.2.1 and 3.2.4. This section will, therefore, mainly

focus on the fine scale surface model. It is shown that many of the classical DG formulations can be reinterpreted as a VMS formulation with a specific choice of fine scale surface model.

Thereafter, in Section 3.3, the same methodology is used to obtain finite element formulations of an advection-diffusion problem. For this problem the volumetric fine scale term may not be omitted. This would constitutes a modeling error. The proposed fine scale volumetric term is verified. Next, it is shown that upwind type methods may also be interpreted as a fine scale surface model. Additionally, it is shown that upwind numerical fluxes act as an ad hoc solution for the problematic omission of the volumetric fine scale term, in classical formulations.

Through the investigation of these two model problems, the DG-RVMS method will be verified step by step. After this chapter, a strong foundation of the method has been developed. The thorough understanding of its foundation will help extend the method to more complex PDEs.

3.1 The residual-based variational multiscale method in a discontinuous approximation space

The analyses in this chapter will be restricted to second order, linear, partial differential equations. Their well know behavior and relative simplicity makes them perfectly suitable for developing a mathematical foundation. This section will first provide the VMS function space definitions for a function basis that is sufficiently smooth. Subsequently, these space definitions are changed to accept the function basis associated with a discontinuous Galerkin method. The conceptual implications of such a change will be discussed. Finally, in Section 3.1.3, these considerations will take shape as a set of steps that defines the DG-RVMS framework.

The weak formulation of a linear PDE consists of a bilinear form $B(\,\cdot\,,\,\cdot\,)$ and a linear form $L(\,\cdot\,)$, acting on the domain Ω with boundary $\partial\Omega$. A Dirichlet problem is considered, such that $u = u_D$ on $\partial\Omega$. The theory that will be presented extends to Neumann boundary conditions, or mixed boundary conditions, in a straight forward way.

$$B(w,u) = L(w) \tag{3.1}$$

This work will deal with exact solutions that are at least $\mathscr{C}^1$ continuous throughout the domain Ω.

A number of definitions will be repeatedly used throughout this document. They are combined in Table 3.1 for easy reference.

3.1.1 Function space definitions for a $\mathscr{C}^1$ continuous finite element space

The variational multiscale paradigm suggests the split of w and u into a coarse scale component and a fine scale component, i.e., $\bar{u}$ and u'. The coarse scale solution is obtained as some projection of the solution onto the function space spanned by the finite element basis $\bar{\mathbb{Q}}$, such that $\bar{u} = \mathscr{P}_{\bar{\mathbb{Q}}} u$. The fine scale components live in the space that complements the finite

Table 3.1: *Collection of reoccurring definitions.*

Jump operator	$[\![p]\!]$	$= p^+ \cdot n^+ + p^- \cdot n^-$
Average operator	$\{\!\{p\}\!\}$	$= \frac{1}{2}\left(p^+ + p^-\right)$
Space domain	Ω	$\subset \mathbb{R}^d$
Domain boundary	$\partial\Omega$	$\subset \mathbb{R}^{d-1}$
Element domain	K	$\subset \Omega$
Element boundary	∂K	$\subset \mathbb{R}^{d-1}$
Domain tessellation	$\mathcal{T}$	$= \{K_i\}_{i=0}^{N}$, the set of all N elements.
Volume L^2-inner product	$(p,q)_K$	$\int_K q \cdot p$
Surface L^2-inner product	$\langle p \cdot n, q \rangle_{\partial K}$	$\int_{\partial K} q \cdot n\, p$
Numerical interior domain	Ω_E	$= \bigcup_{K\in\mathcal{T}} K$
		$(p,q)_{\Omega_E} = \sum_{K\in\mathcal{T}} (p,q)_K$
Interior facets (Excludes domain boundary)	Γ	$= \left[\bigcup_{K\in\mathcal{T}} \partial K\right] \backslash \partial\Omega$
		$= \{x_1, x_2, \cdots, x_j, \cdots, x_{N-1}\}$ (in 1D)
		$\langle [\![p]\!], 1 \rangle_\Gamma = \sum_{K\in\mathcal{T}} \langle p \cdot n, 1 \rangle_{\partial K \backslash \partial\Omega}$
		$\langle \{\!\{p\}\!\}, 1 \rangle_\Gamma = \sum_{K\in\mathcal{T}} \langle \frac{1}{2} p, 1 \rangle_{\partial K \backslash \partial\Omega}$

element space $\mathbb{Q}'$, and now $u' = u - \bar{u}$. Dirichlet boundary conditions are incorporated in the finite element space, which implies that the test function is zero on the boundary.

$$
\begin{aligned}
&u \in \mathbb{Q}(u_D), \quad w \in \mathbb{Q}(0), \quad \mathbb{Q}(g) = \{q \in \mathscr{C}^0(\Omega) : q = g \text{ on } \partial\Omega\} \\
&\bar{u} \in \bar{\mathbb{Q}}(u_D), \quad \bar{w} \in \bar{\mathbb{Q}}(0), \quad \bar{\mathbb{Q}}(g) = \{q \in \mathscr{C}^1(\Omega) : q\big|_K \in P^p(K)\ \forall K \in \mathcal{T},\ q = g \text{ on } \partial\Omega\} \\
&u' \in \mathbb{Q}', \qquad w' \in \mathbb{Q}', \qquad \mathbb{Q}' = \mathbb{Q}(g) \setminus \bar{\mathbb{Q}}(g) \subset \mathscr{C}^0(\Omega) \quad \Rightarrow \quad \mathbb{Q}(g) = \bar{\mathbb{Q}}(g) \oplus \mathbb{Q}'
\end{aligned}
\tag{3.2}
$$

In these function space definitions K denotes an element domain, $\mathcal{T}$ is the computational mesh, and $P^p(K)$ is the set of polynomial functions up to order p. Note that $\mathbb{Q}'$ is zero on the domain boundary by construction. The coarse scale finite element space is finite dimensional, and the fine scale solution space is infinite dimensional.

For conceptual simplicity, it will be required that the finite element space has the level of continuity that corresponds to the order of the PDE. For second order PDEs, this would mean a $\mathscr{C}^1$ continuous finite element space. This will ensure that the derivatives are well defined throughout the entire domain, and that no Dirac layers develop between elements.

As such, these principles are well suited within the framework of isogeometric analysis, where B-spline basis functions are used [46].

Since the finite element space is continuous, and the true solution is also assumed to be at least $\mathscr{C}^0$ continuous, this must mean that $\mathbb{Q}' \subset \mathscr{C}^0$. Any discontinuity in the fine scale solution added to a continuous coarse scale solution would lead to a discontinuous true solution. This contradicts the required $\mathscr{C}^0$ continuity of the exact solution.

The test function can be split up into its coarse scale and its fine scale components. Due to the linearity of the PDE and the accompanying bilinear form, also the weak formulation may be split into a coarse scale and a fine scale weak formulation. For this to be allowed, it is imperative that $\bar{\mathbb{Q}}(0)$ and $\mathbb{Q}'$ are non-overlapping subspaces, that is, $\bar{\mathbb{Q}}(0) \cap \mathbb{Q}' = \{0\}$. This means that the space of the original test functions $\mathbb{Q}(0)$ is their direct sum. Failure to meet this requirement would mean that the fine scale weak form yields more unknowns than equations. This would form an ill defined (infinite) set of equations.

$$\begin{cases} B(\bar{w}, \bar{u} + u') = L(\bar{w}) \\ B(w', \bar{u} + u') = L(w') \end{cases} \tag{3.3}$$

By virtue of the direct sum decomposition $\mathbb{Q}(g) = \bar{\mathbb{Q}}(g) \oplus \mathbb{Q}'$, any element $u \in \mathbb{Q}(u_D)$ is directly decomposed into its components $\bar{u} \in \bar{\mathbb{Q}}(u_D)$ and its components $u' \in \mathbb{Q}'$. These components are fixed by definition of u and the two function spaces. Only a single projector exists that defines $\bar{u} = \mathscr{P}_{\bar{\mathbb{Q}}} u$. This projector is tied to the decomposition of $\mathbb{Q}$ into its fine and coarse scale bases. The fundamental goal of the (R-)VMS method is to obtain the coarse scale component $\bar{u}$ rather than any other finite element approximation u_h. The coarse scale components, by definition, correctly incorporate the fine scale effects.

3.1.2 Function space definitions for a discontinuous finite element space

Some significant conceptual changes need to be made to this framework to obtain a discontinuous Galerkin formulation. The fundamental difference is that the coarse scale solution basis is discontinuous from element to element. As such, a new coarse scale function space $\bar{\mathscr{V}}$ is defined. Since the true solution is continuous, this must mean that the fine scale solution space is also discontinuous. Therefore, also a new fine scale function space $\mathscr{V}'$ is defined. Finally, a global function space is defined from which these two subspaces are extracted. This space is denoted $\mathscr{V}$. By the discontinuous nature of the coarse and fine scale subspaces, $\mathscr{V}$ must also be discontinuous. The function space definitions that are used to define the VMS method in a DG framework are provided in Eq. (3.4).

$$\begin{aligned} &u \in \mathscr{V}(u_D),\ w \in \mathscr{V}(0),\ \mathscr{V}(g) = \{v \in L^2(\Omega) : v\big|_K \in P^\infty(K)\ \forall K \in \mathscr{T},\ v = g \text{ on } \partial\Omega\} \\ &\bar{u} \in \bar{\mathscr{V}}(u_D),\ \bar{w} \in \bar{\mathscr{V}}(0),\ \bar{\mathscr{V}}(g) = \{v \in L^2(\Omega) : v\big|_K \in P^p(K)\ \forall K \in \mathscr{T},\ v = g \text{ on } \partial\Omega\} \\ &u' \in \mathscr{V}'(\cdot),\ \ w' \in \mathscr{V}'(\cdot),\ \mathscr{V}'(m) = \{v \in L^2(\Omega) : v\big|_K \in I^l(K\,; m)\ \forall K \in \mathscr{T},\ v = 0 \text{ on } \partial\Omega\} \end{aligned} \tag{3.4}$$

There is a lot of hidden information in this collection of function spaces.

First of all, note that the space $\mathscr{V}$ is richer than the space $\mathbb{Q}$ that was defined for the continuous case. Since $\mathscr{V} \supset \mathbb{Q} \subseteq \mathscr{C}^0$, the true solution u is still an element of this space. Since

the weighted-residual formulation will make use of a test function that is also in $\mathbb{Q}$, it will constitute a problem with equal numbers of degrees of freedom and equations. Therefore the widening of the solution space is not a problem.

Secondly, the discontinuous nature of $\mathcal{V}$ requires that the weak formulation is defined on a per element basis. This ensures the existence of derivatives, which would otherwise lead to problematic Dirac layers at element boundaries. Defining per-element weak formulations is common practice for DG methods. These separate weak formulations need to be coupled to obtain a global formulation. The VMS based approach will show that this coupling follows naturally from manipulation of the fine scale field.

The most significant difference in the function spaces of Eqs. (3.2) and (3.4) lies in the definition of the fine scale function space. The fine scale component u' will be discontinuous when the finite element solution $\bar{u}$ is discontinuous. Looking at a single element, this means that both $\bar{u}$ and u' have nonzero values on the boundary. This requires that both the fine scale function space and the coarse scale solution space include the low order basis functions. This requires that $I^l(K;m)$ is defined as the set of polynomials defined on K that complements $P^p(K)$, plus the set of edge basis functions which are equated to m on the element boundary. In 1D, the edge basis functions are the linear polynomials. The prescribed values m are double valued on mesh edges, such that they permit the discontinuity in u'.

An example set of function spaces $\bar{\mathcal{V}}$, $\mathcal{V}(0)'$ and $\mathcal{V}'(u'_0, u'_1)$ is shown in Figure 3.1. Only a single element is considered in this figures. The split can be visualized explicitly by using the hierarchical Legendre basis functions. Technically the fine scale function basis should be infinitely dimensional. In the figure the subspace $\bar{\mathcal{V}}$ consists of a $p = 3$ polynomial basis. These functions are removed from $\mathcal{V}$ to obtain $\mathcal{V}(0)'$, while the basis functions that have support on the element boundary are kept in $\mathcal{V}'(u'_0, u'_1)$.

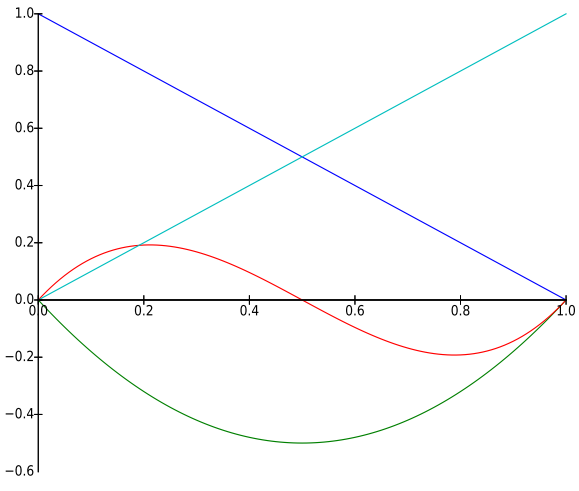

(a) Function space for $\bar{u}, \bar{w} \in \bar{\mathcal{V}}$ in a non-boundary element with polynomial degree $p = 3$.

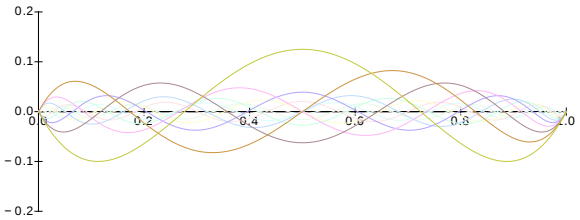

(b) Function space $\mathcal{V}'(0)$.

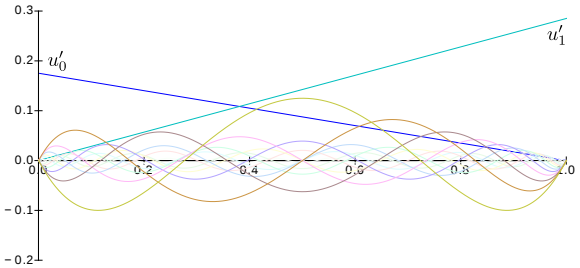

(c) Function space $\mathcal{V}'(u'_0, u'_1)$.

Fig. 3.1: *Example of the function spaces $\bar{\mathcal{V}}$ and $\mathcal{V}'$ for a single 1D element. Visualized with hierarchical Legendre basis functions.*

The requirement that the linear basis functions are in both $\bar{\mathcal{V}}$ and $\mathcal{V}'$ creates a problem. The analogous method in the continuous case required $\bar{\mathbb{Q}} \cap \mathbb{Q}' = \{0\}$. This ensured that the weak formulation in the form of Eq. (3.3) is not over or under constrained. In contrast, the DG spaces from Eq. (3.4) leave an under constrained problem; the low order polynomials in $\bar{u}$ and u' must together equal u on the element boundary, but can take arbitrary values otherwise. Two possible mitigations of this issue are proposed:

1. The direct sum decomposition of the test function space is prioritized. The suggested approach is to remove the low order basis functions from the test function fine scale space. Thereby, $w' \in \mathcal{V}'(0)$. It follows that the global test function space is a direct sum according to $w \in \mathcal{V}(0) = \bar{\mathcal{V}}(0) \oplus \mathcal{V}'(0)$. The catch is that removing basis functions from the test function space requires that the solution is known for the associated basis function in the trial function space. This means that the fine scale components need to be known at element boundaries.

2. Alternatively, one can accept that the function spaces result in a split of the weak formulation that is insufficiently constrained. As such the projection $\bar{u} = \mathcal{P}_{\bar{\mathcal{V}}} u$ no longer maps to a single $\bar{u}$. Instead, a new projection $\bar{u} = \mathcal{P} u$ has to be defined that poses additional constraints on the low order basis functions. Numerical experiments in Sections 3.2 and 3.3 show that for a polynomial basis of $p = 1$ this projector may, for instance, be the L^2 or H^1 projector. The fine scale element boundary values corresponding to the projector are denoted $u'_{\mathcal{P}}$, such that $u' \in \mathcal{V}'(u'_{\mathcal{P}})$

Whichever reasoning the reader is more comfortable with, the conclusion is the same: problem (3.3) is not well defined in a DG environment without a sufficient constraint on the fine scale solution. Different choices of the boundary terms $u'_{\mathcal{P}}$ will lead to different solutions $\bar{u}$. Without a choice of the nodal fine scale values, the projection $\mathcal{P}_{\bar{\mathcal{V}}} u$ is left unspecified and the solution $\bar{u}$ becomes undetermined.

Generally, the values $u'_{\mathcal{P}}$ on element boundaries are not known a priori. However, it turns out that these pointwise values are not explicitly required to solve the finite element (coarse scale) formulation of Eq. (3.3). The global finite element formulation will turn out to involve jumps and averages of the fine scale solution (and its derivatives) across element boundaries. These need to be defined in order to close the formulation. They can be treated either explicitly (by means of predetermined values/equations) or implicitly (by relating them to $\bar{u}$). The solution $\bar{u}$, and thereby implicitly the projector $\mathcal{P}$, depend on the choice of these fine scale surface terms. The choice of these terms constitutes a constraint on the fine scale solution, which makes the global problem well defined. Therefore, these choices will be referred to as a 'fine scale surface model'. It can be shown that existing DG formulations make use of implicit fine scale surface models. Obtaining and evaluating these fine scale surface models for a range of DG formulations will be one of the primary objectives of Sections 3.2 and 3.3.

By means of a fine scale surface model, the fine scale solution is sufficiently constrained. However, the element boundary value of u' also has an effect on the volumetric fine scale model. The Green's function approach discussed in Section 2.2.2 can be extended to incorporate the fine scale boundary terms. The obtained equation reads:

$$u'(x) = \int_K g'(x,y)\, \mathcal{R}_{\bar{u}}(y)\, \mathrm{d}y + \int_{\partial K} h'(x,y) u'(y)\, \mathrm{d}y \tag{3.5}$$

The definitions of $g'(x,y)$ and $h'(x,y)$ are linked, and depend on the PDE at hand. Refer to Appendix A for the details and a number of examples. $u'(y)$ is the fine scale boundary value. Again, this will either need to be treated explicitly, or implicitly. The implicit treatment strategy would strongly relate to the fine scale surface model that is employed. In a 1D setting, the approximation strategy discussed in Section 2.2.2 results in the following residual-based fine scale model. Again, this is elaborated on in Appendix A.

$$u'(x) \approx \tau(x)\mathscr{R}_{\bar{u}}(x) + \gamma_0(x)u'(x_j) - \gamma_1(x)u'(x_{j+1}) \qquad \text{For } x \in [\, x_j \,,\, x_{j+1} \,] \tag{3.6}$$

Next, all these different facets of the R-VMS method in a DG setting are collected into a single set of steps.

3.1.3 The proposed DG-RVMS procedure

The considerations that were discussed in the previous section are combined and crystallized into the following roadmap. This set of steps constituted the proposed DG-RVMS procedure. The procedure is general enough to be applicable for a wide range of PDEs.

1. Obtain the per element weak formulation via a weighted residual approach.

   Find $u \in \mathscr{V}(u_D)$ s.t.:
   $$\int_K w\,\mathscr{L}u \;=\; \int_K w\,f \qquad \forall\, w \in \mathscr{V}(0) \tag{3.7}$$

   Where $\mathscr{L}$ is the differential operator, and u_D the Dirichlet boundary condition. In the following, these integrals will be written by making use of the L^2-inner product notation defined in Table 3.1.

2. Introduce the proposed decomposition into the coarse scale and fine scale solution spaces. The fine scale weak formulation in Eq. (3.8) is rewritten to show the residual-based forcing.

   Find $\bar{u}, u' \in \bar{\mathscr{V}}(u_D) \times \mathscr{V}'(u'_{\mathscr{P}})$ s.t.:
   $$\begin{cases} \left(\bar{w}\,,\mathscr{L}\bar{u}\right)_K \;+\; \left(\bar{w}\,,\mathscr{L}u'\right)_K \;=\; \left(\bar{w}\,,f\right)_K & \forall\, \bar{w} \in \bar{\mathscr{V}}(0) \\ \left(w',\mathscr{L}u'\right)_K \;=\; \left(w',f-\mathscr{L}\bar{u}\right)_K \;\equiv\; \left(w',\mathscr{R}_{\bar{u}}\right)_K & \forall\, w' \in \mathscr{V}'(0) \end{cases} \tag{3.8}$$

3. Apply integration by parts on the terms in the coarse scale equation.

   $$B(\bar{w},\bar{u};K) + s(\bar{w},\bar{u};\partial K) + \left(\mathscr{L}^*\bar{w}\,,u'\right)_K + k(\bar{w},u';\partial K) = L(\bar{w};K) \quad \forall\, \bar{w} \in \bar{\mathscr{V}}(0) \tag{3.9}$$

   $B(\,\cdot\,,\,\cdot\,;K)$ is the bilinear form that is typically found in finite element formulations for the PDE at hand, although constrained to element K. Similarly, $L(\,\cdot\,;K)$ is the linear form on element K. The functionals $s(\,\cdot\,,\,\cdot\,;\partial K)$ and $k(\,\cdot\,,\,\cdot\,;\partial K)$ are the per-element surface terms that are obtained from integration by parts. The differential operator $\mathscr{L}^*$ is the adjoint operator of $\mathscr{L}$.

4. The per-element formulations are combined into a global formulation. To this end, the fine scale boundary values are written as:

$$\begin{aligned} u'^{\pm}\, n^{\pm} &= \frac{1}{2}(u'^{+} + u'^{-})\, n^{\pm} + \frac{1}{2}(u'^{+} n^{+} + u'^{-} n^{-}) \equiv \{\!\{u'\}\!\}\, n^{\pm} + \frac{1}{2}[\![u']\!] \\ \nabla u'^{\pm} \cdot n^{\pm} &= \frac{1}{2}(\nabla u'^{+} + \nabla u'^{-}) \cdot n^{\pm} + \frac{1}{2}(\nabla u'^{+} \cdot n^{+} + \nabla u'^{-} \cdot n^{-}) \equiv \{\!\{\nabla u'\}\!\} \cdot n^{\pm} + \frac{1}{2}[\![\nabla u']\!] \\ &\dots \end{aligned} \tag{3.10}$$

These are identities. The values indicated with a + or a − sign correspond to either side of the interface. The notation on the rightmost side makes use of the average and jump operators ($\{\!\{\cdot\}\!\}$ and $[\![\cdot]\!]$) defined in Table 3.1. Use of these fine scale boundary expressions will yield a global formulation. However, this formulation includes many fine scale element surface terms. Many of these can be eliminated from the formulation by using the following identities.

$$\begin{aligned} [\![u]\!] &= 0 = [\![\bar{u} + u']\!] = [\![\bar{u}]\!] + [\![u']\!] \quad \Rightarrow \quad [\![u']\!] = -[\![\bar{u}]\!] \\ [\![\nabla u]\!] &= 0 = [\![\nabla \bar{u} + \nabla u']\!] = [\![\nabla \bar{u}]\!] + [\![\nabla u']\!] \quad \Rightarrow \quad [\![\nabla u']\!] = -[\![\nabla \bar{u}]\!] \\ &\dots \end{aligned} \tag{3.11}$$

For these identities to hold, the true solution requires a certain smoothness. The PDEs considered in this document require $\mathscr{C}^1$ continuity. Substitution of Eq. (3.11) into Eq. (3.10) yields:

$$\begin{aligned} u'^{\pm}\, n^{\pm} &\equiv \{\!\{u'\}\!\}\, n^{\pm} - \frac{1}{2}[\![\bar{u}]\!] \\ \nabla u'^{\pm} \cdot n^{\pm} &\equiv \{\!\{\nabla u'\}\!\} \cdot n^{\pm} - \frac{1}{2}[\![\nabla \bar{u}]\!] \\ &\dots \end{aligned} \tag{3.12}$$

These are the expressions that are used in the term $k(\bar{w}, u'\,; \partial K)$. The per-element weak formulations are summed. Thereby, intra-element coupling of the weak formulation is realized. The following global coarse scale weak formulation is obtained.

$$\begin{aligned} B(\bar{w}, \bar{u}; \Omega_E) + \sum_{K \in \mathscr{T}} s(\bar{w}, \bar{u}; \partial K) + \left(\mathscr{L}^{*}\bar{w}\,, u'\right)_{\Omega_E} \\ + \sum_{K \in \mathscr{T}} k(\bar{w}, u'; \partial K) = L(\bar{w}; \Omega_E) \qquad \forall\, \bar{w} \in \bar{\mathscr{V}}(0) \end{aligned} \tag{3.13}$$

Note the use of the domain Ω_E, introduced in Table 3.1. This domain excludes the element interfaces. As such, no Dirac layers will form.

5. The obtained global weak formulation is not well defined. The fine scale surface model needs to be introduced. This was discussed in Section 3.1.2. Specifically, the average fine scale terms that occur due to substitution of Eq. (3.12) need to be prescribed. This may be done through the use of an explicit (Eq. (3.14)) or an implicit (Eq. (3.15)) fine scale surface model.

$$\begin{aligned} \{\!\{u'\}\!\} &= \Phi^{\mathrm{E}}(x) \\ \{\!\{\nabla u'\}\!\} &= \Theta^{\mathrm{E}}(x) \\ &\dots \end{aligned} \tag{3.14}$$

$$\begin{aligned} \{\!\{u'\}\!\} &= \Phi^{\mathrm{I}}(\{\!\{\bar{u}\}\!\}, [\![\bar{u}]\!], \{\!\{\nabla\bar{u}\}\!\}, [\![\nabla\bar{u}]\!], \cdots) \\ \{\!\{\nabla u'\}\!\} &= \Theta^{\mathrm{I}}(\{\!\{\bar{u}\}\!\}, [\![\bar{u}]\!], \{\!\{\nabla\bar{u}\}\!\}, [\![\nabla\bar{u}]\!], \cdots) \\ &\cdots \end{aligned} \tag{3.15}$$

6. Finally, the volumetric fine scale model is included. The model of Eq. (3.6) requires the fine scale boundary values. They are obtained by combining the fine scale model Eq. (3.14) or Eq. (3.15) with Eq. (3.11):

$$u'^{\pm} = \{\!\{u'\}\!\} - \frac{1}{2}[\![\bar{u}]\!] \cdot n^{\pm} = \Phi^{\mathrm{I/E}}(\cdots) - \frac{1}{2}[\![\bar{u}]\!] \cdot n^{\pm} \tag{3.16}$$

Thereby, the 1D volumetric fine scale model becomes:

$$u'(x) \approx \tau(x)\mathcal{R}_{\bar{u}}(x) + \gamma_0(x)\left(\Phi^{\mathrm{I/E}} + \frac{1}{2}[\![\bar{u}]\!]\right)\Big|_{x_j} - \gamma_1(x)\left(\Phi^{\mathrm{I/E}} - \frac{1}{2}[\![\bar{u}]\!]\right)\Big|_{x_{j+1}} \tag{3.17}$$

For each point x in the element from x_j to x_{j+1}. This is substituted in place of the remaining fine scale contribution in Eq. (3.13). Thereby, a closed global coarse scale formulation is obtained. This formulation incorporates the fine scale effects onto the computational coarse scale solution.

This framework will be employed for the analysis of two example problems. These are the second order elliptic Poisson equation, and an advection-diffusion problem. Within a constrained setting, the fine scale surface model will be satisfied pointwise, and the fine scale volumetric model of Eq. (3.17) becomes an identity. As such, each step of procedure can be verified.

3.2 The Poisson equation

The DG-RVMS framework that has just been described will first be utilized for a second order elliptic operator: the Poisson equation. The problem is defined as follows, where Ω is the d-dimensional spatial domain with boundary $\partial\Omega$. The second line is the Dirichlet boundary condition.

$$\begin{cases} -\Delta u = f & \text{in } \Omega \subset \mathbb{R}^d \\ u = u_D & \text{on } \partial\Omega \end{cases} \tag{3.18}$$

The Laplace operator is omnipresent in engineering applications. It signifies diffusion in transport problems, and balance of momentum in continuum mechanics problems. It is thus imperative for any numerical method to be able to accurately deal with this type of differential operator. However, in the case of DG methods it posed a major challenge for many years. It took until the late '90s until there were a number of breakthroughs. These lead to a surge of new method formulations and much research in this area [10, 11, 47]. While the derivations proposed in those works are not the basis for the current work, it is important to know the classical derivation of these DG formulations in order to understand the differences with

the proposed DG-RVMS strategy. As such, a comprehensive summary of the derivation is provided in Appendix B.

3.2.1 A global coarse scale weak formulation

The weak formulation is defined on a per-element basis. This is the first step in the outline of Section 3.1.3. It ensures the existence of derivatives within the domain of integration. The following weak formulation is obtained by multiplication of Eq. (3.18) with the test function w and subsequent integration over the element domain.

$$\begin{aligned} &\text{Find } u \in \mathscr{V}(u_D) \text{ s.t.:} \\ &\quad (w, -\Delta u)_K = (w, f)_K \qquad \forall\, w \in \mathscr{V}(0) \end{aligned} \tag{3.19}$$

The test and trial functions are split into their coarse scale and fine scale components: $\bar{u} \in \bar{\mathscr{V}}(u_D)$, $\bar{w} \in \bar{\mathscr{V}}(0)$, $u' \in \mathscr{V}'(u'_{\mathscr{P}})$ and $w' \in \mathscr{V}'(0)$. For now $u'_{\mathscr{P}}$ is left unspecified. Such a split yields two new weak formulations. Due to linearity of the Laplace operator, these can be written if the following form.

$$\begin{aligned} &\text{Find } \bar{u} \in \bar{\mathscr{V}}(u_D),\ u' \in \mathscr{V}'(u'_{\mathscr{P}}) \text{ s.t.:} \\ &\begin{cases} (\bar{w}, -\Delta\bar{u})_K + (\bar{w}, -\Delta u')_K = (\bar{w}, f)_K & \forall\, \bar{w} \in \bar{\mathscr{V}}(0) \\ (w', -\Delta u')_K = (w', f + \Delta\bar{u})_K \equiv (w', \mathscr{R}_{\bar{u}})_K & \forall\, w' \in \mathscr{V}'(0) \end{cases} \end{aligned} \tag{3.20}$$

In these weak forms the differential operator $\mathscr{L}$ would be is defined as

$$\mathscr{L} = -\Delta \tag{3.21}$$

In order to introduce the fine scale model later on, the fine scale solution is separated from the differential operator by using the following general form of Green's identity.

$$(p, \mathscr{L}q)_K = (\mathscr{L}^* p, q)_K + k(p, q; \partial K) \tag{3.22}$$

Where $\mathscr{L}^*$ is the adjoint operator of $\mathscr{L}$. The functional $k(p, q; \partial K)$ constitutes the accompanying boundary terms obtained from integration by parts. For a Poisson problem they are defined as:

$$\mathscr{L}^* = \mathscr{L} = -\Delta \tag{3.23}$$

$$k(p, q; \partial K) = -\langle p, \nabla q \cdot n \rangle_{\partial K} + \langle \nabla p \cdot n, q \rangle_{\partial K} \tag{3.24}$$

Eq. (3.22) is substituted into Eq. (3.20). Additionally, a single integration by parts is performed on the first term. The following per-element coarse scale equation is obtained. This corresponds to step 3 in the strategy of Section 3.1.3.

$$(\nabla\bar{w}, \nabla\bar{u})_K - \langle \bar{w}, \nabla\bar{u} \cdot n \rangle_{\partial K} - (\Delta\bar{w}, u')_K + k(\bar{w}, u'; \partial K) = (\bar{w}, f)_k \quad \forall\, \bar{w} \in \bar{\mathscr{V}}(0) \tag{3.25}$$

Subsequently, this per-element weak formulation is summed over all elements in the mesh. The numerical domain Ω_E is defined in Table 3.1. This domain is different from the complete domain Ω in that it excludes element boundaries. As such, no Dirac layers will occur. These

inter-element Dirac layers are implicitly taken into account by the per-element surface terms.

$$\begin{aligned}(\nabla\bar{w},\nabla\bar{u})_{\Omega_E} - \sum_{K\in\mathcal{T}}\langle\bar{w},\nabla\bar{u}\cdot n\rangle_{\partial K} \\ - (\Delta\bar{w},u')_{\Omega_E} + \sum_{K\in\mathcal{T}} k(\bar{w},u';\partial K) = (\bar{w},f)_{\Omega_E} \quad \forall\,\bar{w}\in\bar{\mathcal{V}}(0)\end{aligned} \tag{3.26}$$

Note that at this stage, all boundary conditions and boundary values ($\bar{u}$, $\nabla\bar{u}$, u', $\nabla u'$) are the element interior values. The PDE is 'contained' in the element. Yet intra-element coupling is required to solve the global system. As proposed in the DG-RVMS road map, this element coupling will be enforced through manipulation of the fine scale boundary terms. The fine scale boundary identities of Eq. (3.12) are substituted into the functional $k(\cdot\,,\cdot;\cdot)$. The identities in Eq. (3.12) assume that the exact solution u is at least $\mathcal{C}^1$ continuous across boundaries. For a Poisson equation with $f\in L^2(\Omega)$, this is true.

$$k(\bar{w},u';\partial K) = -\langle\bar{w}\,n,\{\!\{\nabla u'\}\!\}\rangle_{\partial K} + \langle\frac{1}{2}\bar{w},[\![\nabla\bar{u}]\!]\rangle_{\partial K} + \langle\nabla\bar{w}\cdot n,\{\!\{u'\}\!\}\rangle_{\partial K} - \langle\frac{1}{2}\nabla\bar{w},\,[\![\bar{u}]\!]\rangle_{\partial K} \tag{3.27}$$

Recall that $\{\!\{\cdot\}\!\}$ and $[\![\,\cdot\,]\!]$ are the average and jump operators defined in Table 3.1. Note that all fine scale contributions that appear in the terms in Eq. (3.27) are single valued on element interfaces. Therefore, these terms can be summed across all elements to yield:

$$\sum_{K\in\mathcal{T}} k(\bar{w},u';\partial K) = -\langle[\![\bar{w}]\!],\{\!\{\nabla u'\}\!\}\rangle_\Gamma + \langle\{\!\{\bar{w}\}\!\},[\![\nabla\bar{u}]\!]\rangle_\Gamma + \langle[\![\nabla\bar{w}]\!],\,\{\!\{u'\}\!\}\rangle_\Gamma - \langle\{\!\{\nabla\bar{w}\}\!\},[\![\bar{u}]\!]\rangle_\Gamma \tag{3.28}$$

Where Γ is the sum of all interior edges, also defined in Table 3.1. The opposing $\bar{w}\,n$ and $\nabla\bar{w}\cdot n$ terms in Eq. (3.27) are collected as jumps, and the $\frac{1}{2}\bar{w}$ and $\frac{1}{2}\nabla\bar{w}$ terms as averages.

Substitution of Eq. (3.28) into Eq. (3.26) results in the following global formulation.

$$\begin{aligned}(\nabla\bar{w},\nabla\bar{u})_{\Omega_E} - \sum_{K\in\mathcal{T}}\langle\bar{w},\nabla\bar{u}\cdot n\rangle_{\partial K} + \langle\{\!\{\bar{w}\}\!\},[\![\nabla\bar{u}]\!]\rangle_\Gamma - \langle\{\!\{\nabla\bar{w}\}\!\},[\![\bar{u}]\!]\rangle_\Gamma \\ - (\Delta\bar{w},u')_{\Omega_E} - \langle[\![\bar{w}]\!],\{\!\{\nabla u'\}\!\}\rangle_\Gamma + \langle[\![\nabla\bar{w}]\!],\,\{\!\{u'\}\!\}\rangle_\Gamma \quad \forall\,\bar{w}\in\bar{\mathcal{V}}(0)\end{aligned} \tag{3.29}$$

The sum in this formulation may be combined with the third term in the formulation according to:

$$\begin{aligned}&(\{\!\{p\}\!\},[\![q]\!])_{\partial K} - (p,q\cdot n)_{\partial K^+} - (p,q\cdot n)_{\partial K^-} \\ &\quad= \int_K \Big(\frac{1}{2}(p^+ + p^-)(q^+n^+ + q^-n^-) - (p\,q\,n)^+ - (p\,q\,n)^-\Big) \\ &\qquad= \int_K \Big(\frac{1}{2}(p^+q^+n^+ + p^+q^-n^- + p^-q^+n^+ + p^-q^-n^-) - p^+q^+n^+ - p^-q^-n^-\Big) \\ &\qquad\qquad= \int_K \frac{1}{2}\Big(-p^+n^+q^+ - p^+n^+q^- - p^-n^-q^+ - p^-n^-q^-\Big) \\ &\qquad\qquad\qquad= -\int_K \frac{1}{2}(p^+n^+ + p^-n^-)(q^- + q^+) = -([\![p]\!],\{\!\{q\}\!\})_{\partial K}\end{aligned} \tag{3.30}$$

This yields the exact global coarse scale weak formulation:

$$\begin{aligned}\left(\nabla\bar{w},\nabla\bar{u}\right)_{\Omega_E} - \left\langle[\![\bar{w}]\!],\{\!\{\nabla\bar{u}\}\!\}\right\rangle_\Gamma - \left\langle\{\!\{\nabla\bar{w}\}\!\},[\![\bar{u}]\!]\right\rangle_\Gamma \\ - \left(\Delta\bar{w},u'\right)_{\Omega_E} - \left\langle[\![\bar{w}]\!],\{\!\{\nabla u'\}\!\}\right\rangle_\Gamma + \left\langle[\![\nabla\bar{w}]\!],\{\!\{u'\}\!\}\right\rangle_\Gamma \quad \forall\,\bar{w}\in\bar{\mathcal{V}}(0)\end{aligned} \tag{3.31}$$

It is important to realize that the current derivation made no assumptions, approximations or choices of numerical fluxes. The weak formulation in Eq. (3.31) is identically satisfied by the exact solution. Interestingly, this weak formulation is very similar to many of the classical formulations that have been used for decades. The first three terms in the obtained equation (3.31) are exactly those proposed by Bassi and Rebay in 1997 [48]. These are the terms that are used in almost every DG approximation of the diffusion operator. However, the classical formulations are typically derived in a very different manner. Refer to Table 3.2 for a comprehensive overview of DG formulations, and to Appendix B for a summary of their derivation.

Table 3.2: *Overview of discontinuous Galerkin formulations for a Poisson problem. Adapted from [11].*

Method name	**Global weak formulation**
Bassi-Rebay [48]	$\left(\nabla\bar{w},\nabla\bar{u}\right)_{\Omega_E} - \left\langle[\![\bar{w}]\!],\{\!\{\nabla\bar{u}\}\!\}\right\rangle_\Gamma - \left\langle\{\!\{\nabla\bar{w}\}\!\},[\![\bar{u}]\!]\right\rangle_\Gamma + \left(r([\![\bar{w}]\!]),r([\![\bar{u}]\!])\right)_{\Omega_E}$
Brezzi *et al.* [49]	$\left(\nabla\bar{w},\nabla\bar{u}\right)_{\Omega_E} - \left\langle[\![\bar{w}]\!],\{\!\{\nabla\bar{u}\}\!\}\right\rangle_\Gamma - \left\langle\{\!\{\nabla\bar{w}\}\!\},[\![\bar{u}]\!]\right\rangle_\Gamma + \left(r([\![\bar{w}]\!]),r([\![\bar{u}]\!])\right)_{\Omega_E} - \left\langle[\![\bar{w}]\!],\mu\,\{\!\{r_e(\bar{u})\}\!\}\right\rangle_\Gamma$
Local DG [50]	$\left(\nabla\bar{w},\nabla\bar{u}\right)_{\Omega_E} - \left\langle[\![\bar{w}]\!],\{\!\{\nabla\bar{u}\}\!\}\right\rangle_\Gamma - \left\langle\{\!\{\nabla\bar{w}\}\!\},[\![\bar{u}]\!]\right\rangle_\Gamma + \left\langle[\![\bar{w}]\!],\eta\,[\![\bar{u}]\!]\right\rangle_\Gamma + \left\langle\beta\cdot[\![\bar{w}]\!],[\![\nabla\bar{u}]\!]\right\rangle_\Gamma + \left\langle[\![\nabla\bar{w}]\!],\beta\cdot[\![\bar{u}]\!]\right\rangle_\Gamma + \left(r([\![\bar{w}]\!])+l([\![\beta\cdot\bar{w}]\!]),r([\![\bar{u}]\!])+l([\![\beta\cdot\bar{u}]\!])\right)_{\Omega_E}$
Interior penalty [51]	$\left(\nabla\bar{w},\nabla\bar{u}\right)_{\Omega_E} - \left\langle[\![\bar{w}]\!],\{\!\{\nabla\bar{u}\}\!\}\right\rangle_\Gamma - \left\langle\{\!\{\nabla\bar{w}\}\!\},[\![\bar{u}]\!]\right\rangle_\Gamma + \left\langle[\![\bar{w}]\!],\eta\,[\![\bar{u}]\!]\right\rangle_\Gamma$
Bassi *et. al* [52]	$\left(\nabla\bar{w},\nabla\bar{u}\right)_{\Omega_E} - \left\langle[\![\bar{w}]\!],\{\!\{\nabla\bar{u}\}\!\}\right\rangle_\Gamma - \left\langle\{\!\{\nabla\bar{w}\}\!\},[\![\bar{u}]\!]\right\rangle_\Gamma - \left\langle[\![\bar{w}]\!],\mu\,\{\!\{r_e(\bar{u})\}\!\}\right\rangle_\Gamma$
Baumann-Oden [53]	$\left(\nabla\bar{w},\nabla\bar{u}\right)_{\Omega_E} + \left\langle[\![\bar{w}]\!],\{\!\{\nabla\bar{u}\}\!\}\right\rangle_\Gamma - \left\langle\{\!\{\nabla\bar{w}\}\!\},[\![\bar{u}]\!]\right\rangle_\Gamma$
NIPG [54]	$\left(\nabla\bar{w},\nabla\bar{u}\right)_{\Omega_E} + \left\langle[\![\bar{w}]\!],\{\!\{\nabla\bar{u}\}\!\}\right\rangle_\Gamma - \left\langle\{\!\{\nabla\bar{w}\}\!\},[\![\bar{u}]\!]\right\rangle_\Gamma + \left\langle[\![\bar{w}]\!],\eta\,[\![\bar{u}]\!]\right\rangle_\Gamma$
Babuška-Zlámal [55]	$\left(\nabla\bar{w},\nabla\bar{u}\right)_{\Omega_E} + \left\langle[\![\bar{w}]\!],\eta\,[\![\bar{u}]\!]\right\rangle_\Gamma$
Brezzi *et al.* [56]	$\left(\nabla\bar{w},\nabla\bar{u}\right)_{\Omega_E} - \left\langle[\![\bar{w}]\!],\mu\,\{\!\{r_e(\bar{u})\}\!\}\right\rangle_\Gamma$

Some of the entries in Table 3.2 make use of so-called 'lifting operators'. These are volumetric terms that involve element boundary information. They are defined according to Eq. (3.32). Their occurrence mostly originates from the fact that these weak forms are derived from a

mixed formulation of the Poisson equation. Again, refer to Appendix B for the details.

$$-\mu \left\{\!\!\left\{ r_e([\![u_h]\!]) \right\}\!\!\right\} \quad \text{where } r_e([\![u_h]\!]) \text{ satisfies} \quad \int_\Omega r_e([\![u_h]\!]) \cdot \tau = \int_{\partial\Omega} [\![u_h]\!] \cdot \{\!\{\tau\}\!\} \quad \forall\, \tau \in \mathcal{V}_h \tag{3.32}$$

It has been argued in Section 3.1 that the DG-RVMS approach should lead to a $\bar{u}$ that is exactly equal to $\mathcal{P}u$. Therein, $\mathcal{P}$ is some projector of choice such that $\mathcal{P}u \in \bar{\mathcal{V}}(u_D)$ and $u' = u - \mathcal{P}u \in \mathcal{V}'(u'_{\mathcal{P}})$. This projector will affect two parts of the equation. For a polynomial degree larger than 1, the fine scale Green's function must be obtained from the standard Green's function with the use of this projector. However, for a polynomial degree equal to 1, the standard Green's function *is* the fine scale Green's function (refer to Appendix A). In this case, the projector will be implicitly (yet inextricably) tied to the boundary values of u' and $\nabla u'$.

The fine scale boundary terms in Eq. (3.31) appear to be a problem. They hinder the direct computation of $\bar{u}$. In the remainder of this section, it will be shown that the fine scale boundary terms are actually free to be chosen. Their choice defines (or is defined by) the projector $\mathcal{P}$. Section 3.2.2 will show that any desired solution $\bar{u}$ can be obtained by explicit treatment of these terms, i.e., through direct substitution of their values. The exact H^1 projection and L^2 projection of a 1D solution will be retrieved. This serves as validation of the derivation and the theory. Subsequently, Section 3.2.3 will show that many of the classical formulations from Table 3.2 can be recollected through implicit treatment of the fine scale boundary terms, i.e., through substituting a relationship between the fine scale and coarse scale terms. This implicit treatment will constitute a fine scale surface model which sufficiently constrains the fine scale solution. Thereby, the coarse scale weak formulation becomes closed, and its solution well defined.

3.2.2 Verification by means of numerical experiments

Three numerical experiments are presented. The aim is to validate the fine scale terms that were obtained in weak formulation (3.31). For simplicity a 1D domain is discretized with linear basis functions for all the numerical experiments. Refer to Figure 3.2 for the domain and mesh definitions. Since $\mathscr{L}^*\bar{w} = 0$ for first order polynomials, this means that the volumetric fine scale term drops out of the weak formulation. The effect of this term will be investigated in the section on the advection-diffusion equation. The current numerical experiments focus on the effect of the $\{\!\{u'\}\!\}$ and $\{\!\{\nabla u'\}\!\}$ terms. To this end, explicit fine scale surface models will be used, i.e., Eq. (3.14) of step 5 in the DG-RVMS strategy.

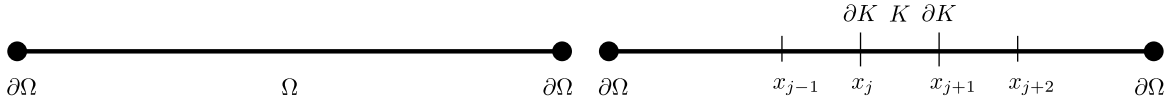

(a) 1D domain definition **(b)** Discretization of the 1D domain

Fig. 3.2: *Definition of 1D domain and discretization.*

When $\bar{u}$ is constructed using an H^1 projection it is nodally coincident with u. As such, $u'_{\mathcal{P}} = 0$, which sufficiently constrains the fine scale solution. Thereby, the coarse scale

problem is well defined. To obtained a closed coarse scale formulation, this condition needs to be incorporated into the terms $\{\!\{u'\}\!\}$ and $\{\!\{\nabla u'\}\!\}$. Clearly one can directly conclude that $\{\!\{u'\}\!\} = 0$ on element interfaces. By using the nodal exactness property an explicit formulation for $\{\!\{\nabla u'\}\!\}$ can be obtained according to:

$$\begin{aligned}\{\!\{\nabla u'\}\!\}\Big|_{\hat{x}} &\equiv \nabla u(\hat{x}) - \{\!\{\nabla \bar{u}\}\!\}\Big|_{\hat{x}} = \frac{\mathrm{d}}{\mathrm{d}x}u(x)\Big|_{\hat{x}} - \frac{1}{2}\left(\frac{u(\hat{x}) - u(\hat{x}-h)}{h} + \frac{u(\hat{x}+h) - u(\hat{x})}{h}\right) \\ &= \frac{\mathrm{d}}{\mathrm{d}x}u(x)\Big|_{\hat{x}} - \frac{u(\hat{x}+h) - u(\hat{x}-h)}{2h} \end{aligned} \tag{3.33}$$

Where $\hat{x}$ is a coordinate on the element boundary, and h is the element width, which is assumed equal on both neighboring elements.

A constant force f yields a parabolic exact solution. For an arbitrary parabola $u = ax^2 + bx + c$ it follows that the last term in Eq. (3.33) is exactly equal to the derivative of the true solution $\frac{\mathrm{d}}{\mathrm{d}x}u = 2ax + b$:

$$\begin{aligned}\frac{u(x+h) - u(x-h)}{2h} &= \frac{ax^2 + 2axh + ah^2 + bx + bh - ax^2 + 2axh - ah^2 - bx + bh}{2h} \\ &= 2ax + b = \frac{\mathrm{d}}{\mathrm{d}x}u(x)\end{aligned}$$

Substitution thereof into Eq. (3.33) shows that for a constant force and linear basis functions $\{\!\{\nabla u'\}\!\} = 0$. An inverse argument says that that when all fine scale terms are omitted from weak formulation (3.31), then the H^1 projection of u must be obtained in case of a constant f and linear basis functions. This is verified in Figure 3.3.

Model problem
$f = 2$
$x_0 = 0,\ x_1 = 5$
$u_0 = 1,\ u_1 = 3$

Exact solution
$u(x) = x^2 + \frac{26}{5}x + 1$

Fine scale model
For $\hat{x} \in \Gamma$:
$\{\!\{u'\}\!\}\Big|_{\hat{x}} = \Phi^{\mathrm{E}}(\hat{x}) = 0$
$\{\!\{\nabla u'\}\!\}\Big|_{\hat{x}} = \Theta^{\mathrm{E}}(\hat{x}) = 0$

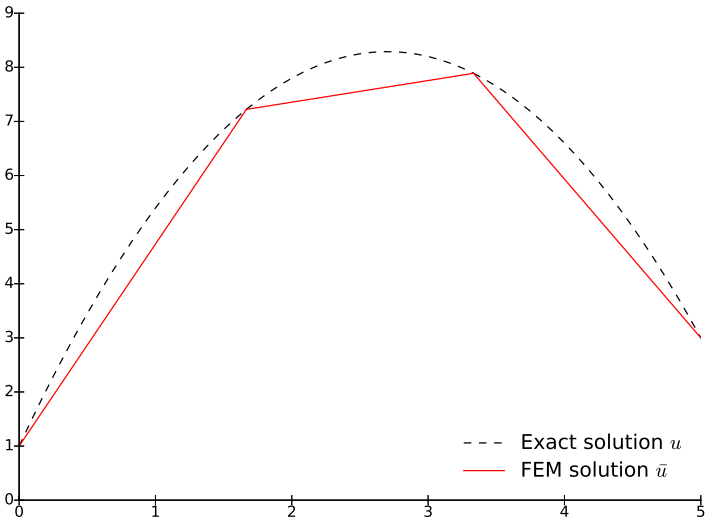

Fig. 3.3: *Nodally exact $\bar{u}$ when all fine scale terms are omitted. Using linear basis functions and constant f.*

For an arbitrary f the nodally exact H^1 projection of u does not necessarily imply $\{\!\{\nabla u'\}\!\} = 0$. In this case nodal coincidence can still be achieved by using the explicit formulation for $\{\!\{\nabla u'\}\!\}$ from Eq. (3.33). The explicit description means that the term in the weak formulation becomes a contribution to the force vector. For a parabolic force $f = 10(x - x^2)$ the nodal exactness is shown in Figure 3.4. Additionally, this figure shows the result when the fine scale terms are omitted. This yields a solution that is far from nodally exact and exhibits significant jumps across elements. Clearly adding the fine scale term $\{\!\{\nabla u'\}\!\}$ has the intended effect.

Model problem

$f = 10(x - x^2)$

$x_0 = 0,\ x_1 = 1$

$u_0 = 0,\ u_1 = 0.1$

Exact solution

$u(x) = -\frac{5}{3}x^3 + \frac{10}{12}x^4 + \frac{14}{15}x$

Fine scale model

For $\hat{x} \in \Gamma$:

$\Phi^{\mathrm{E}}(\hat{x}) = 0$

$\Theta^{\mathrm{E}}(\hat{x}) = \nabla u(\hat{x}) - \{\!\{\nabla \bar{u}\}\!\}\Big|_{\hat{x}}$

$= \frac{\mathrm{d}}{\mathrm{d}x}u(x)\Big|_{\hat{x}} - \frac{u(\hat{x}+h)-u(\hat{x}-h)}{2h}$

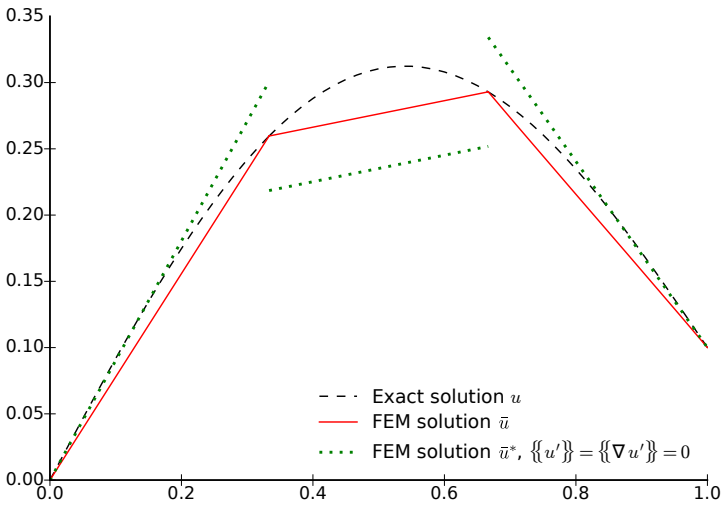

Fig. 3.4: *Nodally exact $\bar{u}$ when an explicit formulation for $\{\!\{\nabla u'\}\!\}$ is implemented.*

Nodal exactness is not necessarily a favorable quality for a discontinuous approximations space. The additional degrees of freedom carry no value. Often one is more interested in a solution that minimizes some error norm. For a given discretization the minimal L^2 error is obtained from the L^2 projection of u onto the finite element space; $\bar{u} = \mathscr{P}_{L^2}u$. Figure 3.5 shows that using explicit formulations for $\{\!\{u'\}\!\}$ and $\{\!\{\nabla u'\}\!\}$ that correspond to the desired $\bar{u}$ indeed yields the L^2 projection of u. In practice a finite element problem was solved to obtain $u_h = \mathscr{P}_{L^2}u$. This solution is used for the explicit formulation of the fine scale boundary terms, which again become force contributions. Note that for its current purpose this L^2 projection must satisfy the boundary conditions such that $u' = u - \bar{u} \in \mathscr{V}'(u'_{\mathscr{P}_{L^2}})$, which is zero on the domain boundary. Figure 3.5 also includes a solution in case all fine scale terms are omitted. Clearly this does not yield an acceptable solution.

All three previous numerical experiments require prior knowledge of the exact solution for their explicit formulation of the fine scale boundary terms. Still it is shown that these additional terms can be manipulated to yield the anticipated finite element solutions. In practice the exact solution is of course seldom available. In these cases the fine scale terms need to be modeled. Different modeling strategies for these terms will be looked at in the next section.

Model problem

$f = 10(x - x^2)$

$x_0 = 0,\ x_1 = 1.5$

$u_0 = 0,\ u_1 = 0.1$

Exact solution

$u(x) = -\frac{5}{3}x^3 + \frac{10}{12}x^4 + \frac{241}{240}x$

Fine scale model

For $\hat{x} \in \Gamma$:

$$\Phi^{\mathrm{E}}(\hat{x}) = u(\hat{x}) - \left\{\!\!\left\{\mathcal{P}_{L^2} u\right\}\!\!\right\}\Big|_{\hat{x}}$$

$$\Theta^{\mathrm{E}}(\hat{x}) = \nabla u(\hat{x}) - \left\{\!\!\left\{\nabla \mathcal{P}_{L^2} u\right\}\!\!\right\}\Big|_{\hat{x}}$$

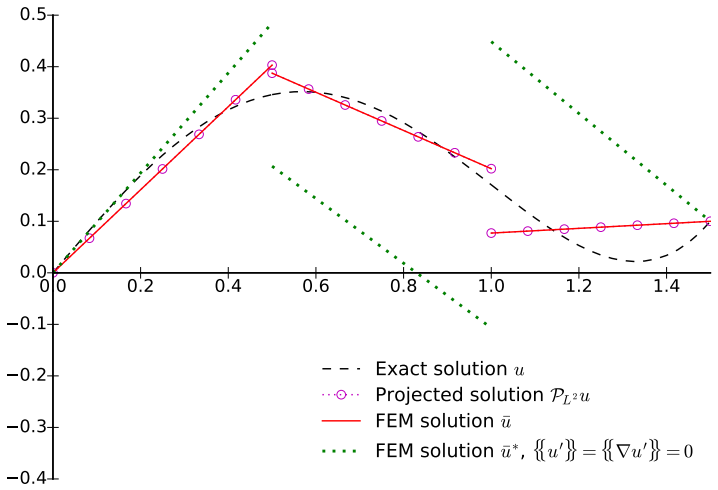

Fig. 3.5: *The L^2 projection of u is obtained with the explicit description for the fine scale terms.*

3.2.3 Recollection of classical discontinuous Galerkin formulations

Different modeling efforts for the three remaining fine scale terms in weak formulation (3.31) lead to different solutions for $\bar{u}$. In extreme cases common projections of the exact solution can be recollected, as shown in the previous section. The appropriate choice of fine scale surface and volume models might be problem dependent. This section will not aim to develop new models as this would be a study in itself. Instead the fine scale surface models that lead to existing formulations are investigated. This should provide insights into the nature of the discretization errors of these methods, the source of approximations of the methods (if any), and the range of applications for which these approximations are valid.

Recall the exact weak formulation:

$$\begin{aligned}(\nabla\bar{w}, \nabla\bar{u})_{\Omega_E} - \langle[\![\bar{w}]\!], \{\!\{\nabla\bar{u}\}\!\}\rangle_\Gamma - \langle\{\!\{\nabla\bar{w}\}\!\}, [\![\bar{u}]\!]\rangle_\Gamma \\ - (\Delta\bar{w}, u')_{\Omega_E} - \langle[\![\bar{w}]\!], \{\!\{\nabla u'\}\!\}\rangle_\Gamma + \langle[\![\nabla\bar{w}]\!], \{\!\{u'\}\!\}\rangle_\Gamma \quad \forall\, \bar{w} \in \bar{\mathcal{V}}(0)\end{aligned} \tag{3.34}$$

This section will again focus on the 1D case. Linear basis functions are used for the construction of the coarse scale solution space. In this setting the fine scale volumetric term is identically zero, and the weak element boundary terms become pointwise strong conditions. This makes it possible to identify the exact modeling choices used to obtain the classical DG formulations. The effect of extending this to a multidimensional setting with higher order basis functions is touched upon in the last two sections.

The interior penalty method

An interior penalty (IP) formulation of the Poisson equation reads:

$$\begin{aligned}(\nabla\bar{w},\nabla\bar{u})_{\Omega_E} - \langle[\![\bar{w}]\!],\{\!\{\nabla\bar{u}\}\!\}\rangle_\Gamma - \langle\{\!\{\nabla\bar{w}\}\!\},[\![\bar{u}]\!]\rangle_\Gamma + \\ \langle\eta h^{-1}[\![\bar{w}]\!],[\![\bar{u}]\!]\rangle_\Gamma = (\bar{w},f)_{\Omega_E} \qquad \forall\,\bar{w}\in\bar{\mathcal{V}}(0)\end{aligned} \tag{3.35}$$

In a 1D case, and when linear basis functions are used, this formulation corresponds to the following implicit fine scale surface model. Equation (3.35) is obtained by substitution of this fine scale surface model into the exact weak form of Eq. (3.34).

$$\begin{cases} \{\!\{u'\}\!\}\Big|_{\hat{x}} = \Phi^{\mathrm{I}}(\hat{x}) = 0 & \hat{x}\in\Gamma \\ \{\!\{\nabla u'\}\!\}\Big|_{\hat{x}} = \Theta^{\mathrm{I}}(\hat{x},[\![\bar{u}]\!]) = -\eta h^{-1}[\![\bar{u}]\!]\Big|_{\hat{x}} & \hat{x}\in\Gamma \end{cases} \tag{3.36}$$

Appendix C shows that pointwise satisfaction of the fine scale model does indeed follow from the comparison of Eqs. (3.34) and (3.35).

The first line is saying that the average of the fine scale solution is zero across element interfaces. As such, $\{\!\{\bar{u}\}\!\} = u$ on element interfaces. Intuitively this is a sound modeling approach. It ensures that the coarse scale solution does not drift away from the exact solution. However, even though $\bar{u}$ centers around the exact solution on element boundaries, there might still be considerable oscillations or jumps from element to element. These jumps are suppressed by the second line in Eq. (3.36). Reformulation of this equation is required to understand its effect. Define $d = \frac{1}{2}h\eta^{-1}$, then for $\hat{x}\in\Gamma$:

$$\begin{aligned} 2d\,\{\!\{\nabla u'\}\!\}\Big|_{\hat{x}} &= -[\![\bar{u}]\!]\Big|_{\hat{x}} = [\![u']\!]\Big|_{\hat{x}} \\ d\nabla u'^{+}(\hat{x}) + d\nabla u'^{-}(\hat{x}) &= n^{+}u'^{+}(\hat{x}) + n^{-}u'^{-}(\hat{x}) \\ n^{-}u'^{+}(\hat{x}) + d\nabla u'^{+}(\hat{x}) &= n^{-}u'^{-}(\hat{x}) - d\nabla u'^{-}(\hat{x}) \\ u'^{+}(\hat{x}) - d\,n^{+}\nabla u'^{+}(\hat{x}) &= u'^{-}(\hat{x}) - d\,n^{-}\nabla u'^{-}(\hat{x}) \\ u'^{+}(\hat{x}-dn^{+}) &\approx u'^{-}(\hat{x}-dn^{-}) \end{aligned} \tag{3.37}$$

In the last line the fine scale surface model is recognized to constitute a first order Taylor approximation. d is the associated distance.

According to this analysis the second line in Eq. (3.36) is saying that the fine scale solutions must be equal at some distance away from the interface. In combination with the first line in Eq. (3.36) this is effectively confining or 'clamping' the fine scale solution close to the interface. As such, it is suppressing the element-to-element oscillations of the coarse scale solution.

Since u' is only continuous within an element, the distance d used in the Taylor approximation only makes sense when it is smaller than the element width. The distance is controlled by the scaling parameter η. This parameter should be larger than 0.5 to ensure $d \leq h$. Good Taylor approximations can only be expected for values significantly higher than 0.5. As η

is increased, the distance d approaches zero and the fine scale solution is forced to zero at element interfaces. This means a nodally exact $\bar{u}$ solution is retrieved. This behavior is in line with the penalization interpretation from which the 'interior penalty' method gained its name.

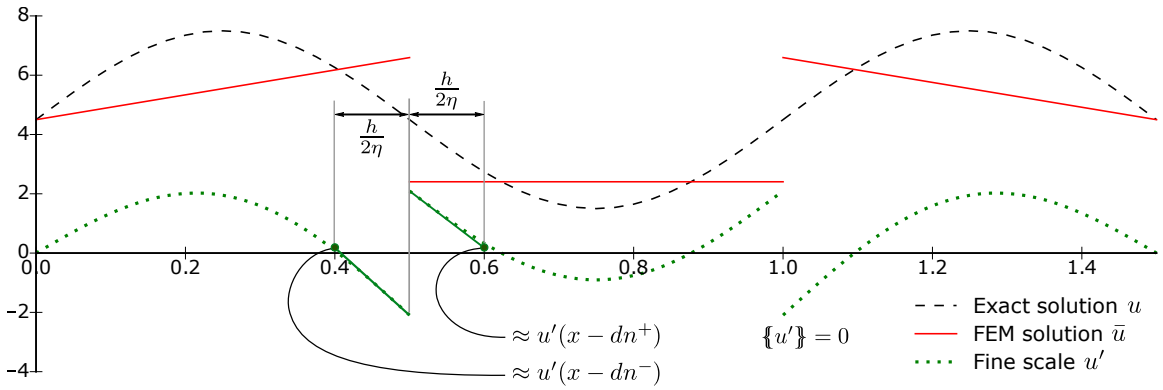

Fig. 3.6: *Interior penalty method computation with $\eta = 2.5$. Showing the implicit fine scale surface model.*

For a sinusoidal force this formulation results in the solution shown in Figure 3.6. The figure shows the previously described fine scale model: the average of u' across the element interface is zero, and the Taylor approximation of u' at a distance d from the interface is equal on both sides.

The nonsymmetric interior penalty Galerkin method

Similar to the previous approach the nonsymmetric interior penalty Galerkin (NIPG) method is obtained when the following two fine scale modeling conditions are employed.

$$\begin{cases} \{\!\{u'\}\!\}\Big|_{\hat{x}} = 0 & \hat{x} \in \Gamma \\ \{\!\{\nabla u'\}\!\}\Big|_{\hat{x}} = -2\{\!\{\nabla \bar{u}\}\!\}\Big|_{\hat{x}} - \eta h^{-1} [\![\bar{u}]\!]\Big|_{\hat{x}} & \hat{x} \in \Gamma \end{cases} \tag{3.38}$$

Substitution of this implicit fine scale surface model into Eq. (3.34) yields the NIPG weak formulation:

$$\begin{aligned} (\nabla \bar{w}, \nabla \bar{u})_{\Omega_E} + \langle [\![\bar{w}]\!], \{\!\{\nabla \bar{u}\}\!\} \rangle_\Gamma - \langle \{\!\{\nabla \bar{w}\}\!\}, [\![\bar{u}]\!] \rangle_\Gamma + \\ \langle \eta h^{-1} [\![\bar{w}]\!], [\![\bar{u}]\!] \rangle_\Gamma = (\bar{w}, f)_{\Omega_E} \qquad \forall\, \bar{w} \in \bar{\mathcal{V}}(0) \end{aligned} \tag{3.39}$$

Just like the IP method the average of u' is equated to zero at element interfaces. Again some further manipulation is required to understand the effect of the second line of the model. By

defining $d = -\frac{h}{2\eta}$, and for $\hat{x} \in \Gamma$:

$$
\begin{aligned}
2d \left\{\!\left\{\nabla u'\right\}\!\right\}\Big|_{\hat{x}} &= -4d \left\{\!\left\{\nabla \bar{u}\right\}\!\right\}\Big|_{\hat{x}} - \left[\!\left[u'\right]\!\right]\Big|_{\hat{x}} \\
d\,\nabla u'^{+}(\hat{x}) + d\,\nabla u'^{-}(\hat{x}) + 2d\,\nabla \bar{u}^{+}(\hat{x}) + 2d\,\nabla \bar{u}^{-}(\hat{x})) &= -n^{+}u'^{+}(\hat{x}) - n^{-}u'^{-}(\hat{x}) \\
-d\nabla u'^{+}(\hat{x}) - d\nabla u'^{-}(\hat{x}) + 4d\,\nabla u(\hat{x}) &= -n^{+}u'^{+}(\hat{x}) - n^{-}u'^{-}(\hat{x}) \\
n^{+}u'^{+}(\hat{x}) - d\nabla u'^{+}(\hat{x}) + 2d\,\nabla u(\hat{x}) &= n^{+}u'^{-}(\hat{x}) + d\nabla u'^{-}(\hat{x}) - 2d\,\nabla u(\hat{x}) \\
u'^{+}(\hat{x}) - d\,n^{+}\nabla u'^{+}(\hat{x}) - 2\,u(\hat{x}) + 2d\,n^{+}\nabla u(\hat{x}) &= u'^{-}(\hat{x}) - d\,n^{-}\nabla u'^{-}(\hat{x}) - 2\,u(\hat{x}) + 2d\,n^{-}\nabla u(\hat{x}) \\
u'^{+}(\hat{x} - dn^{+}) &= u'^{-}(\hat{x} - dn^{-}) + 2\left(u(\hat{x} - dn^{+}) - u(\hat{x} - dn^{-})\right)
\end{aligned}
\tag{3.40}
$$

The last line makes use of a first order Taylor approximation of the fine scale solution and the true solution.

For the IP method the fine scale solution was forced to be equal at a distance d away from either side of the element interface. This constraint might not be favorable when u has high gradients. A certain jump in the fine scale solution could lead to better $\bar{u}$ approximations. The NIPG method relaxes the equality constraint by forcing a jump of twice the offset of the exact solution at the same distance from the interface.

In order to obtain the NIPG formulation the distance d was defined as a *negative* value. As such, the second line of the NIPG model (3.38) is a condition on the *extrapolated* fine scale solution, past its respective element of continuity. This is shown in Figure 3.7.

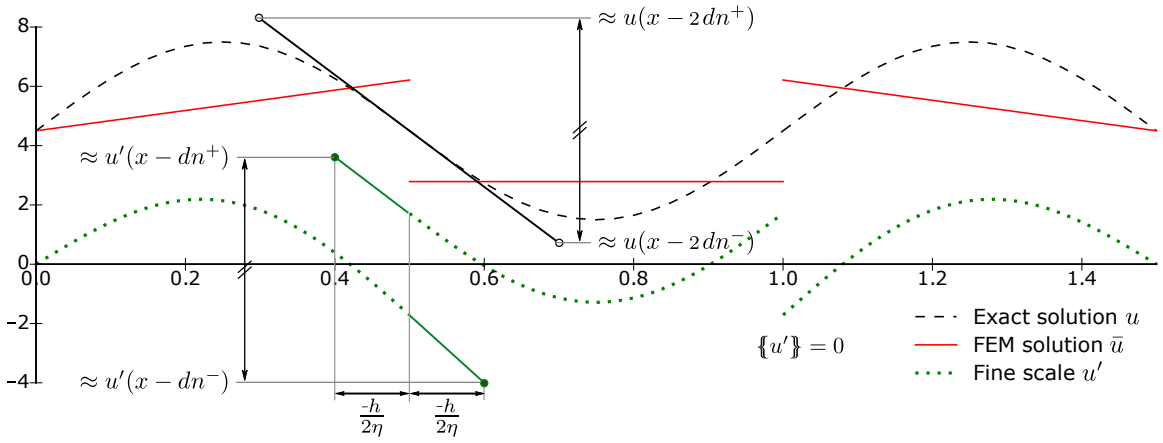

Fig. 3.7: *NIPG method computation with $\eta = 2.5$. Showing the implicit fine scale surface model.*

The finite element solution $\bar{u}$ in Figure 3.7 is obtained under the same conditions as the computation for the IP method (Figure 3.6). The coarse scale solution is very similar despite the significantly different fine scale surface model. The figure depicts the extrapolated fine scale solution. It is shown that the difference thereof on both sides of the element boundary is twice the difference of the exact solution at the same location.

The Baumann-Oden method

The Baumann-Oden method can be retrieved from the following implicit fine scale surface model.

$$\begin{cases} \{\!\{u'\}\!\}\Big|_{\hat{x}} = 0 & \hat{x} \in \Gamma \\ \{\!\{\nabla u'\}\!\} = -2\{\!\{\nabla \bar{u}\}\!\} & \hat{x} \in \Gamma \end{cases} \tag{3.41}$$

Substitution thereof in the exact weak formulation results in the Baumann-Oden formulation:

$$(\nabla \bar{w}, \nabla \bar{u})_{\Omega_E} + \langle [\![\bar{w}]\!], \{\!\{\nabla \bar{u}\}\!\} \rangle_\Gamma - \langle \{\!\{\nabla \bar{w}\}\!\}, [\![\bar{u}]\!] \rangle_\Gamma = (\bar{w}, f)_{\Omega_E} \qquad \forall\, \bar{w} \in \bar{\mathcal{V}}(0) \tag{3.42}$$

The physical interpretation of the second line of the fine scale surface model is less clear than the equivalent conditions discussed for the IP and NIPG methods. The Baumann-Oden method is known to be unstable for a 1D case with a polynomial order of 1 [53]. In such a computational environment the fine scale volumetric term is identically zero and the conditions in Eq. (3.41) are satisfied in a strong sense (see Appendix C). By using the identity $\nabla u(x) = \{\!\{\nabla \bar{u}\}\!\} + \{\!\{\nabla u'\}\!\}$ the second line in Eq. (3.41) can be rewritten as $\{\!\{\nabla \bar{u}\}\!\} = -\nabla u$. This has the notable implication that the *exact solution cannot be obtained* when $\nabla u \neq 0$ on element interfaces. Not even when $\bar{u}$ lies in the space of u. This is shown in Figure 3.8. In this figure the above weak formulation is used to solve a Laplace problem (i.e. $f = 0$) with Dirichlet boundary conditions. The exact solution is a straight line, which can be perfectly represented by the first order polynomial basis of $\bar{u}$. Still the finite element solution $\bar{u}$ does not equal the exact solution. Instead the fine scale surface model is enforced. For this particular case this means that the gradient of $\bar{u}$ will always be incorrect. No convergence in the H^1-seminorm can be expected.

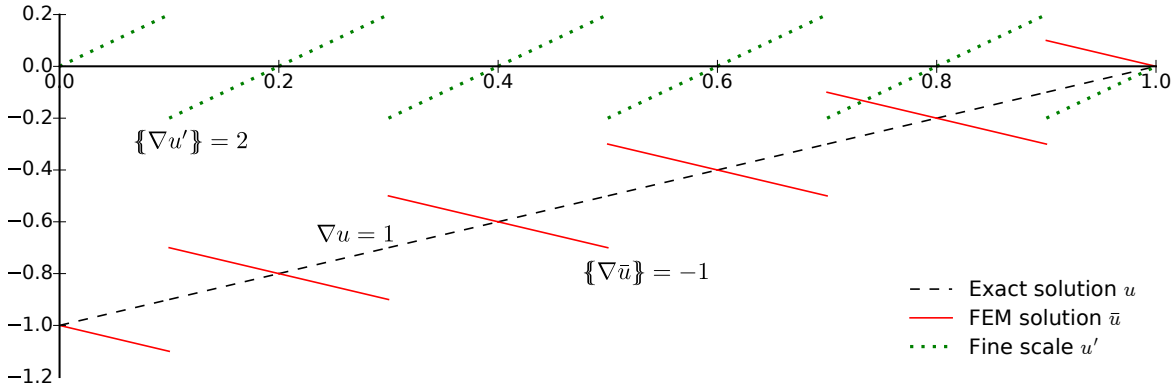

Fig. 3.8: *Baumann-Oden method for a 1D Laplace problem. Showing the implicit fine scale surface model.*

The fact that the exact solution is not retrieved even though it lies in the coarse scale solution space seems to be a fundamental flaw. Still it is not advocated that the Baumann-Oden method should be disregarded in its entirety. In a multidimensional setting, and for higher order polynomials, the Baumann-Oden method is proven to be stable [53]. The next two sections touch upon the implications of computations in such a setting. Additionally, it could

be valuable to consider if there are certain physical systems for which the fine scale surface model of Eq. (3.41) would be especially applicable. For instance when the diffusion operator is only part of the PDE, then the fine scale surface models of the different operators collect into new fine scale surface models. When a Baumann-Oden treatment of the diffusion operator is implemented for such a 'mixed' PDE, additional components would be added to the second line of fine scale model (3.41). This could potentially lead to much more justifiable models. The effect of combining fine scale surface models will be touched upon in the section on the advection-diffusion equation.

3.2.4 Extension to a higher order discretization

The previous computations all employed linear basis functions. In this setting the volumetric fine scale component disappears, as it involves second derivatives of the test function. This term becomes relevant when a higher order discretization is used. The numerical experiments from Section 3.2.2 aimed to find the $\bar{u}$ that is exactly some projection of the exact solution. Recollecting these projections while using higher order basis functions would require incorporation of an appropriate volumetric fine scale model. However, none of the classical formulations (i.e., interior penalty, Baumann-Oden, etc) include a term of the form $(\Delta\bar{w}, \cdot)_{\Omega_E}$. This section shows the effect of the omission of this term.

In Appendix C it is shown that the omission of such a term means that it must equal zero. As such, each of the classical formulations implicitly includes the following fine scale volumetric model:

$$\left(\Delta\bar{w}, u'\right)_{\Omega_E} = 0 \tag{3.43}$$

For a quadratic basis of $\bar{w}$ this means that the per-element average of u' is zero. For third order polynomials the integral of u' weighted by a linear function equals zero, and so further for polynomial orders past three:

$$\begin{aligned}
&p = 2: && \int_K c_1\, u' = 0 && \forall\, K \in \mathcal{T},\ \forall\, c_1 \in \mathbb{R} \\
&p = 3: && \int_K (c_1 + c_2 x)\, u' = 0 && \forall\, K \in \mathcal{T},\ \forall\, c_1, c_2 \in \mathbb{R}\times\mathbb{R} \\
&p = 4: && \int_K (c_1 + c_2 x + c_3 x^2)\, u' = 0 && \forall\, K \in \mathcal{T},\ \forall\, c_1, c_2, c_3 \in \mathbb{R}\times\mathbb{R}\times\mathbb{R} \\
&\cdots && \cdots && \cdots \\
&\text{Generally:} \\
&p > 1: && \int_K u' \sum_{n=1}^{p-1} c_n x^{n-1} = 0 && \forall\, K \in \mathcal{T},\ \forall\, c_1, \cdots, c_{p-1} \in \mathbb{R}^{p-1}
\end{aligned} \tag{3.44}$$

This behavior exhibits a stabilizing effect. The more the fine scale solution is confined to zero, the better the coarse scale solution approximates the exact solution. The importance of this behavior becomes particularly clear when the Baumann-Oden method is considered. This method is known to be unstable for first order discritization on a 1D domain, and

can be proven to be stable when higher order basis functions are used [53]. The numerical experiment in the previous section visualized the curious behavior of the Baumann-Oden method for linear basis functions. Figure 3.9 shows results from the same model problem but for higher order discretizations. The solution quality increases considerably with polynomial order. The identities in Eq. (3.44) have been numerically verified for the resulting solutions in Figure 3.9. Note that the fine scale surface model described in the previous section is still adhered to.

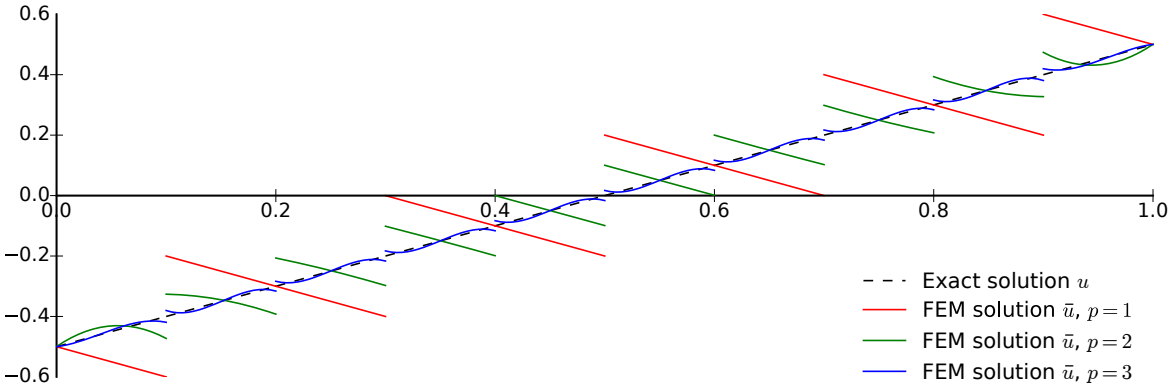

Fig. 3.9: *Baumann-Oden method for a 1D Laplace problem. Showing a multitude of higher order discretizations, each with 10 elements.*

3.2.5 Extension to a multidimensional domain

A final study of the Poisson equation will touch upon the extension of the DG-RVMS framework to a higher dimensional domain. The conclusions drawn for the 1-dimensional case were all based on pointwise identities. The fine scale surface model for a multitude of classical formulations could be obtained by equating terms from the exact DG-RVMS formulation to corresponding terms in the classical finite element formulation. The terms that involve the same operator on the test function can be collected and individually equated to zero. This is shown in Appendix C. However, the same proof does not hold in a multidimensional setting. Not even in an integral sense. Rather than equating each individual term to zero, all the terms must collectively equal zero.

The numerical experiments considered in this section will make use of weak enforcement of the Dirichlet boundary condition. One implication of this method is that the test functions do not vanish on the boundary. The derivation proposed at the beginning of this section would lead to a slightly different weak form. Domain boundary terms would be included in Eq. (3.31), leading to:

$$
\begin{aligned}
&\text{Find } \bar{u} \in \bar{\mathcal{V}} \text{ s.t.:} \\
&\quad (\nabla \bar{w}, \nabla \bar{u})_{\Omega_E} - \langle \bar{w}, \nabla \bar{u} \cdot n \rangle_{\partial\Omega} - \langle [\![\bar{w}]\!], \{\!\{ \nabla \bar{u} \}\!\} \rangle_{\Gamma} - \langle \{\!\{ \nabla \bar{w} \}\!\}, [\![\bar{u}]\!] \rangle_{\Gamma} + \\
&\qquad (\mathscr{L}^* \bar{w}, u')_{\Omega_E} - \langle \bar{w}, \nabla u' \cdot n \rangle_{\partial\Omega} - \langle [\![\bar{w}]\!], \{\!\{ \nabla u' \}\!\} \rangle_{\Gamma} \\
&\qquad\quad + \langle \nabla \bar{w} \cdot n, u' \rangle_{\partial\Omega} + \langle [\![\nabla \bar{w}]\!], \{\!\{ u' \}\!\} \rangle_{\Gamma} = (\bar{w}, f)_{\Omega_E} \qquad \forall\, \bar{w} \in \bar{\mathcal{V}}
\end{aligned}
\tag{3.45}
$$

Within this new framework an interior penalty formulation is obtained by the weak satisfaction of the following fine scale surface model on the boundary.

$$-\nabla u' \cdot n = \eta h^{-1} u' \tag{3.46}$$

This model is substituted into Eq. (3.45). Subsequently, the identity $u' = u_D - \bar{u}$ is used on the domain boundary to remove any remaining fine scale terms. Thereby, the classical interior penalty formulation Eq. (3.47) is retrieved.

$$\begin{aligned}(\nabla\bar{w}, \nabla\bar{u})_{\Omega_E} - \langle[\![\bar{w}]\!], \{\!\{\nabla\bar{u}\}\!\}\rangle_\Gamma - \langle\{\!\{\nabla\bar{w}\}\!\}, [\![\bar{u}]\!]\rangle_\Gamma + \langle\eta h^{-1}[\![\bar{w}]\!], [\![\bar{u}]\!]\rangle_\Gamma \\ + \langle\eta h^{-1}\bar{w}, \bar{u}\rangle_{\partial\Omega} - \langle\nabla\bar{w}\cdot n, \bar{u}\rangle_{\partial\Omega} - \langle\bar{w}, \nabla\bar{u}\cdot n\rangle_{\partial\Omega} \\ = (\bar{w}, f)_{\Omega_E} - \langle\nabla\bar{w}\cdot n, u_D\rangle_{\partial\Omega} + \langle\eta h^{-1}\bar{w}, u_D\rangle_{\partial\Omega} \qquad \forall\,\bar{w}\in\bar{\mathcal{V}}\end{aligned} \tag{3.47}$$

Eq. (3.47) no longer pointwise satisfies the fine scale surface model that has been obtained earlier. Recall that the fine scale surface model is required to make the split into a coarse scale and a fine scale solution well posed. Pointwise enforcement of these models would over constrain the problem. Instead a weakly satisfied fine scale surface model is required. By comparing Eq. (3.47) to Eq. (3.45) the following identity is implicitly satisfied.

$$\begin{aligned}-(\Delta\bar{w}, u')_{\Omega_E} - \langle\bar{w}, \nabla u'\cdot n\rangle_{\partial\Omega} - \langle[\![\bar{w}]\!], \{\!\{\nabla u'\}\!\}\rangle_\Gamma + \langle\nabla\bar{w}\cdot n, u'\rangle_{\partial\Omega} \\ + \langle[\![\nabla\bar{w}]\!], \{\!\{u'\}\!\}\rangle_\Gamma = \langle\eta h^{-1}[\![\bar{w}]\!], [\![\bar{u}]\!]\rangle_\Gamma - \langle\eta h^{-1}\bar{w}, u'\rangle_{\partial\Omega} \qquad \forall\,\bar{w}\in\bar{\mathcal{V}}\end{aligned} \tag{3.48}$$

In a multidimensional case this *is* the fine scale model. While more illusive than those obtained for the 1D case, it does provide some tangible insight into the fine scale behavior. For instance by taking a test function $\bar{w}$ that equals 1 in the element K and 0 outside of this element:

$$\int_{\partial K} \{\!\{\nabla u'\}\!\}\cdot n = -\int_{\partial K} \eta h^{-1}[\![u']\!] \tag{3.49}$$

Where $\{\!\{\nabla u'\}\!\} \equiv \nabla u'$ and $[\![u']\!] \equiv u'$ on the domain boundary. This identity looks much like the fine scale surface model for the 1D interior penalty case. Contrarily similar equations for the remaining fine scale model were not obtained, e.g.:

$$\begin{aligned}\int_{\partial K} \{\!\{u'\}\!\} &\neq 0 \\ \int_K u' &\neq 0\end{aligned} \tag{3.50}$$

These identities *are* satisfied for a 1D case, so their behavior in a multidimensional setting might prove insightful. To this end, weak formulation Eq. (3.47) is used to solve the problem shown in Figure 3.10. The finite element mesh consists of 18 triangular elements. The problem is solved while using basis functions of a range of polynomial orders. Figure 3.11 shows results obtained by using linear basis functions. Figures 3.12 and 3.13 are the results of using a $p = 2$ and $p = 4$ polynomial basis respectively. The integrals from Eqs. (3.49) and (3.50) are carried out on each separate element. The obtained values are collected in Table 3.3.

Model problem

$\Omega = [\,0\,,\,1\,] \times [\,0\,,\,1\,]$

$f = 0$ in Ω

$u = 0$ when $x_1 = 0$

$u = 0$ when $x_1 = 1$

$u = \sin(\pi\, x_1)$ when $x_2 = 0$

$u = 0$ when $x_2 = 1$

Exact solution

$$u(x_1, x_2) = \left(\cosh(\pi\, x_2) - \frac{\cosh(\pi)}{\sinh(\pi)} \sinh(\pi\, x_2)\right) \sin(\pi\, x_1)$$

Numerical implementation

Mesh: 18 triangular elements

Interior penalty method

$\eta_\Gamma = 3$

$\eta_{\partial\Omega} = 8$

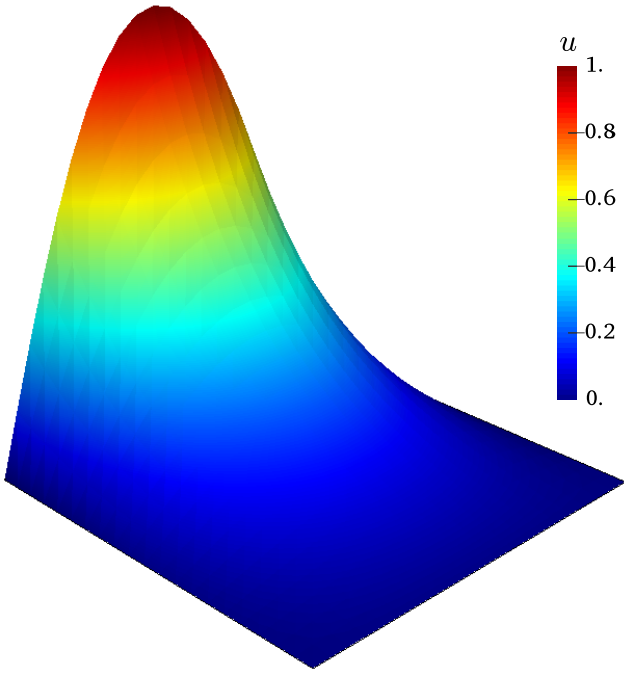

Fig. 3.10: *Exact solution of the 2D Laplace model problem.*

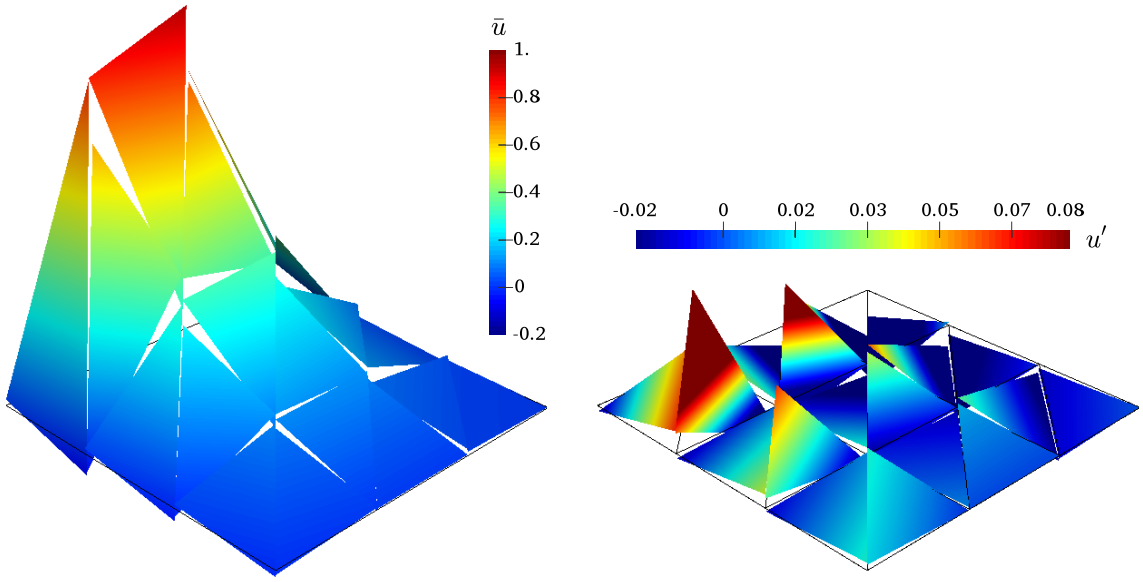

(a) Coarse scale solution $\bar{u}$.

(b) Fine scale solution u'.

Fig. 3.11: *Interior penalty method for a 2D Laplace problem with $p = 1$ discretization.*

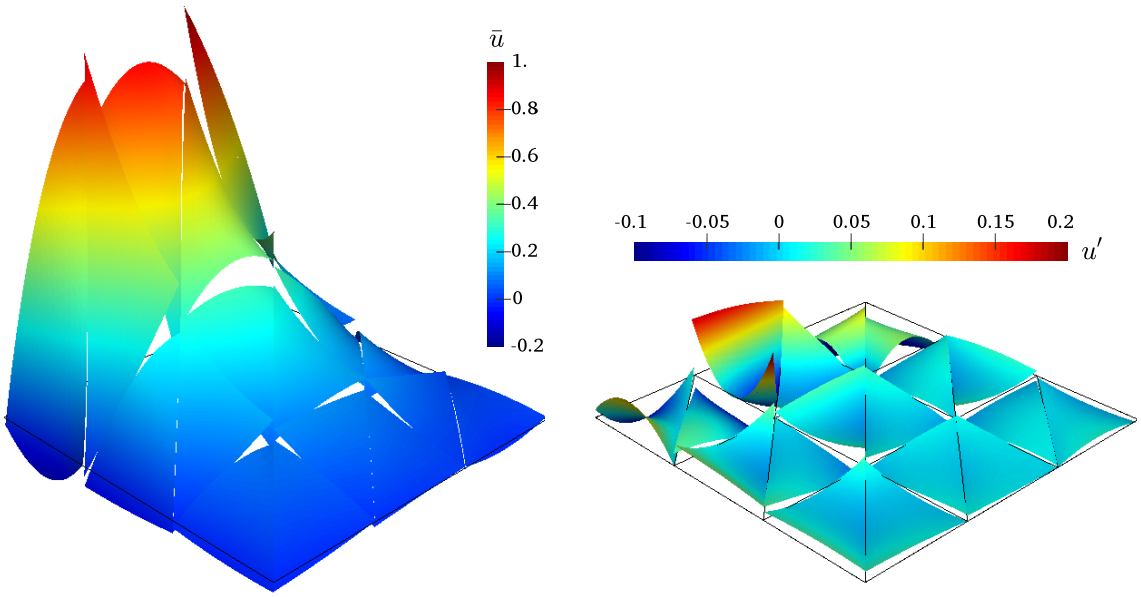

(a) Coarse scale solution $\bar{u}$. **(b)** Fine scale solution u'.

Fig. 3.12: *Interior penalty method for a 2D Laplace problem with $p = 2$ discretization.*

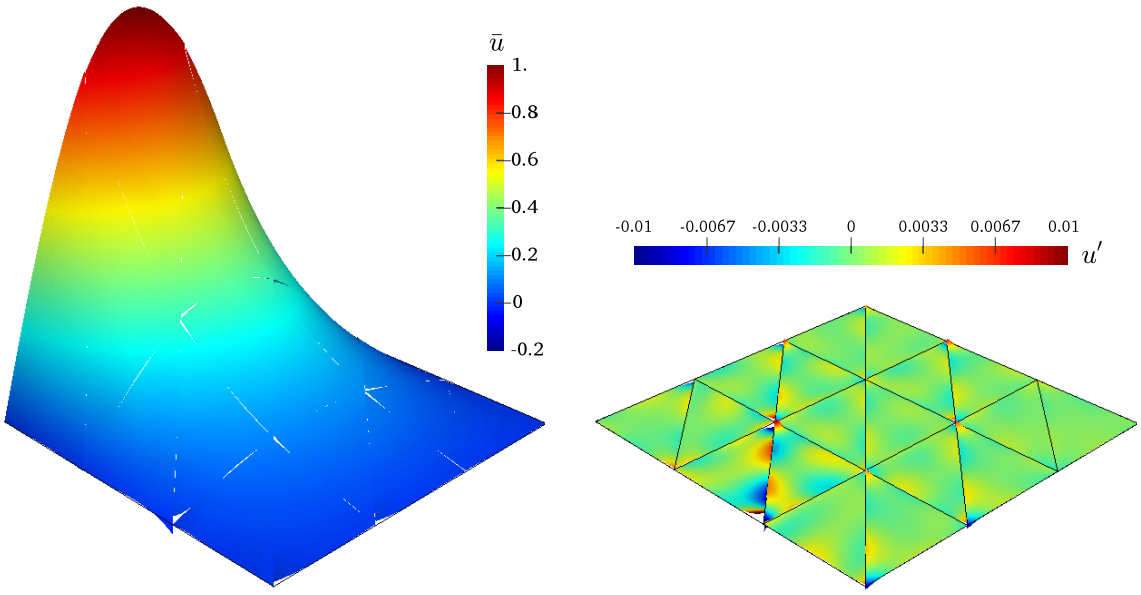

(a) Coarse scale solution $\bar{u}$. **(b)** Fine scale solution u'.

Fig. 3.13: *Interior penalty method for a 2D Laplace problem with $p = 4$ discretization.*

Table 3.3: *Integrals of Eqs.* (3.49) *and* (3.50) *for the interior penalty problem of Figure 3.10. Carried out for basis functions of* $p = 1$ *to* $p = 6$ *on the same computational mesh.*

	$\max_{K\in\mathcal{T}} \left\lvert \int_{\partial K} \{\!\{\nabla u'\}\!\} + \eta h^{-1} [\![\bar{u}]\!] \right\rvert$	$\frac{1}{\#\text{Els}} \sum_{K\in\mathcal{T}} \left\lvert \int_{\partial K} \{\!\{u'\}\!\} \right\rvert$	$\frac{1}{\#\text{Els}} \sum_{K\in\mathcal{T}} \left\lvert \int_{K} u' \right\rvert$
$p = 1$	0	$2.39 \cdot 10^{-3}$	$2.93 \cdot 10^{-4}$
$p = 2$	0	$1.81 \cdot 10^{-3}$	$1.98 \cdot 10^{-4}$
$p = 3$	0	$6.83 \cdot 10^{-5}$	$2.78 \cdot 10^{-6}$
$p = 4$	0	$2.22 \cdot 10^{-5}$	$2.04 \cdot 10^{-6}$
$p = 5$	0	$7.89 \cdot 10^{-7}$	$7.53 \cdot 10^{-9}$
$p = 6$	0	$3.31 \cdot 10^{-7}$	$3.59 \cdot 10^{-9}$

The results in Table 3.3 verify that the fine scale surface model of Eq. (3.49) is satisfied. Indeed the integrals from Eq. (3.50) do not equal zero. Interestingly these integrals decrease is a step-wise fashion. They reduce by two or three orders of magnitude for each subsequent odd polynomial order. In contrast they only reduce by an approximate factor of two when the polynomial order is increased from an odd order polynomial to an even order polynomial. This notable convergence behavior hints at a multidimensional extension of the small scale surface model Eq. (3.44) for a higher dimensional domain. A more thorough error analysis is required to fully understand this behavior.

3.3 The advection-diffusion problem

The same principle is applied to the advection-diffusion problem. Different from the Laplace operator, the DG method has no 'problem' with advection terms when upwind numerical fluxes are used. The purpose of this chapter is not to provide a better (or even alternative) method. Rather this chapter means to show that the framework also holds for this class of equations. Additionally, the volumetric fine scale term will not cancel for linear basis functions, so its effect can be evaluated. The following problem is considered.

$$\begin{cases} a \cdot \nabla u - \nu \Delta u = f & \text{in } \Omega \subset \mathbb{R}^d \\ u = u_D & \text{on } \partial\Omega \end{cases} \tag{3.51}$$

The parameters a and ν are assumed constant in the analysis.

3.3.1 A global coarse scale weak formulation

The process described in Section 3.1.3 is repeated. The first two steps lead to the per element coarse scale weak formulation. A summation over all elements in the mesh yields:

$$\begin{aligned}&\text{Find } \bar{u} \in \bar{\mathscr{V}}(u_D) \text{ s.t.:}\\ &-\left(a\cdot\nabla\bar{w},\bar{u}\right)_{\Omega_E}+\left(\nabla\bar{w},\nu\nabla\bar{u}\right)_{\Omega_E}+\sum_{K\in\mathscr{T}}\left[\left\langle\bar{w},a\cdot n\,\bar{u}\right\rangle_{\partial K}-\left\langle\bar{w},\nu\,\nabla\bar{u}\cdot n\right\rangle_{\partial K}\right]+\\ &\qquad\left(\mathscr{L}^*\bar{w},u'\right)_{\Omega_E}+\sum_{K\in\mathscr{T}}k(\bar{w},u';\partial K)=\left(\bar{w},f\right)_{\Omega_E}\qquad\forall\,\bar{w}\in\bar{\mathscr{V}}(0)\end{aligned}\tag{3.52}$$

Where for this problem

$$\mathscr{L}^*=-a\cdot\nabla-\nu\Delta\tag{3.53}$$

$$k(p,q;\partial K)=\left\langle p,a\cdot n\,q\right\rangle_{\partial K}-\left\langle p,\nu\,\nabla p\cdot n\right\rangle_{\partial K}+\left\langle\nabla q\cdot n,\nu\,p\right\rangle_{\partial K}\tag{3.54}$$

The global formulation is obtained by manipulation of the fine scale element boundary terms. Equation (3.12) is used in Eq. (3.54), which is subsequently substitution into Eq. (3.52) to obtain the following global weak formulation.

$$\begin{aligned}&\text{Find } \bar{u} \in \bar{\mathscr{V}}(u_D) \text{ s.t.:}\\ &-\left(a\cdot\nabla\bar{w},\bar{u}\right)_{\Omega_E}+\left\langle[\![\bar{w}]\!]\cdot a,\{\!\{\bar{u}\}\!\}\right\rangle_\Gamma+\left\langle[\![\bar{w}]\!]\cdot a,\{\!\{u'\}\!\}\right\rangle_\Gamma+\\ &\quad\left(\nabla\bar{w},\nu\nabla\bar{u}\right)_{\Omega_E}-\left\langle[\![\bar{w}]\!],\nu\,\{\!\{\nabla\bar{u}\}\!\}\right\rangle_\Gamma-\left\langle\{\!\{\nabla\bar{w}\}\!\},\nu\,[\![\bar{u}]\!]\right\rangle_\Gamma+\\ &\left(\mathscr{L}^*\bar{w},u'\right)_{\Omega_E}-\left\langle[\![\bar{w}]\!],\nu\,\{\!\{\nabla u'\}\!\}\right\rangle_\Gamma+\left\langle[\![\nabla\bar{w}]\!],\,\nu\,\{\!\{u'\}\!\}\right\rangle_\Gamma=\left(\bar{w},f\right)_{\Omega_E}\quad\forall\,\bar{w}\in\bar{\mathscr{V}}(0)\end{aligned}\tag{3.55}$$

The collection of the terms associated to the diffusion operator have been discussed in Section 3.2. An analogous approach results in the two advection terms. In particular the $\langle[\![\bar{w}]\!]\cdot a,\{\!\{\bar{u}\}\!\}\rangle_\Gamma$ term is obtained by using a manipulation similar to Eq. (3.30).

The numerical experiments will use linear basis functions for the coarse scale equation. Different from the implementation of the Poisson equation, the volumetric fine scale term does not disappear for the current problem. This is because the adjoint differential operator $\mathscr{L}^*$ includes a first derivative term. Therefore $\mathscr{L}^*\bar{w}$ can take nonzero values, even for linear basis functions.

In the section on the Poisson equation it was argued that omitting the volumetric fine scale term posed an additional condition on u' for basis functions of $p > 1$. However, in the advection-diffusion case this volumetric term already becomes important for $p = 1$ polynomials. Yet the fine scale problem is sufficiently constrained purely by the fine scale surface model. Therefore, exclusion of the volumetric fine scale term in the advection-diffusion case would attempt to over constrain the fine scale solution. Due to the resulting inconsistency the coarse scale solution effectively solves a different PDE. This is observed as an approximation error which becomes smaller as the residual becomes smaller, i.e., with mesh refinement. Potential improvement of the coarse scale solution can thus be expected when the volumetric fine scale term, or some model thereof, is included.

The solution for u' in the element interior is obtained by inverting the fine scale weak formulation (second line in Eq. (3.8)) by means of a fine scale Green's function. This is elaborated on in Appendix A. The appendix also describes that when linear basis functions and constant coefficients are used, then the fine scale term can be treated as a simple multiplication with a constant.

For linear basis functions, constant coefficients f, a and ν, and a 1D domain the term becomes:

$$\begin{aligned}(\mathscr{L}^*\bar{w}, u')_{\Omega_E} = \sum_{k\in\mathcal{T}} \Big[&\big(-a\cdot\nabla\bar{w}\,,\,\tau\,(f - a\cdot\nabla\bar{u})\big)_K + \\ &\big(-a\cdot\nabla\bar{w}, \gamma_0\nu\, n_j\, u'_j\big)_K + \big(-a\cdot\nabla\bar{w}, \gamma_1\nu\, n_{j+1}\, u'_{j+1}\big)_K\Big]\end{aligned} \tag{3.56}$$

The per-element constants τ, γ_0 and γ_1 are average quantities over the element boundary or volume. These are derived from the Green's function. The derivation of their expressions as per Eq. (3.57) is also left to Appendix A.

$$\tau = \frac{h}{2\,a} - \frac{\nu}{a^2} + \frac{h}{a\left(e^{\frac{a}{\nu}h} - 1\right)} \qquad \gamma_0 = \frac{\nu - a\,h - \nu e^{-\frac{a}{\nu}h}}{a\,h\,\nu\left(e^{-\frac{a}{\nu}h} - 1\right)} \qquad \gamma_1 = \frac{\nu + a\,h - \nu e^{\frac{a}{\nu}h}}{a\,h\,\nu\left(e^{\frac{a}{\nu}h} - 1\right)} \tag{3.57}$$

The normal vectors n_j and n_{j+1} in Eq. (3.56) are the left and right normals of the element of integration. Similarly the fine scale boundary values u'_j and u'_{j+1} corresponding to the left and right boundary of the element of integration. Just like $\{\!\{u'\}\!\}$ and $\{\!\{\nabla u'\}\!\}$ these are unknowns that need to be modeled or treated explicitly. In the following numerical experiments these will first be treated explicitly. This will serve to verify the methodology and the obtained formulation. In practical applications explicit treatment is not feasible. Instead implicit treatment is required, i.e., their values have to be related to $\bar{u}$ in some way. It will be shown in Section 3.3.4 that when an interior penalty, NIPG or Baumann-Oden treatment of the diffusion term is implemented, then even for an advection-diffusion problem the following fine scale surface model holds.

$$\{\!\{u'\}\!\}\Big|_{\hat{x}} = \Phi(\hat{x}) = 0 \qquad\qquad \hat{x}\in\Gamma \tag{3.58}$$

When this is used in Eq. (3.16) of step 5 of the DG-RVMS roadmap, then the fine scale boundary value is obtained as:

$$u'^{\pm}\Big|_{\hat{x}} = \frac{1}{2}[\![u']\!]\Big|_{\hat{x}}\cdot n^{\pm} = -\frac{1}{2}[\![\bar{u}]\!]\Big|_{\hat{x}}\cdot n^{\pm} \qquad\qquad \hat{x}\in\Gamma \tag{3.59}$$

And the volumetric fine scale model becomes

$$\begin{aligned}(\mathscr{L}^*\bar{w}, u')_{\Omega_E} = \sum_{k\in\mathcal{T}} \Big[&\big(-a\cdot\nabla\bar{w}\,,\,\tau\,(f - a\cdot\nabla\bar{u})\big)_K + \\ &\big(a\cdot\nabla\bar{w}\,,\,\gamma_0\nu\frac{1}{2}[\![\bar{u}]\!]\Big|_{x_j}\big)_K + \big(a\cdot\nabla\bar{w}\,,\,\gamma_1\nu\frac{1}{2}[\![\bar{u}]\!]\Big|_{x_{j+1}}\big)_K\Big]\end{aligned} \tag{3.60}$$

Again, this is an identity for constant coefficients and linear coarse scale basis functions on a 1D domain. Still it may inspire a suitable volumetric fine scale model for a problem that extends past these limitations. For instance Chapter 4 will use a similar model for a higher order discretization on a space-time domain.

3.3.2 Verification by means of numerical experiments

The numerical experiments presented in this section are similar to those performed for the Poisson model problem. The computations will be carried out on a 1D domain, discretized with linear basis functions. Again the experiments will aim to obtain H^1 and L^2 projections of the exact solution. The focus will be on the effect of the volumetric fine scale term, which canceled in the investigated Poisson computations. Explicit imposition of the fine scale surface terms will help verify weak formulation (3.55) as well as the volumetric fine scale term Eq. (3.56).

For the case where a nodally exact H^1 projection is sought, all nodal u' and $\{\!\{u'\}\!\}$ values are zero. This includes those corresponding to γ_0 and γ_1 in Eqs. (3.56) and (3.60). As such, the fine scale volumetric term is confined to the contribution associated with τ. The $\{\!\{\nabla u'\}\!\}$ term is again treated explicitly as was described in the section on the Poisson experiments. By using this model set-up the solution shown in Figure 3.14 is obtained.

Model problem

$f = 6,\ a = 0.5,\ \nu = 0.15$

$x_0 = 0,\ x_1 = 1$

$u_0 = 0,\ u_1 = 2$

Exact solution

$$u(x) = -\frac{10}{e^{\frac{1}{0.3}} - 1}\left(e^{\frac{x}{0.3}} - 1\right) + 12x$$

Fine scale model

For $\hat{x} \in \Gamma$:

$$\{\!\{u'\}\!\}\Big|_{\hat{x}} = 0$$

$$\{\!\{\nabla u'\}\!\}\Big|_{\hat{x}} = \frac{\mathrm{d}}{\mathrm{d}x}u(x)\Big|_{\hat{x}} - \frac{u(\hat{x}+h) - u(\hat{x}-h)}{2h}$$

$$u'(\hat{x}) = 0$$

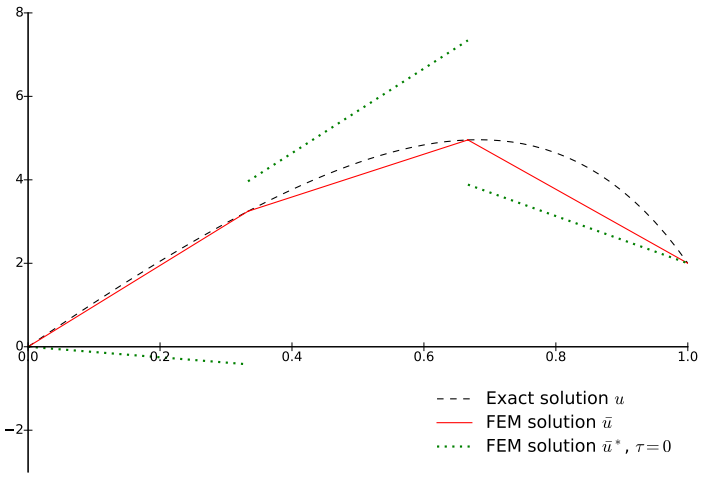

Fig. 3.14: *Nodally exact $\bar{u}$ when an explicit formulation for $\{\!\{\nabla u'\}\!\}$ is implemented.*

Figure 3.14 verifies that the H^1 projection is retrieved given this model set-up. Additionally, it shows the importance of the volumetric fine scale term; when this is omitted by setting $\tau = 0$ the solution behaves unstable. Small changes in ν lead to wildly varying solutions. Unstable behavior of finite element approximations to advection-diffusion equations is a known phenomenon, and prompted the use of upwind numerical fluxes. Section 3.3.3 will go into the nature of the effectiveness of upwind methods, and will additionally show that upwind methods implicitly constitute a fine scale surface model.

The H^1 computation explicitly used $u' = 0$ on element boundaries. This canceled the effect of the γ terms in Eq. (3.56). To verify the occurrence of these γ terms, an L^2 projection of an exact solution will be retrieved. The L^2 projection of the solution no longer yields a nodally exact $\bar{u}$. As such, the fine scale boundary terms can no longer be omitted. Instead the fine scale terms are implemented explicitly where their values and derivatives are obtained

from a precomputed L^2 projection. The same procedure was proposed for the Poisson model problem. The result is shown in Figure 3.15.

Model problem

$$f = 6,\ a = 0.5,\ \nu = 0.15$$
$$x_0 = 0,\ x_1 = 1$$
$$u_0 = 0,\ u_1 = 2$$

Exact solution

$$u(x) = -\frac{10}{e^{\frac{1}{0.3}} - 1}\left(e^{\frac{x}{0.3}} - 1\right) + 12x$$

Fine scale model

For $\hat{x} \in \Gamma$:

$$\{\!\{u'\}\!\}\Big|_{\hat{x}} = u(\hat{x}) - \{\!\{\mathcal{P}_{L^2} u\}\!\}\Big|_{\hat{x}}$$
$$\{\!\{\nabla u'\}\!\}\Big|_{\hat{x}} = \nabla u(\hat{x}) - \{\!\{\nabla \mathcal{P}_{L^2} u\}\!\}\Big|_{\hat{x}}$$
$$u'\big(\lim_{\epsilon \to 0} \hat{x} \pm \epsilon\big) = u(\hat{x}) - \mathcal{P}_{L^2} u\big(\lim_{\epsilon \to 0} \hat{x} \pm \epsilon\big)$$

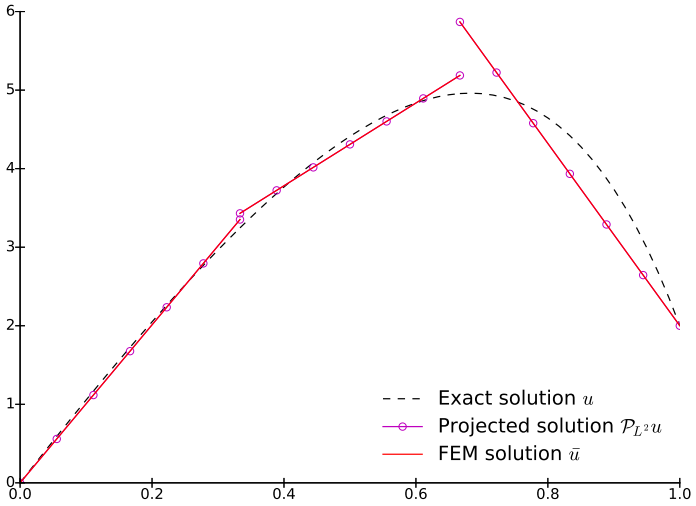

Fig. 3.15: *The L^2 projection of u is obtained with the explicit description for the fine scale terms.*

Figure 3.15 shows that the L^2 projection of the exact solution is indeed retrieved by consistent and explicit substitution of the fine scale surface terms. This strongly hints at the validity of all the fine scale terms in weak formulation (3.55), and of the proposed DG-RVMS solution strategy in general.

The experiments proposed in this section all produced results in line with the DG-RVMS theory. On top of the element boundary fine scale terms that were investigated earlier, now also the volumetric fine scale term had to be included. The first numerical experiment showed that the omission of the volumetric fine scale term produces highly inaccurate results. A remedy for this problem is the use of upwind numerical fluxes. These will be investigated in the next section from a residual-based variational multiscale point of view.

3.3.3 Recollection of classical discontinuous Galerkin formulations

The formulation that is obtained by using the DG-RVMS method (Eq. (3.55)) suggests the use of average quantities as coarse scale element boundary conditions. Yet upwinding methods have been the backbone of DG methods since their first introduction in 1973 by Reed and Hill [57]. This section will aim to investigate what fine scale surface models are implicitly enforced by using classical upwind strategies. In practice the fine scale surface models associated to the advection operator are not stand-alone. They combine with those associated to the diffusion operator. Any fine scale model will have an effect on both sets of terms. An advection dominated case is considered to make claims on the fine scale surface model corresponding to upwind numerical fluxes. This is of special interest since advection dominated flow is often a problematic case for finite element implementations. The final section will

touch upon the implications of combining different fine scale models, e.g. combining an interior penalty method with the use of upwind fluxes.

The use of upwind values for the element interior boundary conditions is in line with the physical interpretation of the advection term. Information is propagated in the direction of the advection velocity vector, so the element boundary data of some element in the mesh comes from the upstream element. The flux term obtained from integration by parts of the coarse scale solution would be of the form shown in Eq. (3.61). The jumps in $\bar{w}$ are obtained because $\bar{u}(\lim_{\epsilon\to 0} x - \epsilon a)$ is single valued on the element interface.

$$\left\langle [\![\bar{w}]\!] \cdot a, \bar{u}(\lim_{\epsilon\to 0} x - \epsilon a) \right\rangle_\Gamma \tag{3.61}$$

This term replaces the per-element boundary condition obtained for the advection component in the exact weak formulation. The finite element formulation is obtained by the substitution of Eq. (3.62) in the exact weak formulation of Eq. (3.55).

$$\left\langle [\![\bar{w}]\!] \cdot a, \{\!\{\bar{u}\}\!\} \right\rangle_\Gamma + \left\langle [\![\bar{w}]\!] \cdot a, \{\!\{u'\}\!\} \right\rangle_\Gamma = \left\langle [\![\bar{w}]\!] \cdot a, \bar{u}(\lim_{\epsilon\to 0} x - \epsilon a) \right\rangle_\Gamma \tag{3.62}$$

An example computation that makes use of this type of numerical flux is shown in Figure 3.16. It concerns an advection dominated case. The remaining fine scale terms from the diffusion operator are treated similar to those discussed for the H^1 numerical experiment earlier. Indeed the figure shows a coarse scale solution $\bar{u}$ that is nodally exact. When the fine scale volumetric term is omitted, i.e., $\tau = 0$, then the solution loses all accuracy. Similar behavior was reported for the earlier numerical experiment. However, the solution becomes radically more accurate when an upwind numerical flux is used, even when $\tau = 0$.

Model problem

$f = 6,\ a = 0.5,\ \nu = 0.001$

$x_0 = 0,\ x_1 = 1$

$u_0 = 0,\ u_1 = 2$

Exact solution

$$u(x) = -\tfrac{10}{e^{500}-1}\left(e^{500x} - 1\right) + 12x$$

Fine scale model

For $\hat{x} \in \Gamma$:

$$\{\!\{u'\}\!\}\Big|_{\hat{x}} = 0$$

$$\{\!\{\nabla u'\}\!\}\Big|_{\hat{x}} = \tfrac{\mathrm{d}}{\mathrm{d}x}u(\hat{x})\Big|_{\hat{x}} - \tfrac{u(\hat{x}+h)-u(\hat{x}-h)}{2h}$$

$$u'(\hat{x}) = 0$$

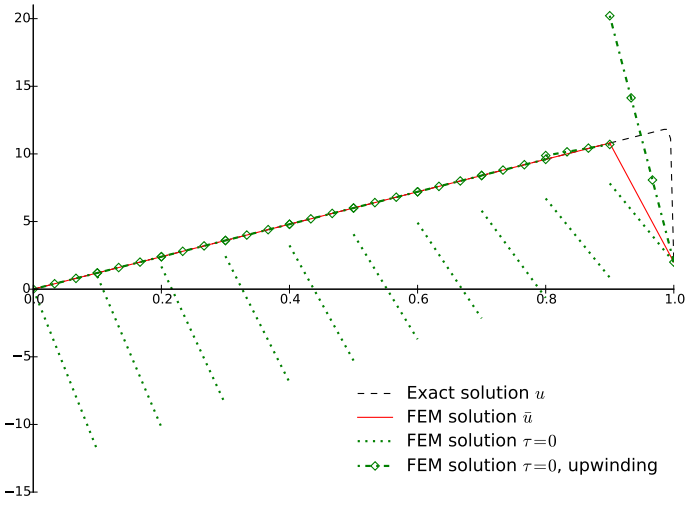

Fig. 3.16: *Comparison between upwinding and the use of the volumetric τ term. Using 10 elements.*

Before the actual fine scale surface model is derived, first a more conceptual argumentation on the effectiveness of upwind methods will be proposed. The advective nature of the PDE

pushes the solution u to the right. Towards the right boundary the diffusion term becomes dominant as high second derivatives are required to satisfy the boundary condition. This solution behavior can be observed in Figure 3.16. The complex behavior on the right part of the domain results in high residuals. This can be verified by examining the solution $\bar{u}$ in the rightmost element. It has a negative slope, whereas f is positive. Therefore, the residual $\mathscr{R}_{\bar{u}} = f - a \cdot \nabla \bar{u}$ is large. However, in all the remaining elements the slope of the coarse scale solution are such that the residual is nearly zero. The upwind method sweeps through the mesh, from left to right. Since the residuals are low on the left the solution error due to omission of the volumetric fine scale term is small. The subsequent element uses the previous element boundary values $\bar{u}$ as boundary conditions, which was sufficiently accurate. From this observation it can be concluded that the use of upwind numerical fluxes is effectively a *remedy* for the lack of the volumetric fine scale term.

On top of mediating the problematic distribution of the residual, the use of upwind numerical fluxes also implicitly constitute a fine scale surface model. The model can be obtained by manipulating the identity in Eq. (3.62). From this equation it follows that the fine scale term acts as the difference between the upwind term and the average term. Depending on the direction of a this can be split up in two cases: an a that points into the element denoted K^+ (meaning $a \cdot n^+ < 0$) and an a that points out of that element and into K^- (and thus $a \cdot n^+ > 0$).

$a \cdot n^+ < 0$	$a \cdot n^+ > 0$
$\langle [\![\bar{w}]\!] \cdot a, \bar{u}(\lim_{\epsilon \to 0} x - \epsilon a) - \{\!\{\bar{u}\}\!\} \rangle_\Gamma =$	$\langle [\![\bar{w}]\!] \cdot a, \bar{u}(\lim_{\epsilon \to 0} x - \epsilon a) - \{\!\{\bar{u}\}\!\} \rangle_\Gamma =$
$\langle [\![\bar{w}]\!] \cdot a, \bar{u}^- - \frac{1}{2}(\bar{u}^+ + \bar{u}^-) \rangle_\Gamma =$	$\langle [\![\bar{w}]\!] \cdot a, \bar{u}^+ - \frac{1}{2}(\bar{u}^+ + \bar{u}^-) \rangle_\Gamma =$
$\frac{1}{2} \langle [\![\bar{w}]\!] \cdot a, -\bar{u}^+ + \bar{u}^- \rangle_\Gamma =$	$\frac{1}{2} \langle [\![\bar{w}]\!] \cdot a, \bar{u}^+ - \bar{u}^- \rangle_\Gamma =$
$\frac{1}{2} \langle [\![\bar{w}]\!] \cdot a, n^- \cdot n^+ \bar{u}^+ + n^- \cdot n^- \bar{u}^- \rangle_\Gamma =$	$\frac{1}{2} \langle [\![\bar{w}]\!] \cdot a, n^+ \cdot n^+ \bar{u}^+ + n^+ \cdot n^- \bar{u}^- \rangle_\Gamma =$
$\frac{1}{2} \langle [\![\bar{w}]\!], [\![\bar{u}]\!] \, a \cdot n^- \rangle_\Gamma =$	$\frac{1}{2} \langle [\![\bar{w}]\!], [\![\bar{u}]\!] \, a \cdot n^+ \rangle_\Gamma =$
$\frac{1}{2} \langle [\![\bar{w}]\!], [\![\bar{u}]\!] \, \lvert a \cdot n \rvert \rangle_\Gamma$	

(3.63)

As such, in either case the fine scale model can be retrieved from the following equality:

$$
\begin{aligned}
\langle [\![\bar{w}]\!] \cdot a, \{\!\{u'\}\!\} \rangle_\Gamma &= \frac{1}{2} \langle [\![\bar{w}]\!], [\![\bar{u}]\!] \, \lvert a \cdot n \rvert \rangle_\Gamma \\
\langle [\![\bar{w}]\!], (u'^+ + u'^-) \, a \rangle_\Gamma &= -\langle [\![\bar{w}]\!], (u'^+ n^+ + u'^- n^-) \lvert a \cdot n \rvert \rangle_\Gamma \\
\langle [\![\bar{w}]\!], a u'^+ + a u'^- + \lvert a \cdot n \rvert \, u'^+ n^+ + \lvert \, a \cdot n \rvert u'^- n^- \rangle_\Gamma &= 0 \\
\langle [\![\bar{w}]\!], a \cdot n^+ \, u'^+ - a \cdot n^- u'^- + \lvert a \cdot n \rvert \, u'^+ - \lvert a \cdot n \rvert \, u'^- \rangle_\Gamma &= 0 \\
\langle [\![\bar{w}]\!], (a \cdot n^+ + \lvert a \cdot n \rvert) \, u'^+ - (a \cdot n^- + \lvert a \cdot n \rvert) \, u'^- \rangle_\Gamma &= 0
\end{aligned}
\tag{3.64}
$$

When a points out of K^- and into K^+, then $a \cdot n^+ < 0$ and $a \cdot n^+ + \lvert a \cdot n \rvert = 0$ which means that the fine scale component u^+ is removed from the identity. If instead a points into K^-

and out of K^+ then $a \cdot n^- + |a \cdot n| = 0$ and the fine scale component u^- vanishes. As such, the fine scale model (3.65) is obtained.

$$\begin{cases} \langle [\![\bar{w}]\!],\, u'^+ \rangle_\Gamma = 0 \quad \Rightarrow \quad \langle [\![\bar{w}]\!],\, \bar{u}^+ \rangle_\Gamma = \langle [\![\bar{w}]\!],\, u \rangle_\Gamma & \text{when } a \cdot n^+ > 0 \\ \langle [\![\bar{w}]\!],\, u'^- \rangle_\Gamma = 0 \quad \Rightarrow \quad \langle [\![\bar{w}]\!],\, \bar{u}^- \rangle_\Gamma = \langle [\![\bar{w}]\!],\, u \rangle_\Gamma & \text{when } a \cdot n^- > 0 \end{cases} \tag{3.65}$$

This model only enforces a condition on u' on parts of the element boundary, namely the sides where the advection velocity vector is pointing out of the element. The fine scale solution is left condition-free at sides where the vector is pointing inwards. This is in line with the mathematically required boundary conditions for a pure advection problem. This becomes particularly clear when the advection dominated 1D case is considered. The weak conditions become strong pointwise per-element boundary conditions:

$$\begin{cases} u'^+(x) = 0 \quad \Rightarrow \quad \bar{u}^+(x) = u(x) & \text{for } x \in \Gamma \text{ when } a \cdot n^+ > 0 \\ u'^-(x) = 0 \quad \Rightarrow \quad \bar{u}^-(x) = u(x) & \text{for } x \in \Gamma \text{ when } a \cdot n^- > 0 \end{cases} \tag{3.66}$$

For a positive a this means that the use of upwinding effectively enforces the fine scale condition $u' = 0$ on the right nodes of the elements. In turn this means that the finite element solution $\bar{u}$ becomes the exact solution u at this node.

As an example the pure advection problem of Eq. (3.67) is considered. Only a single boundary condition is required to determine the constant of integration. The upwind method thus aims to set this per-element required single boundary condition to the true solution value. This boundary condition is set at the outflow boundary. The value at the outflow boundary of the one element is the boundary condition of the neighboring element. Thereby, the correct solution is propagated through the domain.

$$\frac{\mathrm{d}}{\mathrm{d}x} u = f \quad \Rightarrow \quad u = \int f + C \tag{3.67}$$

The just described nodal exactness is often not observed in upwind computations. See for example Figure 3.16. The upwind finite element result shows clear deviation from the exact solution around the right boundary condition. This is due to the exclusion of the volumetric fine scale term. It was argued in Section 3.3.1 that this results in an approximation error. Therefore, a residual-based volumetric fine scale model can prove valuable, even in a DG environment.

In practical applications there will almost always be some diffusive effect. Even in the case of Figure 3.16 the second derivatives become so large towards the right boundary that the diffusion term takes effect. In these cases the upwind fine surface scale model combines with those proposed for the Laplace operator.

3.3.4 Combining fine scale surface models

The analysis in the previous section dealt with advection dominated flow and upwind numerical fluxes. However, the fine scale surface model that was derived for such a case does not correspond well to the models derived in Section 3.2.3. For instance the interior penalty treatment of the diffusion term implies $\{\!\{u'\}\!\} = 0$ and $\{\!\{\nabla u'\}\!\} = -\eta h^{-1} [\![\bar{u}]\!]$, while the

use of upwind fluxes in a purely advective case implied $u' = 0$ on element outflow boundaries. There is too little approximation freedom to enforce all these conditions separately. Instead certain conditions combine to form a new fine scale surface model.

Two different cases are investigated. First, an interior penalty formulation is used to deal with the second order elliptic operator, and secondly, a Baumann-Oden implementation is looked at. Both formulations use upwind numerical fluxes for the advection part of the equation. The fine scale surface model for both these cases is derived.

Interior penalty and upwinding

The exact variational multiscale weak formulation (3.55) is equated to an interior penalty & upwind finite element formulation. Once the identical terms on either side of the equation are subtracted, the following identity remains. Note that it is assumed that the volumetric fine scale term is treated correctly in the finite element formulation. This means that the volumetric fine scale model of Eq. (3.60) is implemented.

$$\begin{aligned}\langle [\![\nabla \bar{w}]\!], \nu \{\!\{u'\}\!\} \rangle_\Gamma + \langle [\![\bar{w}]\!], a \{\!\{\bar{u}\}\!\} \rangle_\Gamma + \langle [\![\bar{w}]\!], a \{\!\{u'\}\!\} \rangle_\Gamma - \langle [\![\bar{w}]\!], \nu \{\!\{\nabla u'\}\!\} \rangle_\Gamma = \\ \langle [\![\bar{w}]\!], a\, \bar{u}(\lim_{\epsilon \to 0} x - \epsilon a) \rangle_\Gamma + \langle [\![\bar{w}]\!], \nu \eta h^{-1} [\![\bar{u}]\!] \rangle_\Gamma \quad \forall\, \bar{w} \in \bar{\mathcal{V}}(0)\end{aligned} \tag{3.68}$$

All terms are moved to the left hand side and collected according to matching test function operations. The upwind terms from the advection operator simplifies to the term obtained in Eq. (3.63).

$$\langle [\![\nabla \bar{w}]\!], \nu \{\!\{u'\}\!\} \rangle_\Gamma + \langle [\![\bar{w}]\!], a \{\!\{u'\}\!\} - \frac{1}{2} [\![\bar{u}]\!]\, |a \cdot n| - \nu \{\!\{\nabla u'\}\!\} - \nu \eta h^{-1} [\![\bar{u}]\!] \rangle_\Gamma = 0 \tag{3.69}$$

The 1D case is investigated. As shown in Appendix C the 1D setting requires each term that corresponds to a different test function operator to equal zero individually. This leaves the following identities:

$$\begin{cases} \{\!\{u'\}\!\}\Big|_{\hat{x}} = 0 & \hat{x} \in \Gamma \\ \nu \{\!\{\nabla u'\}\!\}\Big|_{\hat{x}} = -(\frac{1}{2}|a \cdot n| + \nu \eta h^{-1}) [\![\bar{u}]\!]\Big|_{\hat{x}} & \hat{x} \in \Gamma \end{cases} \tag{3.70}$$

The identity $[\![\bar{u}]\!] = -[\![u']\!]$ is used to write the second equation purely in terms of fine scale components. The average and jump operators are expanded in terms of the neighboring element values.

$$\left(\frac{1}{2}|a \cdot n| + \nu \eta h^{-1}\right) u'^{+} n^{+} - \frac{1}{2} \nu \nabla u'^{+} = -\left(\frac{1}{2}|a \cdot n| + \nu \eta h^{-1}\right) u'^{-} n^{-} + \frac{1}{2} \nu \nabla u'^{-} \tag{3.71}$$

Note that both sides are vector quantities. The left hand side is dotted with n^+ and the right hand side with $-n^- = n^+$.

$$\left(\frac{1}{2}|a\cdot n| + \nu\eta h^{-1}\right) u'^{+} - \frac{1}{2}\nu\nabla u'^{+} n^{+} = \left(\frac{1}{2}|a\cdot n| + \nu\eta h^{-1}\right) u'^{-} - \frac{1}{2}\nu\nabla u'^{-} n^{-} \tag{3.72}$$

This equation can be written in the following simplified form.

$$u'^{+} - d\,\nabla u'^{+} n^{+} = u'^{-} - d\,\nabla u'^{-} n^{-} \tag{3.73}$$

Where:

$$d = \frac{h}{2\eta + |a\cdot n|\nu^{-1}h} \tag{3.74}$$

This fine scale surface model has been encountered before. It is exactly the model that was derived for the interior penalty method in the case of a pure diffusion problem: Eqs. (3.36) and (3.37). The same interpretation holds. The first order Taylor approximation of the fine scale solution field at a distance d from the element boundary is equal.

Figure 3.17 shows a model computation executed with an interior penalty and upwind implementation. The fine scale volumetric term was treated implicitly by using Eq. (3.60). The figure shows the resulting coarse and fine scale solutions. It shows that the fine scale solution does indeed behave as described in Eqs. (3.70) and (3.74).

Model problem

$f = 6,\ a = -0.5,\ \nu = 0.15$

$x_0 = 0,\ x_1 = 0.9$

$u_0 = 0,\ u_1 = 2$

$d = 0.1$

Exact solution

$$u(x) = \frac{u_1 - \frac{f}{a}x_1}{e^{\frac{a}{\nu}x_1} - 1}\left(e^{\frac{a}{\nu}x} - 1\right) + \frac{f}{a}x$$

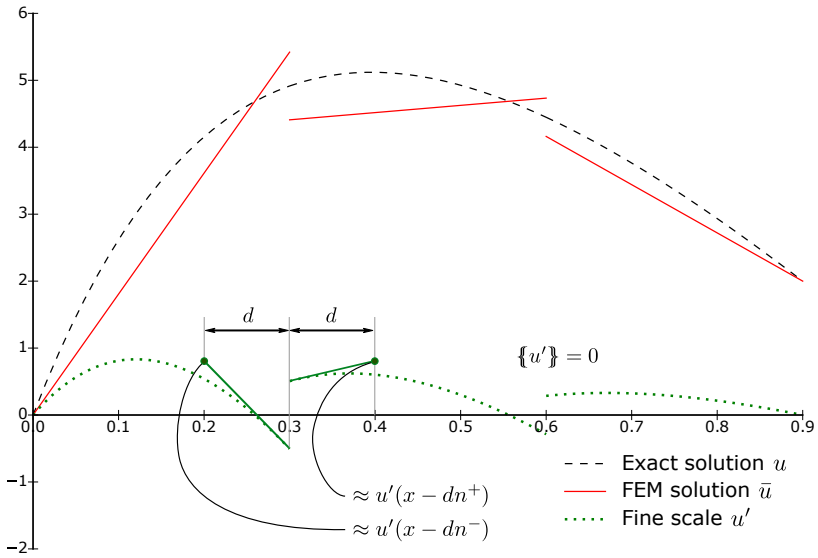

Fig. 3.17: *Illustration of the fine scale surface model when using an upwind flux in combination with an interior penalty method.*

Baumann-Oden and upwinding

When the interior penalty formulation is replaced by a Baumann-Oden implementation then Eq. (3.70) changes to the following.

$$\begin{cases} \{\!\{u'\}\!\}\Big|_{\hat{x}} = 0 & \hat{x} \in \Gamma \\ \nu\{\!\{\nabla u'\}\!\}\Big|_{\hat{x}} = -\frac{1}{2}\left|a \cdot n\right| [\![\bar{u}]\!]\Big|_{\hat{x}} - 2\nu\{\!\{\nabla \bar{u}\}\!\}\Big|_{\hat{x}} & \hat{x} \in \Gamma \end{cases} \tag{3.75}$$

Again the identity $[\![\bar{u}]\!] = -[\![u']\!]$ is substituted into the second line, and the resulting equation is written in terms of the per-element boundary values.

$$\frac{1}{2}|a \cdot n|\, u'^{+} n^{+} - \frac{1}{2}\nu \nabla u'^{+} - \nu \nabla \bar{u}^{+} = -\frac{1}{2}|a \cdot n|\, u'^{-} n^{-} + \frac{1}{2}\nu \nabla u'^{-} + \nu \nabla \bar{u}^{-} \tag{3.76}$$

By dotting the left hand side with n^{+} and the right hand side with $-n^{-} = n^{+}$:

$$\frac{1}{2}|a \cdot n|\, u'^{+} - \frac{1}{2}\nu \nabla u'^{+} \cdot n^{+} - \nu \nabla \bar{u}^{+} \cdot n^{+} = \frac{1}{2}|a \cdot n|\, u'^{-} - \frac{1}{2}\nu \nabla u'^{-} \cdot n^{-} - \nu \nabla \bar{u}^{-} \cdot n^{-} \tag{3.77}$$

The boundary values $\nabla \bar{u}^{\pm}$ are written as $\nabla u - \nabla u'^{\pm}$ whereby the fine scale surface model becomes independent of the coarse scale solution.

$$\frac{1}{2}|a \cdot n|\, u'^{+} + \frac{1}{2}\nu \nabla u'^{+} \cdot n^{+} - \nu \nabla u \cdot n^{+} = \frac{1}{2}|a \cdot n|\, u'^{-} + \frac{1}{2}\nu \nabla u'^{-} \cdot n^{-} - \nu \nabla u \cdot n^{-} \tag{3.78}$$

Dividing by $\frac{1}{2}|a \cdot n|$ and subsequent subtraction of u on both sides of the equation yields the following model.

$$u'^{+} - d\, \nabla u'^{+} \cdot n^{+} - \, u + 2d\, \nabla u \cdot n^{+} = u'^{-} - d\, \nabla u'^{-} \cdot n^{-} - u + 2d\, \nabla u \cdot n^{-} \tag{3.79}$$

Where:

$$d = -\frac{\nu}{|a \cdot n|} \tag{3.80}$$

This is again a fine scale surface model that has been seen before, namely the one corresponding to the NIPG method in Eqs. (3.38) and (3.40). The interpretation was that the fine scale solution fields extrapolated a distance d past the element boundary are offset by the same first order Taylor extrapolation of the exact solution at twice that distance. A numerical experiment is again performed. The coarse and fine scale solutions shown in Figure 3.18 are obtained. They do indeed correspond to the model of Eqs. (3.75) and (3.79).

The distance d is a measure of the constraint on the fine scale solution. As d decreases the fine scale boundary values decrease, and the coarse scale solution approaches a nodally exact solution. Interestingly d becomes smaller as the advective velocity increases. As such, the Baumann-Oden treatment of the Laplace operator appears to be a suitable choice for advection dominated problems. This stands in contrast to the curious behavior when it is implemented for a pure Poisson equation.

Model problem

$f = 6,\ a = -1.5,\ \nu = 0.15$

$x_0 = 0,\ x_1 = 0.9$

$u_0 = 0,\ u_1 = 2$

$d = -0.1$

Exact solution

$$u(x) = \frac{u_1 - \frac{f}{a}x_1}{e^{\frac{a}{\nu}x_1} - 1}\left(e^{\frac{a}{\nu}x} - 1\right) + \frac{f}{a}x$$

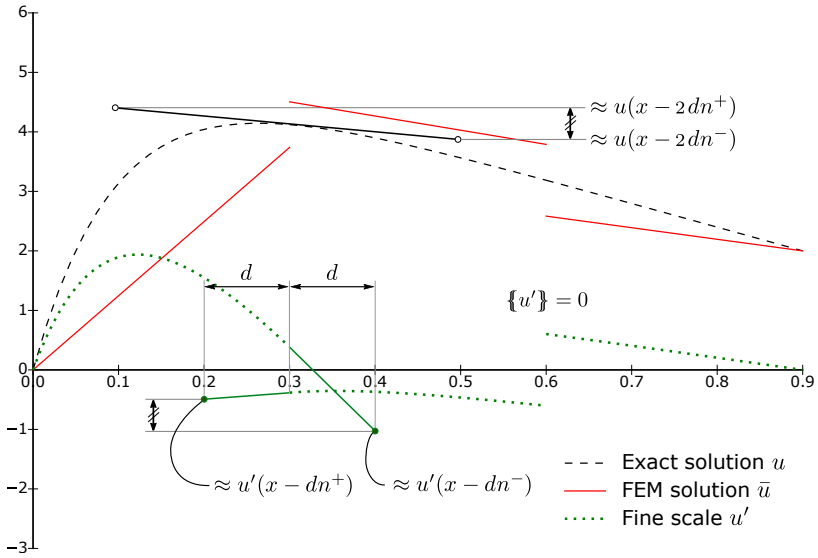

Fig. 3.18: *Illustration of the fine scale surface model when using an upwind flux in combination with a Baumann-Oden method.*

The understanding of this type of behavior follows directly from the DG-RVMS methodology developed in this chapter. In summary the DG-RVMS method introduces two new concepts by which DG formulations may be better understood, or even improved. These are the fine scale surface model, and the fine scale volumetric model. A fine scale surface model is required to obtain a well posed weak formulation. At the same time it dictates the behavior of the coarse scale solution. Additionally, the fine scale volumetric model needs to be incorporated to suppress the approximation error. The volumetric fine scale term is the true missing term in typical finite element formulation. This section has shown that the expected coarse scale solution is obtained by correct incorporation of the fine scale volumetric model. For more complex PDEs, and more complex discretizations, the volumetric term needs to be approximated. In the next chapter the performance of a DG implementation that does include an approximate fine scale volumetric model is investigated. For this purpose the Burgers equation is considered.

Chapter 4

A more complex example: The Burgers equation

The foundation of the DG-RVMS method has been firmly developed in the previous chapter. In the current chapter its extension to a more complex PDE is investigated. The same strategy will be applied to a 1D viscous Burgers equation. The viscous Burgers equation is a nonlinear, hyperbolic, transient, second order PDE. It will be discretized with higher order polynomial basis functions. As such, the proposed DG-RVMS framework requires a number of approximations. It will turn out that despite these approximations the DG-RVMS method yields a significant performance boost. In particular, the relative error in total energy in the final solution field is decreases by almost an order of magnitude. This performance boost is observed for a wide range of discretizations and for a number of polynomial order basis functions.

The chapter begins with a general review of the Burgers equation in a finite element setting. The turbulent behavior exhibited by the Burgers equation is discussed. This behavior lies at the core of the scale interaction of the PDE. Next, a space-time weak formulation is proposed. It will serve as the basis for all further finite element formulations. In practice an explicit Runge-Kutta time integration scheme is used for all computations. Therefore, the section also includes the formalism of going from the space-time formulation, to an implementation that uses a finite-difference scheme in time and a finite element method in space. Finally, a reference solution is constructed. Based on this solution further numerical experiments will be evaluated.

The first VMS model that is investigated is a three-scale formulation in a continuous Galerkin implementation. The fine scale effects are modeled by making use of an eddy viscosity model. This is thus not an residual-based fine scale model. Instead this formulation deals with the scale interaction in a more direct way. The energy transfer between the different scales, including the fine scales, is more directly enforced. It is thus an insightful approach that will set a baseline for the potential performance increase of the residual-based models.

Next, a classical R-VMS model is implemented. In the previous chapter it was shown that the volumetric fine scale term in the DG-RVMS framework consists of the classical R-VMS

model, to which an additional term is added. The classical term will first be composed, and tested, for a separate R-VMS finite element implementation. According to Section 2.3 the classical R-VMS method requires a sufficiently smooth coarse scale function space. Therefore, the numerical experiments in Section 4.3 will make use of B-spline basis functions.

Finally, the DG case is considered in Section 4.4. The finite element formulation is developed from a VMS point-of-view, as proposed in the previous chapter. This will include the use of a fine scale surface model to make the formulations well posed. The R-VMS model designed in the prior section is complemented with the element surface terms. This yields the fine scale volumetric model for a discontinuous discretization.

Since the scale interaction for Burgers turbulence is interpreted as a transfer of energy, the energy in the solution field will be of prime interest. All three VMS-based implementations will be examined based on the same measures. These consist of an inspection of the final solution field, an analysis of the spectral energy decomposition of this solution, and an investigation of the convergence of the relative error in total energy. Thereby, a consistent picture of the behavior of the different VMS models is obtained. This will help to put the performance increase for the DG-RVMS approach into context.

4.1 An introduction to the Burgers equation

The Burgers equation lends its name from the Dutch physicist Johannes Martinus Burgers (1895-1981) [58]. He was a professor at Delft university of technology in his early career (at the time Technische Hogeschool Delft). Johannes' focus was on the field of aerodynamics. Indeed the Burgers equation can be considered a 1-dimensional model for pressureless gas dynamics [59]. This chapter will focus on a forced viscous Burgers equation on a 1-dimensional periodic domain. The equation reads:

$$\begin{cases} u_t + u\,u_x - \nu u_{xx} = f & \text{for } x,t \in Q \\ u = u_0 & \text{for } x \in \Omega,\ t = t^0 \end{cases} \tag{4.1}$$

Where u_0 is the initial condition, Q is the space-time domain and Ω is the 1-dimensional spatially periodic domain. The initial condition will be propagated in time from $t = t^0$ to $t = T$.

The 'inviscid' Burgers equation constitutes a conservation law, as shown in Eq. (4.2). The associated flux $\frac{1}{2}u^2$ can be interpreted as the kinetic energy of the flow. Solutions of conservation equations can be constructed by means of the method of characteristics. In case of a Burgers equation the characteristics of the initial condition may cross due to the nonlinearity of the PDE. This leads to discontinuities. The Rankine-Hugoniot condition ensures that the (unique) viscosity solution is retrieved [60, 61].

$$
\begin{aligned}
& u_t + u\,u_x = u_t + \frac{1}{2}\left(u^2\right)_x = 0 \\
& \int_{x_j}^{x_{j+1}} u_t + \int_{x_j}^{x_{j+1}} \frac{1}{2}\left(u^2\right)_x = 0 \quad \Rightarrow \quad \frac{\mathrm{d}}{\mathrm{d}t} \int_{x_j}^{x_{j+1}} u = \frac{1}{2}u^2\Big|_{x_j} - \frac{1}{2}u^2\Big|_{x_{j+1}}
\end{aligned}
\tag{4.2}
$$

The viscous variant of the Burgers equation may be integrated explicitly by making use of the Cole-Hopf transformation [61–63]. This indicates that the solution is insensitive to small perturbations in the initial condition, and does not exhibit self-randomizing and intrinsically chaotic behavior [59]. These are key factors in Navier-Stokes turbulence. Despite the lack of these features, Burgers turbulence can still serve as a benchmark for turbulence models. In particular the energy in the solution field is dissipated following an energy cascade that is remarkably similar to the energy cascade observed in 3-dimensional Navier-Stokes turbulence [5, 59, 64]. On average the kinetic energy is transported to higher frequency modes by the nonlinear hyperbolic nature of the PDE. At the high frequency range of the energy spectrum the energy is dissipated by the viscous term.

The important role of the scale interaction makes the Burgers equation especially suitable as an indicator of the performance of new variational multiscale models. Additionally, the nonlinear hyperbolic nature of the PDE has the tendency to develop shocks in the solution field. These can be captured especially well by using a discontinuous discretization. Therefore, the Burgers equation is an excellent candidate for evaluating the proposed DG-RVMS framework.

4.1.1 Space-time finite element formulation

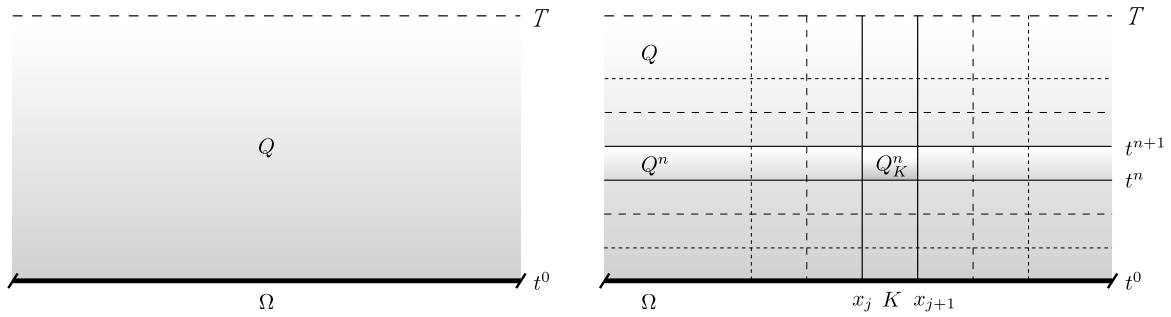

(a) Space-time domain of the Burgers equation.

(b) Discretization of the space-time domain.

Fig. 4.1: *Definition of the domain and subdomains.*

The weak formulation is recovered in a space-time finite element setting. This setting allows a split of basis functions into fine scale and coarse scale components for both the time dimension and the space dimension. Thereby, the variational multiscale method and the fine scale models can be derived consistently. The weak formulation is obtained through multiplication with a space-time test function and subsequent integration over the complete space-time

Table 4.1: *Collection of domain definitions.*

Space domain	Ω		$\subset \mathbb{R}$
Space-time domain	Q	$= \Omega \times [t^0, T]$	$\subset \mathbb{R} \times \mathbb{R}$
Time slab	Q^n	$= \Omega \times [t^n, t^{n+1}]$	$\subset \mathbb{R} \times \mathbb{R}$
Element space domain	K		$\subset \mathbb{R}$
Element time slab	Q_K^n	$= K \times [t^n, t^{n+1}]$	$\subset \mathbb{R} \times \mathbb{R}$
Numerical interior domain	Ω_E	$= \bigcup_{K \in \mathcal{T}} K$	
		$(p,q)_{\Omega_E} = \sum_{K \in \mathcal{T}} (p,q)_K$	
Interior facets (Excludes domain boundary)	Γ	$= \bigcup_{K \in \mathcal{T}} \partial K$	
		$= \{x_0, x_2, \cdots, x_j, \cdots, x_{N-1}\}$	
		$\langle [\![p]\!], 1 \rangle_\Gamma = \sum_{K \in \mathcal{T}} \langle p \cdot n, 1 \rangle_{\partial K}$	
		$\langle \{\!\{p\}\!\}, 1 \rangle_\Gamma = \sum_{K \in \mathcal{T}} \langle \frac{1}{2} p, 1 \rangle_{\partial K}$	

domain. The function space $\mathbb{Q}_Q$ corresponds to the space defined in Eq. (3.2), extended to span the space-time domain Q. For all domain definitions, refer to Figure 4.1 and Table 4.1.

$$\begin{aligned} &\text{Find } u \in \mathbb{Q}_Q \text{ s.t.:} \\ &(w, u_t)_Q + \frac{1}{2}(w, (u^2)_x)_Q - (w, \nu u_{xx})_Q = (w, f)_Q \qquad \forall\, w \in \mathbb{Q}_Q \end{aligned} \tag{4.3}$$

The time domain is treated as a stack of time-slabs. Weak formulation (4.3) can be defined for each of these slabs. These are solved sequentially, where the solution at time t^{n+1} of slab Q^n is the initial condition for slab Q^{n+1}. For its current purpose these initial conditions will be incorporated into the function space, rather than via integration by parts in the time domain.

$$(w, u_t)_{Q^n} + \frac{1}{2}(w, (u^2)_x)_{Q^n} - (w, \nu u_{xx})_{Q^n} = (w, f)_{Q^n} \qquad \forall\, w \in \mathbb{Q}_{Q^n} \tag{4.4}$$

The next step to obtain a VMS formulation would be to introduce the split of basis functions. These formulations be will developed for different cases in Sections 4.2 to 4.4. The fine scale model will be based on the VMS formulation. However, the coarse scale formulation is solved using a finite difference time stepping method. This finite difference time stepping algorithm requires a spatial finite element formulation to obtain the time derivatives. For any time t the

PDE may be multiplied with a test function purely in space. Subsequent integration by parts yields the following formulation. No surface terms are introduced since the spatial domain is periodic.

$$(w, u_t)_\Omega - \frac{1}{2}(w_x, u^2)_\Omega + (w_x, \nu u_x)_\Omega = (w, f)_\Omega \qquad \forall\, w \in \mathbb{Q} \tag{4.5}$$

4.1.2 Runge-Kutta time integration

The Runge-Kutta (RK) method is a finite difference type time integration method. It is the typical time integration method for computational fluid dynamics [13]. Often an implicit, or mixed implicit-explicit form is adopted. The current work will use a purely explicit scheme as this will simplify the implementation of the residual-based fine scale model later on.

The explicit Runge-Kutta time integration algorithm is:

1. The initial condition for time-slab Q^n is the final solution of the computation corresponding to time-slab Q^{n-1}. This solution is denoted $u^{(t^n)}$.
2. Based on this solution the time derivative u_t at time t^n is obtained as the finite element solution to Eq. (4.5). This is treated explicitly, meaning that all-but-the-first term are contributions to the force vector. The obtained time derivative is denoted $u_t^{(t^n)}$.
3. The obtained u_t and $u^{(t^n)}$ are used to find an intermediate u, at time $t^n + \alpha_1 \Delta t$. A basic forward Euler scheme is used. This solution is denoted $u^{(t^n+\alpha_1\Delta t)}$.
4. An intermediate u_t is obtained from finite element formulation (4.5) while using the solution $u^{(t^n+\alpha_1\Delta t)}$. The new time derivative is denoted $u_t^{(t^n+\alpha_1\Delta t)}$.
5. An new intermediate u at time $t^n + \alpha_2 \Delta t$ is again obtained from a forward Euler scheme. The initial condition $u^{(t^n)}$ is used as the start point in the forward Euler scheme. The time derivative used in the forward Euler method is a weighted average of the previously found time derivatives. The weighting factors are $\beta_{1,1}$ and $\beta_{1,2}$
6. The last two steps are repeated until the final solution $u^{(t^n+\Delta t)} = u^{(t^{n+1})}$ is found. Different β coefficients are used for each new Euler scheme.

The explicit time stepping approach makes it possible to invert the finite element formulations of Eq. (4.5) in its matrix form according to Eq. (4.6). In this equation the mass matrix $\mathbf{M}$ is obtained from the assembly of the first term in Eq. (4.5). The mass matrix does not change throughout the computation and therefore has to be assembled and inverted only once.

$$\mathbf{u}_t = \mathbf{M}^{-1}\mathbf{f}(\mathbf{u}) \tag{4.6}$$

The previously described iterative solution procedure can be summarized by the following set of intermediate solutions. These solutions make use of the inverted finite element matrix equation.

1. $\mathbf{u}^{(t^n)}$
2. $\mathbf{u}_t^{(t^n)} = \mathbf{M}^{-1}\mathbf{f}(\mathbf{u}^{(t^n)})$
3. $\mathbf{u}^{(t^n+\alpha_1\Delta t)} = \mathbf{u}^{(t^n)} + \alpha_1\Delta t\, \mathbf{u}_t^{(t^n)}$
4. $\mathbf{u}_t^{(t^n+\alpha_1\Delta t)} = \mathbf{M}^{-1}\mathbf{f}(\mathbf{u}^{(t^n+\alpha_1\Delta t)})$
5. $\mathbf{u}^{(t^n+\alpha_2\Delta t)} = \mathbf{u}^{(t^n)} + \alpha_2\Delta t\,(\,\beta_{1,1}\mathbf{u}_t^{(t^n)} + \beta_{1,2}\mathbf{u}_t^{(t^n+\alpha_1\Delta t)}\,)$
6. $\mathbf{u}_t^{(t^n+\alpha_2\Delta t)} = \mathbf{M}^{-1}\mathbf{f}(\mathbf{u}^{(t^n+\alpha_2\Delta t)})$
7. $\mathbf{u}^{(t^n+\alpha_3\Delta t)} = \mathbf{u}^{(t^n)} + \alpha_3\Delta t\,(\,\beta_{2,1}\mathbf{u}_t^{(t^n)} + \beta_{2,2}\mathbf{u}_t^{(t^n+\alpha_1\Delta t)} + \beta_{2,2}\mathbf{u}_t^{(t^n+\alpha_2\Delta t)}\,)$
8. $\cdots$

Different explicit Runge-Kutta methods are obtained for different sets of α's and β's. In this chapter the RK4 scheme and the Dormand-Prince Runge-Kutta scheme will be used. The RK4 scheme is fourth order accurate in the accumulated (global) error, and fifth order accurate in the local truncation error. The Dormand-Prince scheme is fifth order accurate in the accumulated error, and sixth order accurate in the local truncation error [65]. Their sets of parameters are given in Tables 4.2 and 4.3 respectively.

0				
α_1	$\beta_{1,1}$			
α_2	$\beta_{2,1}$	$\beta_{2,2}$		
α_3	$\beta_{3,1}$	$\beta_{3,2}$	$\beta_{3,3}$	
1	$\beta_{4,1}$	$\beta_{4,2}$	$\beta_{4,3}$	$\beta_{4,4}$

0				
$\frac{1}{2}$	$\frac{1}{2}$			
$\frac{1}{2}$	0	$\frac{1}{2}$		
1	0	0	1	
1	$\frac{1}{6}$	$\frac{1}{3}$	$\frac{1}{3}$	$\frac{1}{6}$

Table 4.2: *RK4 tableau.*

0						
$\frac{1}{5}$	$\frac{1}{5}$					
$\frac{3}{10}$	$\frac{3}{40}$	$\frac{9}{40}$				
$\frac{4}{5}$	$\frac{44}{45}$	$-\frac{56}{15}$	$\frac{32}{9}$			
$\frac{8}{9}$	$\frac{19372}{6561}$	$-\frac{25360}{2187}$	$\frac{64448}{6561}$	$-\frac{212}{729}$		
1	$\frac{9017}{3168}$	$-\frac{355}{33}$	$\frac{46732}{5247}$	$\frac{49}{176}$	$-\frac{5103}{18656}$	
1	$\frac{35}{384}$	0	$\frac{500}{1113}$	$\frac{125}{192}$	$-\frac{2187}{6784}$	$\frac{11}{84}$
1	$\frac{5179}{57600}$	0	$\frac{7571}{16695}$	$\frac{393}{640}$	$-\frac{92097}{339200}$	$\frac{187}{2100}$	$\frac{1}{40}$

Table 4.3: *Dormand-Prince Runge-Kutta tableau.*

In order to evaluate the resulting solutions obtained with the different models in Sections 4.2 to 4.4, a benchmark solution is required. A benchmark problem is formulated in the following, and the corresponding solution is analyzed.

4.1.3 Direct numerical simulation benchmark results

The significance of the scale interaction present in Burgers turbulence, and Navier-Stokes turbulence, is the main reason for the effectiveness of the variational multiscale method. An alternative approach to capture this scale interaction is to simply compute all the scales of importance. This is referred to as direct numerical simulation (DNS). Clearly this comes with great computational cost. Therefore, these computations are mostly carried out on

small domains as reference solutions [66–68]. Different turbulence modeling techniques can be verified based on these benchmarks. For Navier-Stokes turbulence the smallest scales of importance are called the Kolmogorov scales [69, 70]. At these length and time scales the effective Reynolds number has decreased so far that viscous effects dominate the governing equations. An analogous length scale does not exist for Burgers turbulence [59]. The construction of a DNS solution thereof will hinge on sufficient refinement of the computational mesh. Specifically, the shock wave that will occur in the following problem needs to be well resolved. Since a 1D domain is considered, a relatively fine mesh can be used without the need of excessive computational resources.

The DNS benchmark will concern a problem formulation described in [71]. This paper dealt with an eddy viscosity model within a three-scale VMS framework. It will serve as the basis for all numerical experiments that are performed in this chapter. Thereby, a consistent overview of the potential improvements can be provided. The problem deals with a periodic forcing on a periodic domain. Details are provided in Figure 4.2. The problem was solved by using 8192 elements of polynomial degree 1. This yields a solution that is sufficiently accurate for its current purposes to be referred to as a DNS solution [71]. The Dormand-Prince Runge-Kutta scheme is used for time stepping. This scheme was chosen as it could be used with larger time steps than the classical RK4 scheme. Still a relatively fine time step of $\Delta t = h/24$ was required to ensure stability, where h is the element width. The time steps need to be this small because of the explicit nature of the time stepping algorithm, and the nonlinear hyperbolic nature of the PDE. In comparison a 12 times larger time step can be used if space-time finite elements are be employed [71]. Since all future numerical experiments will make use of Runge-Kutta time stepping, it was felt that this should be reflected in the DNS computation. The obtained solution at $t = 8\pi$ is shown in Figure 4.2.

Burgers problem
$\Omega = [0\,,\, 2\pi]$, periodic
$t^0 = 0$, $T = 8\pi$
$f(x,t) = 0.1\,\sin(x - t)$
$\nu = 2\pi/1000$
$u(x,0) = 1$

Numerical discretization
8192 linear elements
RK-scheme: Table 4.3
$\Delta t = h/24 = 2\pi/8192/24$

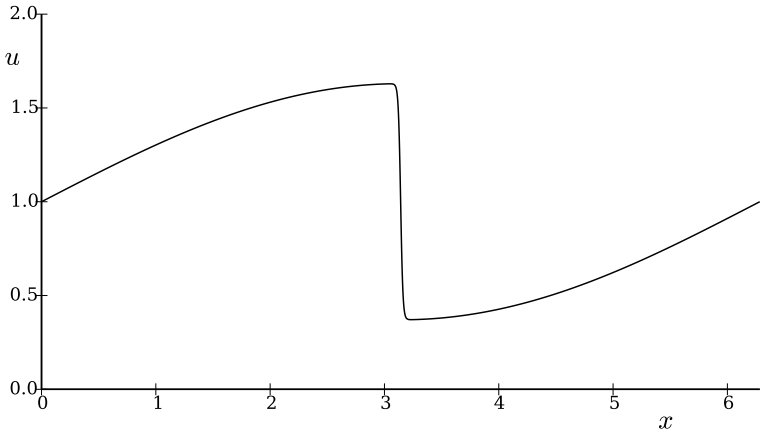

Fig. 4.2: *DNS solution of the Burgers problem at time* $t = 8\pi$.

The scale interaction that occurs within the solution of Figure 4.2 can be interpreted as an energy transfer. To examine this behavior the energy spectrum of the solution can be visualized. This spectrum is obtained by means of a fast Fourier transform (FFT) of the nodal solution data. The spectral energy is obtained from the FFT coefficients by means of Eq. (4.8). This definition of the spectral energy suits Eq. (4.7), such that the total energy is given by the sum of the spectral energies. Equation (4.7) uses Parseval's identity to go from

a sum of squared values in the spatial domain, to the sum of squared values in the frequency domain. The resulting energy spectrum of the DNS solution is shown in Figure 4.3.

$$E_{tot}\big|_t \equiv \frac{1}{2}\int_0^{2\pi} u(x,t)^2\,\mathrm{d}x \;\approx\; \frac{\pi}{N}\sum_{\hat{x}=0}^{N-1} u(\frac{2\pi}{N^2}\hat{x},t)^2 \;=\; \frac{\pi}{N^2}\sum_{n=-\lfloor N/2\rfloor}^{\lfloor N/2\rfloor} |\mathrm{FFT}(n)|^2 = \sum_{k=0}^{\lfloor N/2\rfloor} E(k)$$
$$\approx 3.75744936272 \tag{4.7}$$

$$E(k) = \begin{cases} \dfrac{\pi}{N^2}\,|\mathrm{FFT}(k)|^2 & \text{When } k = 0 \\ \dfrac{2\pi}{N^2}\,|\mathrm{FFT}(k)|^2 & \text{When } k > 0 \end{cases} \tag{4.8}$$

The noisy behavior past $k = 10^3$ is the result of computational accuracy; $E(k) \approx 10^{-32}$ corresponds roughly to the square of the floating point precision of a `double` number format. Remarkable is the smoothness of the solution at the lower range of the spectrum. The seemingly steep near-discontinuity shown in Figure 4.2 does not translate to notable behavior is in the high frequency range. The figure is consistent with the expected Burgers turbulence behavior. Energy from the periodic forcing enters as a low frequency response. The nonlinear hyperbolic nature of the equation results in a solution that ramps up. In the frequency response this corresponds to energy traversing to the high frequency scales. At the higher frequency ranges, associated with high second derivatives, the energy is dissipated by the viscous term in the equation.

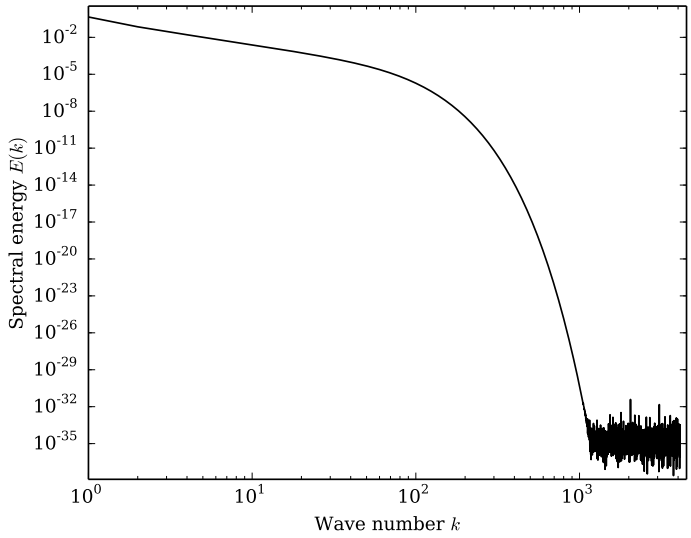

Fig. 4.3: *Energy spectrum of the Burgers solution at time $t = 8\pi$.*

The goal of the VMS method is to capture the scale interaction that was described earlier. Since these revolve around the behavior of the energy in the system, the analysis of the numerical experiments will also focus on the energy in the solution. Three different types of VMS methods will be investigated in the remaining of this chapter. For each of the

implementations the performance will be assessed in three stages. First, the solution at $t = 8\pi$ is visually inspected. Secondly, the total energy in the final solution is investigated, as well as the convergence thereof with respect to the number of degrees of freedom. Finally, the energy spectrum of the numerical solution is examined. The analyses will considered basis functions of a range of polynomial degrees. Each of these facets is compared to the DNS solution.

4.2 A three-scale approach using an eddy viscosity model

The first modeling approach is based on early work on the variational multiscale framework, before the residual-based modeling concept was introduced. Eddy viscosity models, known from RANS and LES type turbulence models, were adapted to the VMS framework [23–25]. A formal way of deriving the finite element formulation is through the introduction of a three-scale system of equations [39]. The energy in the solution field is transferred from the coarse scale through the intermediate scale range to the fine scales. The eddy viscosity three-scale VMS model enforces this flow of energy explicitly. In the residual-based fine scale models developed in Sections 4.3 and 4.4 this energy cascade occurs more implicitly. As such, the current section will offer a measure by which future R-VMS models can be evaluated.

4.2.1 Model formulation

The test and trial functions from the spatial weak formulation of Eq. (4.5) are split into three components associated to three different function spaces. Each function space signifies a new range of scales, going from the coarse scales $\bar{\mathscr{M}}$ to the intermediate scales $\tilde{\mathscr{M}}$ and the fine scales $\mathscr{M}'$.

$$\begin{aligned}
\bar{\mathscr{M}} &= \{v \in \mathscr{C}^0(\Omega) : v\big|_K \in P^m(K) \;\; \forall\, K \in \mathscr{T}\} \\
\tilde{\mathscr{M}} &= \{v \in \mathscr{C}^0(\Omega) : v\big|_K \in P^p(K) \setminus \bar{\mathscr{M}} \;\; \forall\, K \in \mathscr{T}\} \\
\mathscr{M}' &= \{v \in \mathscr{C}^0(\Omega) : v\big|_K \in P^\infty(K) \setminus \bar{\mathscr{M}} \oplus \tilde{\mathscr{M}} \;\; \forall\, K \in \mathscr{T}\}
\end{aligned} \tag{4.9}$$

Each of these spaces is a $\mathscr{C}^0$ continuous finite element space. As such, this decomposition is slightly different from the decomposition into $\bar{\mathbb{Q}}$ and $\mathbb{Q}'$. Recall that $\bar{\mathbb{Q}}$ was a function space of higher order continuous functions (defined in Eq. (3.2)). In order to split the weak form into its three components these function spaces must be a direct sum decomposition of $\mathbb{Q}$, so $\mathbb{Q} = \bar{\mathscr{M}} \oplus \tilde{\mathscr{M}} \oplus \mathscr{M}'$. Then the three-scale interpretation of the Burgers equation reads:

Find $\bar{u}\,, \tilde{u}, u' \in \bar{\mathscr{M}} \times \tilde{\mathscr{M}} \times \mathscr{M}'$ s.t.:

$$\begin{cases}
\big(\bar{w}\,, \bar{u}_t + \tilde{u}_t + u'_t\big)_\Omega - \frac{1}{2}\big(\bar{w}_x\,, (\bar{u}+\tilde{u}+u')^2\big)_\Omega + \big(\bar{w}_x\,, \nu(\bar{u}_x + \tilde{u}_x + u'_x)\big)_\Omega = \big(\bar{w}\,, f\big)_\Omega & \forall\, \bar{w} \in \bar{\mathscr{M}} \\
\big(\tilde{w}\,, \bar{u}_t + \tilde{u}_t + u'_t\big)_\Omega - \frac{1}{2}\big(\tilde{w}_x\,, (\bar{u}+\tilde{u}+u')^2\big)_\Omega + \big(\tilde{w}_x\,, \nu(\bar{u}_x + \tilde{u}_x + u'_x)\big)_\Omega = \big(\tilde{w}\,, f\big)_\Omega & \forall\, \tilde{w} \in \tilde{\mathscr{M}} \\
\big(w', \bar{u}_t + \tilde{u}_t + u'_t\big)_\Omega - \frac{1}{2}\big(w'_x, (\bar{u}+\tilde{u}+u')^2\big)_\Omega + \big(w'_x, \nu(\bar{u}_x + \tilde{u}_x + u'_x)\big)_\Omega = \big(w', f\big)_\Omega & \forall\, w' \in \mathscr{M}'
\end{cases} \tag{4.10}$$

The objective of the three-scale approach is to compute the two coarse scale components $\bar{u}$

and $\tilde{u}$, while incorporating the effect of the infinite dimensional fine scale solution u'. To this end, Eq. (4.10) has to be simplified to yield a closed set of equations for $\bar{u}$ and $\tilde{u}$.

The energy cascade observed in turbulent flow indicates that interaction between the different scales occurs in a hierarchical manner. Flow structures within a certain spectral range interact predominantly with flow structures of neighboring length scales. As such, a physically inspired simplification is to ignore the influence of the fine scale flow u' onto the coarse scale solution $\bar{u}$. Secondly, the physical nature of turbulence demonstrates a predominantly dissipative role of the fine scales. Based on this behavior the effect of the fine scale onto the intermediate scale $\tilde{u}$ is modeled as an energy sink. To this end, the diffusion coefficient ν is increased by a so-called eddy viscosity ν_T. The simplified three-scale set of equations becomes:

Find $\bar{u}\,, \tilde{u} \in \bar{\mathscr{M}} \times \tilde{\mathscr{M}}$ s.t.:

$$\begin{cases} \left(\bar{w}, \bar{u}_t + \tilde{u}_t\right)_\Omega = \frac{1}{2}\left(\bar{w}_x, (\bar{u}+\tilde{u})^2\right)_\Omega - \left(\bar{w}_x, \nu(\bar{u}_x + \tilde{u}_x)\right)_\Omega + \left(\bar{w}, f\right)_\Omega & \forall\, \bar{w} \in \bar{\mathscr{M}} \\ \left(\tilde{w}, \bar{u}_t + \tilde{u}_t\right)_\Omega = \frac{1}{2}\left(\tilde{w}_x, (\bar{u}+\tilde{u})^2\right)_\Omega - \left(\tilde{w}_x, \nu\, \bar{u}_x\right)_\Omega - \left(\tilde{w}_x, (\nu+\nu_T)\, \tilde{u}_x\right)_\Omega + \left(\tilde{w}, f\right)_\Omega & \forall\, \tilde{w} \in \tilde{\mathscr{M}} \end{cases} \tag{4.11}$$

This finite element problem requires a hierarchical set of basis functions in order to satisfy $\bar{\mathscr{M}} \cap \tilde{\mathscr{M}} = \{0\}$. Recall that this is a condition for the direct sum-decomposition. Spectral methods suit this purpose, and so do Legendre basis functions. The latter will be used in correspondence with [71]. Low order Legendre basis functions are used to construct $\bar{\mathscr{M}}$. Subsequent higher order basis functions are used for the construction of $\tilde{\mathscr{M}}$. In the following the highest polynomial degree included in $\bar{\mathscr{M}}$ is denoted m and the highest polynomial degree in $\tilde{\mathscr{M}}$ is denoted p.

4.2.2 The eddy viscosity parameter

In order to numerically solve Eq. (4.11), the eddy viscosity parameter ν_T needs to be estimated. Recall that this is the viscosity contribution that simulates the dissipative interaction of the fine scales u' onto the intermediate scales $\tilde{u}$. An appropriate value of this parameter can be estimated by making use of the DNS energy spectrum that was obtained earlier. In general the rate of dissipation of the spectral mode with frequency k is given by [61]:

$$\frac{\mathrm{d}}{\mathrm{d}t} E(k) = -2\nu k^2 E(k) \tag{4.12}$$

The scale interaction simulated by the VMS method must ensure that the total dissipated energy in the intermediate scale weak formulation also includes the energy dissipated in the fine scale solution. As such:

$$(\nu_T + \nu) \sum_{k_m}^{k_p} k^2 E(k) = \nu \sum_{k_m}^{\infty} k^2 E(k) \quad \Rightarrow \quad \nu_T = \nu \left(\frac{\sum_{k_p}^{\infty} k^2 E(k)}{\sum_{k_m}^{k_p} k^2 E(k)} \right) \tag{4.13}$$

Where k_p is the cut-off wave number associated to all the modes that can be approximated by the space $\bar{\mathcal{M}} \oplus \tilde{\mathcal{M}}$, and k_m is the cut-off wave number for the space $\bar{\mathcal{M}}$. Since these spaces do not directly correspond to a set of trigonometric functions, the associated wave number needs to be approximated. According to the Nyquist theorem the highest frequency that can be reconstructed consistently from a set of equispaced data points is half the sampling rate. Inspired by this theorem the cut-off frequencies of Eq. (4.14) are proposed. In this equation dofs stands for degrees of freedom.

$$\begin{aligned} k_p &= \frac{1}{2}\,\text{dofs} = \frac{1}{2}\,p\,N \\ k_m &= \frac{1}{2}\,m\,N \end{aligned} \tag{4.14}$$

Here N is the number of elements, p is the maximum polynomial order of the Legendre basis functions that are being used, and m the order past which the model is introduced. If $m = 0$ then the modeling would be introduced to all scales. This corresponds to a typical large-eddy simulation model. Both a true VMS ($m > 0$) and an LES ($m = 0$) model will be considered in the following. Thereby, the effect of the three-scale nature of the VMS implementation can be evaluated.

Table 4.4 provides an overview of the ν_T/ν fractions that were obtained from Eq. (4.13). All the VMS numerical experiments will make use of a cut-off polynomial degree m that satisfies $m = \frac{1}{2}\,p$. When this is substituted into Eqs. (4.13) and (4.14) it follows that the values for ν_T/ν only depend on the number of degrees of freedom. Similarly all LES computations per definition make use of an m that equals 0. Hence the fraction ν_T/ν also only depends on the number of degrees of freedom.

Table 4.4: *Fractions ν_T/ν for different numbers of degrees of freedom, used for the numerical experiments in Figs. 4.5 to 4.7.*

Degrees of freedom (dofs)	16	32	64	128	256
ν_T/ν for the VMS model	11.2	4.86	1.80	0.480	0.0598
ν_T/ν for the LES model	5.62	2.38	0.826	0.172	0.00834

The numerical results that are obtained by making use of the model discussed in Section 4.2.1, and the parameters from Table 4.4, will be discussed in the following section.

4.2.3 Numerical results

The numerical implementation makes use of the RK4 time stepping scheme of Table 4.2. A time step of $\Delta t = \pi/384$ is used for all computations. When the eddy viscosity VMS model is used with 16 elements and a $m = 1$, $p = 2$ discretization, then the solution of Figure 4.4 is obtained.

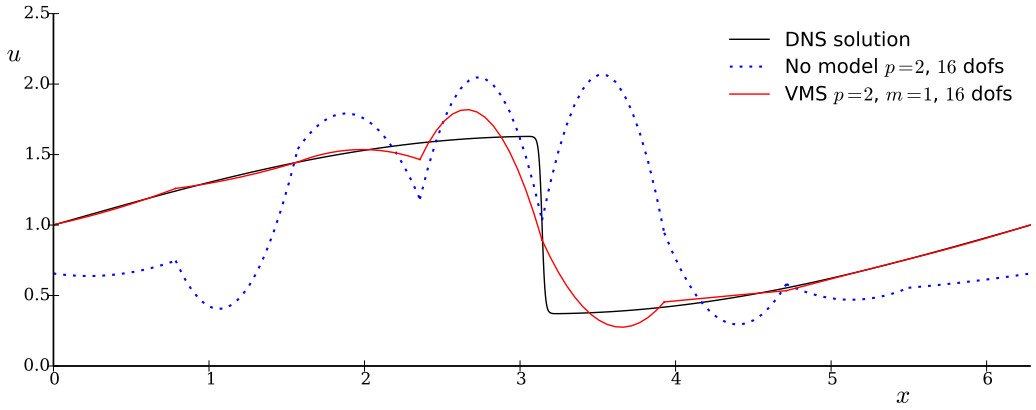

Fig. 4.4: *Example solution, with and without proposed eddy viscosity model with* $\nu_T/\nu = 4.86$. *Using a total of 16 elements with quadratic basis functions.*

The significant increase in accuracy is apparent. The near-discontinuity of the exact solution results in large oscillatory behavior after the wave front when the VMS model is omitted. The solution that does include the VMS model does not exhibit this behavior. Instead a nearly symmetrical solution is obtained. Despite the continuity of the solution basis the shock is almost completely contained within the two neighboring elements.

The increase in accuracy of the solution field translates to an increase in accuracy of the energy contained in the solution. This is shown in the convergence curves for different pairs of p and m. The total energy of these solution is computed at time $t = 8\pi$. This is compared to the average energy of the DNS solution at $6\pi \leq t \leq 8\pi$. Thereby a relative error in total energy is obtained. Figures 4.5 to 4.7 show convergence curves for three different VMS computations. These are compared to corresponding solutions that do not include any modeling, i.e. $\nu_T = 0$. Additionally, an equivalent LES computation is provided for reference. Recall that the LES computation introduces the eddy viscosity to all scales, which means that $m = 0$.

The VMS model outperforms the LES model at practically every instance. This indicates that the effect of the correct scale interaction imposed by the VMS model works. Compared to the no-model solution it is clear that the most significant improvement is obtained for coarse discretizations. This is to be expected; as the mesh becomes finer, the DNS solution is approached. At some stage the mesh is fine enough to capture sufficient scale interaction without the VMS model.

Interestingly the VMS method is not as effective at the highest polynomial order, shown in Figure 4.7. This may be due to an inaccurate estimation of ν_T. The estimation for the eddy viscosity parameter was based on the estimated cut-off frequencies of Eq. (4.14). Yet these were purely based on the number of degrees of freedom associated with the set of basis functions. In reality the higher order basis functions are richer than a set of data points, as implied by this estimation.

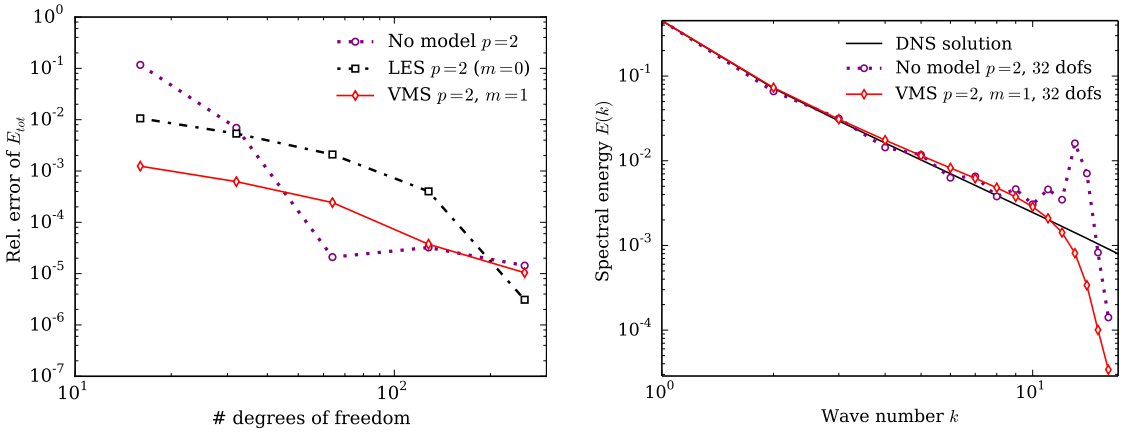

(a) Relative error in total energy at $t = 8\pi$.

(b) Spectral energy of the first 17 wave numbers. Average in $6\pi \leq t \leq 8\pi$.

Fig. 4.5: *Obtained energy convergence and spectrum for $p = 2$ and $m = 1$ polynomial basis functions. Including and excluding the eddy viscosity model.*

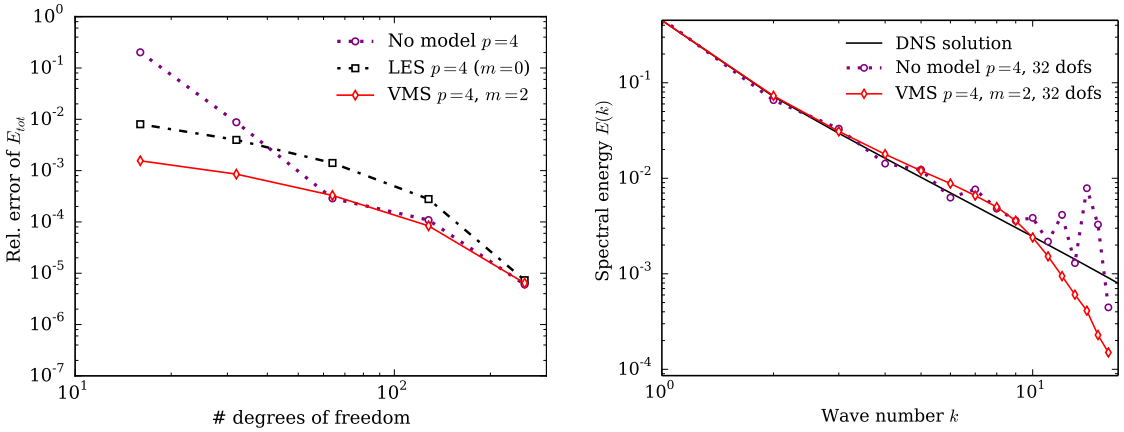

(a) Relative error in total energy at $t = 8\pi$.

(b) Spectral energy of the first 17 wave numbers. Average in $6\pi \leq t \leq 8\pi$.

Fig. 4.6: *Obtained energy convergence and spectrum for $p = 4$ and $m = 2$ polynomial basis functions. Including and excluding the eddy viscosity model.*

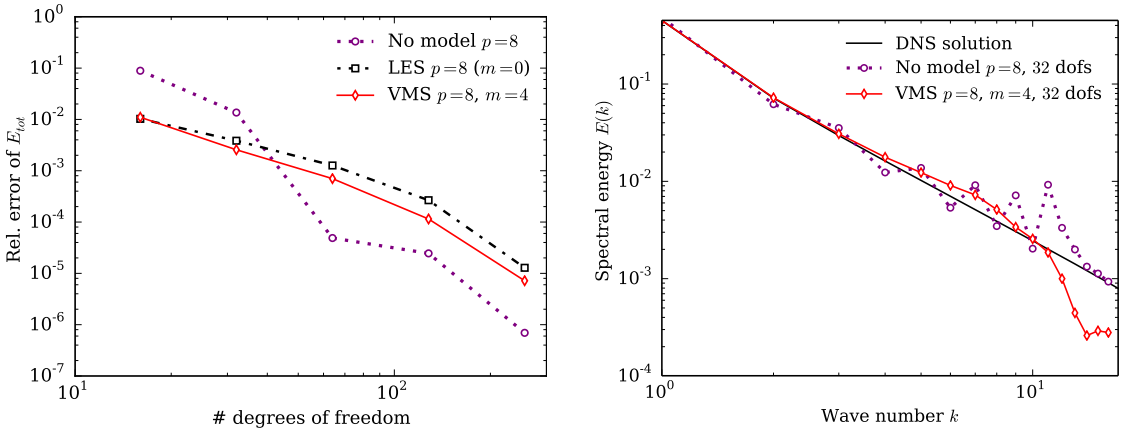

(a) Relative error in total energy at $t = 8\pi$

(b) Spectral energy of the first 17 wave numbers. Average in $6\pi \leq t \leq 8\pi$.

Fig. 4.7: *Obtained energy convergence and spectrum for $p = 8$ and $m = 4$ polynomial basis functions. Including and excluding the eddy viscosity model.*

Finally, an energy spectrum is shown for each of the pairs of p and m. All spectrum figures concern a discretization with 32 degrees of freedom. The spectra are obtained according to a similar approach as described in Section 4.1.3. The solution is first sampled at a higher sampling rate to obtain the data points for the fast Fourier transform. This ensures that the polynomial order of the basis functions is properly captured in the energy spectrum. Additionally they are time averaged. These figures only show the first few frequencies, up to a number that is slightly larger than the Nyquist frequency. Partly because the low frequency modes are of prime interest, and partly because the high frequency modes show artificial patterns originated from the piece-wise polynomial origin of the solution. The DNS spectrum of Figure 4.3 is added to these figures.

Despite being time averaged, the spectra of the solution without VMS model show strongly erratic behavior. In contrast the spectra of the VMS solutions are very smooth. Generally the irregular spectra of the no-model solutions overshoot the DNS spectrum. This corresponds to the problem that the VMS method aims to solve: the dissipative nature of the fine scale solution is lost in the no-model finite element formulation. This leads to an energy build-up in the low frequency modes. The spectra of the solutions that did include the three-scale based VMS model approached zero much earlier. This indicates that energy at the intermediate scale range was indeed dissipated more heavily, as was the intent.

4.3 A classical residual-based model

A critical point in the eddy viscosity three-scale model is the estimation of the eddy viscosity parameter. In the previous section this parameter was estimated based on the DNS solution. Clearly this is generally not feasible. The R-VMS method does not require such physically

inspired parameters. This model is predominantly mathematical in origin and the involved parameters may be estimated independent of the DNS solution. The residual-based fine scale model developed in this chapter will be part of the model used for the DG-RVMS implementation of Section 4.4. It will therefore be described in more detail.

4.3.1 Model formulation

Th finite element formulation is obtained by introducing a two-scale split of basis functions in Eq. (4.5). Integration by parts is performed on the coarse scale equation such that no differential operator acts on the fine scale solution.

Find $\bar{u}, u' \in \bar{\mathbb{Q}} \times \mathbb{Q}'$ s.t.:

$$\begin{cases} (\bar{w}\,, \bar{u}_t + u'_t)_\Omega - \frac{1}{2}(\bar{w}_x, \bar{u}^2 + 2\bar{u}\,u')_\Omega + (\bar{w}_x, \nu\bar{u}_x)_\Omega = \\ \qquad\qquad\qquad\qquad \frac{1}{2}(\bar{w}_x, u'^{\,2})_\Omega \quad + (\bar{w}_{xx}, \nu u')_\Omega + (\bar{w}\,, f)_\Omega \qquad \forall\, \bar{w} \in \bar{\mathbb{Q}} \\ (w'\,, \bar{u}_t + u'_t)_\Omega + \frac{1}{2}(w', ((\bar{u} + u')^2)_x)_\Omega - (w', \nu(\bar{u}_{xx} + u'_{xx}))_\Omega = (w', f)_\Omega \qquad \forall\, w' \in \mathbb{Q}' \end{cases} \tag{4.15}$$

Where $\mathbb{Q} = \bar{\mathbb{Q}} \oplus \mathbb{Q}'$. Since the coarse scale equation includes second derivatives, i.e. $\bar{w}_{xx}$, the finite element space must be $\mathscr{C}^1$ continuous in space. For this reason B-spline basis functions will be used in the numerical experiments. These basis functions will be discussed in more detail later.

Finite difference time stepping will be used to advance the coarse scale solution in time. However, the fine scale model is obtained from a different, space-time, weak formulation. To obtain this model the split of basis functions is introduced in the space-time formulation (4.4):

Find $\bar{u}, u' \in \bar{\mathbb{Q}}_{Q^n} \times \mathbb{Q}'_{Q^n}$ s.t.:

$$\begin{cases} (\bar{w}\,,\, \bar{u}_t + u'_t)_{Q^n} + \frac{1}{2}(\bar{w}\,, ((\bar{u}+u')^2)_x)_{Q^n} - (\bar{w}\,, \nu(\bar{u}_{xx} + u'_{xx}))_{Q^n} = (\bar{w}\,,\, f)_{Q^n} \qquad \forall\, \bar{w} \in \bar{\mathbb{Q}}_{Q^n} \\ (w', \bar{u}_t + u'_t)_{Q^n} + \frac{1}{2}(w', ((\bar{u}+u')^2)_x)_{Q^n} - (w', \nu(\bar{u}_{xx} + u'_{xx}))_{Q^n} = (w', f)_{Q^n} \qquad \forall\, w' \in \mathbb{Q}'_{Q^n} \end{cases} \tag{4.16}$$

The residual-based fine scale model is analytically inspired by the fine scale weak formulation. It will involve average quantities of the Green's function that corresponds to the strong form of the fine scale problem. This is extensively discussed in Chapter 2, Section 3.3, and Appendix A. Since the numerical implementation will run through the time domain step by step, the Green's function will be defined on the space-time domain of a single time-slab Q^n. In order to obtain the Green's function associated to the per-time-slab fine scale problem, the fine scale equation in Eq. (4.16) is written in the following form.

$$\begin{aligned} (w', u'_t)_{Q^n} + \frac{1}{2}(w', (u'^2)_x)_{Q^n} + (w', u_h\, u'_x)_{Q^n} + (w', u_{hx}\, u')_{Q^n} - (w', \nu\, u'_{xx})_{Q^n} = \\ - (w', \bar{u}_t)_{Q^n} + (w', \nu\bar{u}_{xx})_{Q^n} - \frac{1}{2}(w', (\bar{u}^2)_x)_{Q^n} + (w', f)_{Q^n} = \\ (w', -\bar{u}_t - \frac{1}{2}(\bar{u}^2)_x + \nu\bar{u}_{xx} + f)_{Q^n} = (w', \mathscr{R}_{\bar{u}})_{Q^n} \end{aligned} \tag{4.17}$$

Where the right hand side can be recognized as the residual of the coarse scale solution $\bar{u}$ paired with the fine scale solution basis.

Two simplifications of the fine scale equation are often introduced. Since u' is considered small, the nonlinear term is neglected. Alternative derivations construct a perturbation series. The series has to be truncated at some term. For truncation after the first term, as proposed in [2], this is equivalent to neglecting square terms. Secondly, the domain is split up into the per-element space-time domains Q_K^n. The Green's function is defined for each individual Q_K^n. This is required to localize the resulting finite element formulation. In each Q_K^n the fine scale problem is an initial boundary value problem. This means that the solution u' involves space-time boundary conditions. It is assumed that these are homogeneous boundary conditions. This means that $u' = 0$ is used on the per-element space-time boundary ∂Q_K^n. This is a crude approximation but it is necessary in order to decouple the different elements.

Attempts have been made to reduce the severity of this approximation. Of particular interest is the work of Codina *et al.*. They propose a transient ODE for the fine scale volumetric model [72]. u' is remembered throughout the computation as a history variable. Thereby the dynamic nature of the subgrid scale model is retained. This model behaves particularly well for small time steps.

With the two previously mentioned assumptions, the fine scale problem is simplified to the following per-element space-time weak formulation. The model obtained by using these simplifications will no-longer yield the true coarse scale solution. Therefore, the approximate coarse scale solution u_h is introduced in place of $\bar{u}$ at this stage.

$$(w', u'_t)_{Q_K^n} + (w', u_h\, u'_x)_{Q_K^n} + (w', u_{hx}\, u')_{Q_K^n} - (w', \nu\, u'_{xx})_{Q_K^n} = (w', \mathcal{R}_{u_h})_{Q_K^n} \tag{4.18}$$

The corresponding strong form of this PDE takes the form of a transient advection-reaction-diffusion equation with homogeneous boundary conditions:

$$\begin{cases} u'_t + u_{hx}\, u' + u_h\, u'_x - \nu\, u'_{xx} = \mathcal{R}_{u_h} & x, t \in Q_K^n \\ u' = 0 & x, t \in \partial Q_K^n \end{cases} \tag{4.19}$$

For a homogeneous boundary value problem the exact solution can be retrieved from the Green's function.

$$u'(x) = \int_{Q_K^n} g'(x, y)\, f \,\mathrm{d}y = \int_{Q_K^n} g'(x, y)\, \mathcal{R}_{u_h} \,\mathrm{d}y \tag{4.20}$$

Based on this identity the fine scale model follows from the approximations

$$u'(x) \approx \int_{Q_K^n} g'(x, y) \,\mathrm{d}y\, \mathcal{R}_{u_h} \quad \Rightarrow \quad u' \approx \frac{1}{|Q_K^n|} \int_{Q_K^n} u' \approx \tau \mathcal{R}_{u_h} \tag{4.21}$$

Due to the transient (thus multidimensional) and nonlinear nature of the Burgers equation, and since higher order basis functions will be used, this substitution no longer yields an exact formulation for $\bar{u}$. Nevertheless the same average-like form of u' is used. The approximation has proven to be very effective [2, 20, 26, 28, 72, 73].

The complexity of Eq. (4.19) poses a challenge when attempting to acquiring the Green's

function. Instead the parameter τ associated to the PDE is constructed by means of asymptotic scaling arguments. The behavior of the PDE depends on the set of parameters ν, u_{hx} and u_h. Their values determine which differential operators will dominate the collective τ. The following asymptotic behavior is expected:

$$\begin{aligned}
\nu, u_{hx}, u_h \ll 1 \quad &\Rightarrow \quad \tau \to \tilde{\tau}_t \;\; = \tau_t \, C_1^{k-1} \\
u_{hx} \gg 1, \nu, u_h \quad &\Rightarrow \quad \tau \to \tilde{\tau}_R = \tau_R \, C_2^{p-1} \\
u_h \gg 1, u_{hx}, \nu \quad &\Rightarrow \quad \tau \to \tilde{\tau}_A = \tau_A \, C_2^{p-1} \\
\nu \gg 1, u_h, u_{hx} \quad &\Rightarrow \quad \tau \to \tilde{\tau}_D = \tau_D \, C_2^{p-1}
\end{aligned} \tag{4.22}$$

Where τ_t corresponds to the Green's function of a purely temporal differential operator $\frac{\mathrm{d}}{\mathrm{d}t}$. Similarly τ_R, τ_A and τ_D correspond to the reactive, advective and diffusive components of the PDE respectively. The τ expressions for each of these differential operators is devised in Appendix A. The following expressions were obtained. Refer to Eqs. (A.17), (A.21), (A.27) and (A.28) respectively.

$$\tau_t = \frac{\Delta t^2}{2h} \qquad \tau_R = \frac{1}{u_{hx}} \qquad \tau_A = \frac{h}{2u_h} \qquad \tau_D = \frac{h^2}{12\nu} \tag{4.23}$$

It is important to realize that these expressions are only valid for linear basis functions. This is argued in the derivation of these expressions in Appendix A. Higher order basis functions would leave more approximation freedom to describe the true solution within the element. This would reduce the magnitude of u' and hence the magnitude of τ. The multiplication by C_1^{k-1} and C_2^{p-1} in Eq. (4.22) is incorporated to capture this effect. p is the polynomial degree of the finite element discretization, and k the convergence rate of the finite difference time stepping algorithm. The exponentially decreasing order with respect to p and k is inspired by classical convergence rates observed in finite element error analysis. Additionally, the rates $p-1$ and $k-1$ ensures that $\tilde{\tau}_t = \tau_t$, $\tilde{\tau}_R = \tau_R$, $\tilde{\tau}_A = \tau_A$ and $\tilde{\tau}_D = \tau_D$ in the case of linear interpolations; $p = 1$ or $k = 1$. The coefficients C_1 and C_2 should be smaller than 1 to cause convergence towards zero. However, in practice it is found that a larger value often yields better results.

A typical way of constructing the global τ that behaves as described in Eq. (4.22) is shown in Eq. (4.24).

$$\begin{aligned}
\tau &= \frac{1}{\sqrt{\left(\frac{1}{\tilde{\tau}_t}\right)^2 + \left(\frac{1}{\tilde{\tau}_R}\right)^2 + \left(\frac{1}{\tilde{\tau}_A}\right)^2 + \left(\frac{1}{\tilde{\tau}_D}\right)^2}} \\
&= \frac{1}{\sqrt{\frac{4h^2}{\Delta t^4} C_1^{2-2k} + {u_h}_x^2 \, C_2^{2-2p} + \frac{4{u_h}^2}{h^2} C_2^{2-2p} + \frac{144\nu^2}{h^4} C_2^{2-2p}}}
\end{aligned} \tag{4.24}$$

This expression is very similar to those used in stabilized finite element methods. Indeed the structure of Eq. (4.24) is inspired by the expressions for the stabilization parameters in [33].

The fine scale model in Eq. (4.21), with the definition of τ from Eq. (4.24), is substituted in the coarse scale formulation of Eq. (4.15). The last simplification that needs to be made to obtain a fully closed form of the finite element formulation is to neglect u'_t. It is thereby assumed that within a time slab the fine scale time derivative has a negligible average effect.

$$\begin{aligned} &\text{Find } u_h \in \bar{\mathbb{Q}} \text{ s.t.:} \\ &(\bar{w}, u_{ht})_\Omega - \frac{1}{2}(\bar{w}_x, u_h^2)_\Omega - (\bar{w}_x, u_h \tau \mathscr{R}_{u_h})_\Omega + (\bar{w}_x, \nu u_{hx})_\Omega = \\ &\qquad (\bar{w}_x, f)_\Omega + (\bar{w}_{xx}, \nu\tau\mathscr{R}_{u_h})_\Omega + \frac{1}{2}(\bar{w}_x, (\tau\mathscr{R}_{u_h})^2)_\Omega \qquad \forall\, \bar{w} \in \bar{\mathbb{Q}} \end{aligned} \tag{4.25}$$

The just described residual-based model is treated explicitly in the RK4 time stepping scheme of Table 4.2. All fine scale terms become contributions to the force vector, and the coarse scale residual is computed based on previous solution values and time derivatives. To make this as consistent as possible with the original space-time formulation, this additional component of the force vector is recomputed at every α-step in the Runge-Kutta scheme. The computation of the force addition at each α-step will make use of the coarse scale solution and the coarse scale time derivatives from the previous α-step.

4.3.2 B-spline basis functions

Finite element formulation (4.25) requires second derivatives of the test function. For standard continuous Galerkin discretizations this would be a problem. While the first derivatives of Lagrange or Legendre basis functions are square-integrable on the domain Ω, their second derivatives are not. Differentiation of the jumps in the first derivatives give rise to Dirac layers at element interfaces. A different class of basis functions is implemented to mitigate this issue. These are so-called B-splines. The use of B-splines as basis functions to construct a finite element space is referred to as isogeometric analysis [46, 74]. Isogeometric analysis is the focus of much recent research. However, for its current purpose only the implementation of the B-spline basis functions is important.

Figure 4.8 shows three different orders of B-splines. Each separate spline is constructed by connecting a number of piecewise polynomial functions. These are connected such that they satisfy the required level of continuity. Second order B-splines consist of three $p = 2$ polynomials, connected such that they are $\mathscr{C}^1$ continuous. Third order splines are made up of four $p = 3$ polynomials such that they are $\mathscr{C}^2$ continuous. And so forth for higher order splines. With increasing order, also their domain of influence increases. Each point in the domain of Figure 4.8c is spanned by 5 fourth order splines. In contrast, only 3 second order splines cover each point in Figure 4.8a.

Each of the basis functions in Figure 4.8 lies in the $\mathscr{C}^1$ continuous space of functions. This is shown in Figure 4.9. The first derivatives shown in these figures are all continuous. As such, the B-splines are second order square-integrable. This makes them suitable basis functions for solving Eq. (4.25).

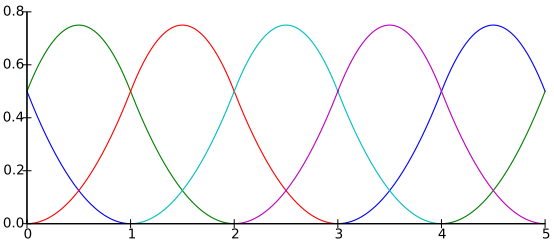

(a) 2nd order B-splines

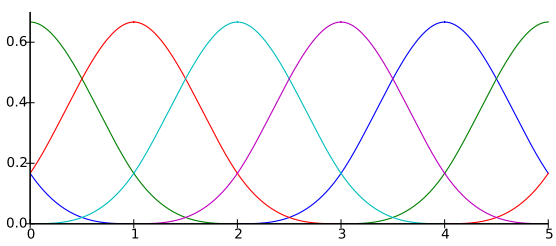

(b) 3rd order B-splines

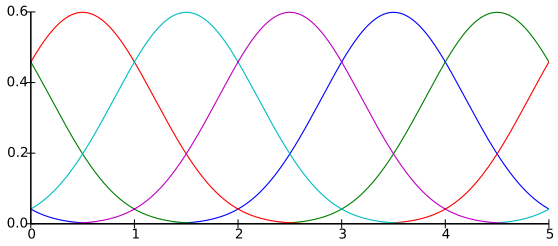

(c) 4th order B-splines

Fig. 4.8: *Five B-spline basis functions on a periodic [0, 5] domain, for multiple polynomial orders.*

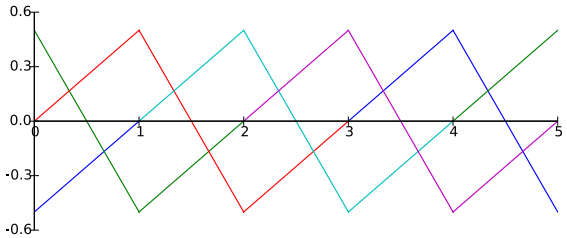

(a) 2nd order B-splines

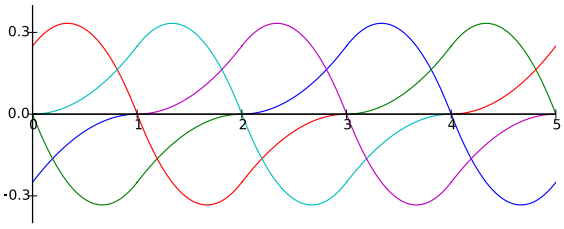

(b) 3rd order B-splines

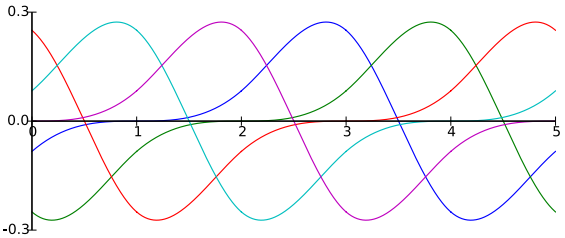

(c) 4th order B-splines

Fig. 4.9: *Derivatives of the B-spline basis functions of Figs. 4.8a to 4.8c.*

4.3.3 Numerical results

The implemented space finite element, time finite difference formulation makes use of the RK4 time stepping scheme of Table 4.2. A time step of $\Delta t = \pi/\text{dofs}/4$ is used. As stated in Section 4.1.2 the RK4 scheme is fifth order accurate in the local truncation error. Therefore $k = 5$ is used in the fine scale volumetric model. The R-VMS model depends on two coefficients. Table 4.5 provides an overview of the values that are used in the numerical experiments. It was attempted to keep them as constant as possible throughout the different computations, yet a larger C_1 is required for the coarse discretizations. This large factor does not yield convergence towards the no-model implementation in terms of total energy. Therefore, they are reduced for more refined computations.

Table 4.5: *Parameters used for the numerical experiments in Figs. 4.11 to 4.13.*

Dofs	4	8	16	32	64	128	256
C_1	2	2	2	2	0.7	0.7	0.7
C_2	0.7	0.7	0.7	0.7	0.7	0.7	0.7

When 32 second order splines are used with the just described R-VMS model, then Figure 4.10 is obtained. The figure shows very similar results compared to that obtained for the eddy viscosity model. When the R-VMS model is absent then the shock results in strong oscillatory behavior behind the wave front. This is fueled by the increase in continuity of the basis functions, which drives the unstable response far into the mesh. The solution stabilizes when the R-VMS model is implemented. The oscillatory behavior is quickly damped, and the true solution is approached a few elements past the shock wave. Compared to the eddy viscosity implementation the instability does travel through more elements in the B-spline implementation. However, this could reasonably be expected, given the extra level of continuity of the B-splines.

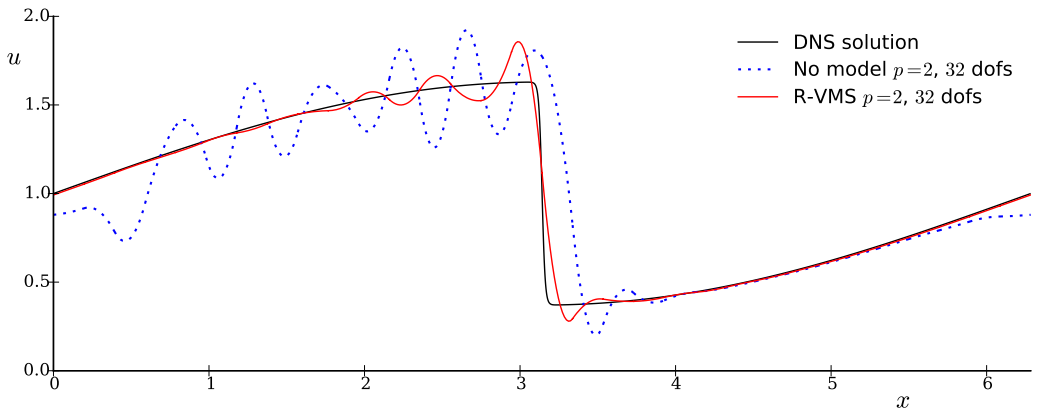

Fig. 4.10: *Example solution, with and without proposed R-VMS model with $C_1 = 2$ and $C_2 = 0.7$. Using a total of 32 2nd order B-splines.*

Figures 4.11a, 4.12a and 4.13a show convergence curves that focus on the total amount of energy in the solution at $t = 8\pi$. Again the relative errors are obtained by comparing to the average energy in the DNS solution at $6\pi \leq t \leq 8\pi$. Each figure concerns a different degree of the B-spline basis functions. All convergence curves show considerable increase in performance for low order discretizations. For finer meshes the no-model implementation incorporates sufficient scale interaction. Then the effect of the fine scales becomes less pronounced and the R-VMS model approaches the no-model solution. This pattern occurs for all polynomial orders, which hints at the variational consistence of the method. The same pattern was observed in the convergence curves of the eddy viscosity model.

Figures 4.11b, 4.12b and 4.13b show the energy spectra corresponding to a 32 degrees of freedom discretization of the respective order basis functions. The energy spectra are again obtained by interpolation of the solution field, and a subsequent manipulation of the fast Fourier transform of the data set. The first 17 frequencies are zoomed into, which corresponds roughly to the Nyquist range. The energy spectra of the no-model solutions show significant deviations from the DNS solution for all modes. Even though these concern time averaged plots the no-model spectra behave highly irregular. On the other hand the curve that corresponds to the R-VMS solution is relatively smooth. This is in line with the stabilization interpretation of the R-VMS model.

These energy spectra do consistently show that too much energy is stored in the intermediate scale range, i.e., the dimple around $k = 13$. This is different from the energy spectra obtained by using a three-scale eddy viscosity model. That model specifically targets the intermediate scale range. Still this peak is much smaller than the corresponding spectral energies of the no-model solution in the same frequency range. It is conceivable that this dimple can be suppressed with an increase of the coefficients in Table 4.5. This could cause more diffusion in this scale range. In turn this would potentially lead to a more stable and smooth solution and probably a lower L^2 error. Still it was chosen to focus on the error in total energy, which showed optimal behavior for the current set of coefficients.

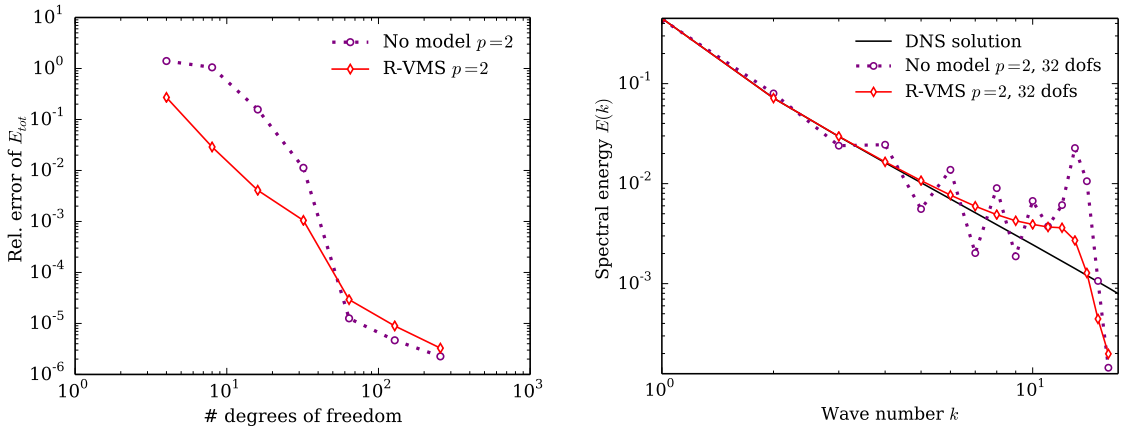

(a) Relative error in total energy at $t = 8\pi$.

(b) Spectral energy of the first 17 wave numbers. Average in $6\pi \leq t \leq 8\pi$.

Fig. 4.11: *Obtained energy convergence and spectrum for 2nd order B-spline basis functions. Including and excluding the R-VMS model.*

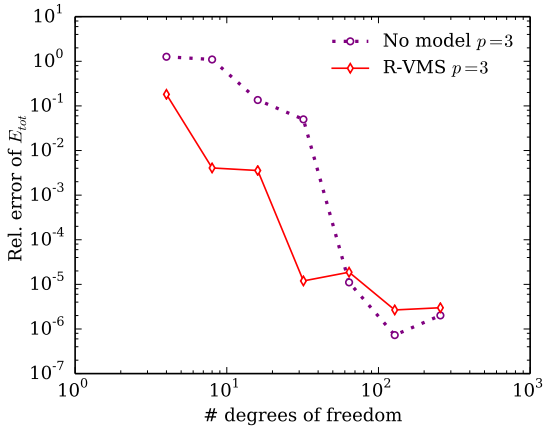

(a) Relative error in total energy at $t = 8\pi$.

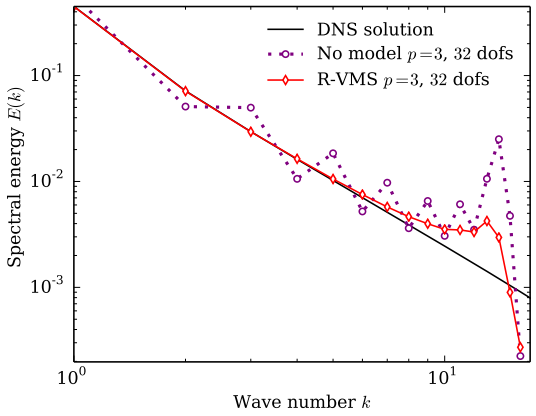

(b) Spectral energy of the first 17 wave numbers Average in $6\pi \leq t \leq 8\pi$.

Fig. 4.12: *Obtained energy convergence and spectrum for 3rd order B-spline basis functions. Including and excluding the R-VMS model.*

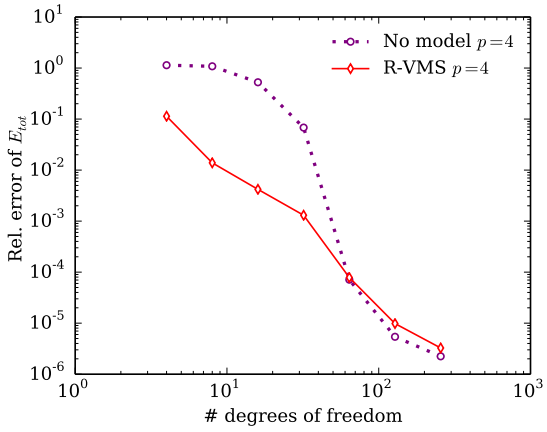

(a) Relative error in total energy at $t = 8\pi$

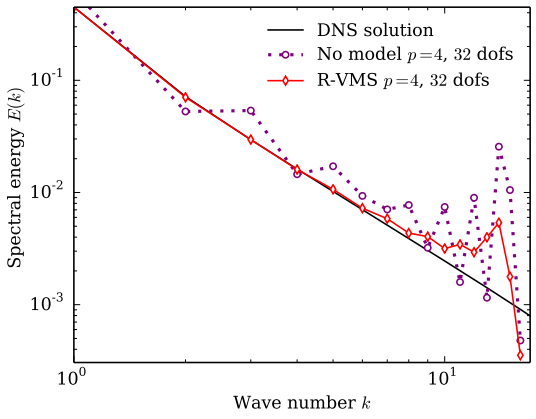

(b) Spectral energy of the first 17 wave numbers. Average in $6\pi \leq t \leq 8\pi$.

Fig. 4.13: *Obtained energy convergence and spectrum for 4th order B-spline basis functions. Including and excluding the R-VMS model.*

4.4 A discontinuous Galerkin residual-based variational multiscale approach

The fine scale model developed in the previous section will prove to be one piece of the puzzle when dealing with discontinuous discretizations. In this section the framework that was proposed in Chapter 3 will be applied to the Burgers equation. The added complexity requires certain approximations and modeling simplifications. By means of numerical experiments it is investigated how suitable these approximations are. This will serve to elevate the proposed DG-RVMS methodology from the controlled environment that was the focus of Chapter 3.

4.4.1 Model formulation

Similar to the previous section, the finite element formulation and the fine scale volumetric model will be derived from different weak forms. The finite element implementation will be based on the spatial weak formulation of Eq. (4.4). To ensure the existence of derivatives it is defined on a per-element basis. Substitution of a split of basis functions yields:

$$\text{Find } \bar{u}, u' \in \bar{\mathcal{V}} \times \mathcal{V}' \text{ s.t.:}$$
$$\begin{cases} \left(\bar{w}\,,\bar{u}_t+u'_t\right)_K+\frac{1}{2}\left(\bar{w}\,,\left((\bar{u}+u')^2\right)_x\right)_K-\left(\bar{w}\,,\nu(\bar{u}_{xx}+u'_{xx})\right)_K=\left(\bar{w}\,,f\right)_K & \forall\,\bar{w}\in\bar{\mathcal{V}} \\ \left(w',\bar{u}_t+u'_t\right)_K+\frac{1}{2}\left(w',\left((\bar{u}+u')^2\right)_x\right)_K-\left(w',\nu(\bar{u}_{xx}+u'_{xx})\right)_K=\left(w',f\right)_K & \forall\,w'\in\mathcal{V}' \end{cases} \tag{4.26}$$

Weak formulation Eq. (4.26) corresponds to steps 1 and 2 of the proposed strategy of Section 3.1.3. Step 3 suggest the use of integration by parts, resulting in the following formulation.

$$\begin{aligned} &\left(\bar{w},\bar{u}_t+u'_t\right)_K-\frac{1}{2}\left(\bar{w}_x,\bar{u}^2\right)_K-\left(\bar{w}_x,\bar{u}\,u'\right)_K+\frac{1}{2}\langle\bar{w},\left(\bar{u}+u'\right)^2\rangle_{\partial K} \\ &\quad+\left(\bar{w}_x,\nu\bar{u}_x\right)_K+\langle\bar{w},\nu\bar{u}_x\rangle_{\partial K}-\langle\bar{w},\nu u'_x\rangle_{\partial K}-\langle\bar{w}_x,\nu u'\rangle_{\partial K} \\ &\quad=\left(\bar{w}_{xx},\nu u'\right)_K+\frac{1}{2}\left(\bar{w}_x,u'^{\,2}\right)_K+\left(\bar{w},f\right)_K \quad \forall\,\bar{w}\in\bar{\mathcal{V}} \end{aligned} \tag{4.27}$$

The global weak formulation is obtained by summing over all elements. The elements are coupled by substituting the identities of Eq. (3.12) in place of the fine scale boundary values. This was step 4 of the DG-RVMS framework. The nonlinear advective term is the new term compared to the earlier analysis in Chapter 3. It will be rewritten as follows, where it is recognized that $\bar{u}+u'=u$ in the fourth term is single valued on element interfaces.

$$\begin{aligned} \sum_K\frac{1}{2}\langle\bar{w},u^2\rangle_{\partial K}&=\frac{1}{2}\langle[\![\bar{w}]\!],u^2\rangle_\Gamma=\frac{1}{2}\langle[\![\bar{w}]\!],\{\!\{u\}\!\}^2\rangle_\Gamma=\frac{1}{2}\langle[\![\bar{w}]\!],\{\!\{\bar{u}+u'\}\!\}^2\rangle_\Gamma \\ &=\frac{1}{2}\langle[\![\bar{w}]\!],\left(\{\!\{\bar{u}\}\!\}+\{\!\{u'\}\!\}\right)^2\rangle_\Gamma=\frac{1}{2}\langle[\![\bar{w}]\!],\{\!\{\bar{u}\}\!\}^2+2\{\!\{\bar{u}\}\!\}\{\!\{u'\}\!\}+\{\!\{u'\}\!\}^2\rangle_\Gamma \end{aligned} \tag{4.28}$$

The surface terms obtained from the diffusion term are manipulated as discussed in Section 3.2. Thereby the global weak formulation becomes:

$$\begin{aligned}(\bar{w}, \bar{u}_t + u'_t)_{\Omega_E} - \frac{1}{2}(\bar{w}_x, \bar{u}^2)_{\Omega_E} - (\bar{w}_x, \bar{u}\,u')_{\Omega_E} + \frac{1}{2}\langle [\![\bar{w}]\!], \{\!\{\bar{u}\}\!\}^2 + 2\{\!\{\bar{u}\}\!\}\{\!\{u'\}\!\} + \{\!\{u'\}\!\}^2 \rangle_\Gamma \\ (\bar{w}_x, \nu\bar{u}_x)_{\Omega_E} - \langle [\![\bar{w}]\!], \nu\,\{\!\{\bar{u}_x\}\!\}\rangle_\Gamma - \langle \{\!\{\bar{w}_x\}\!\}, \nu\,[\![\bar{u}]\!]\rangle_\Gamma - \langle [\![\bar{w}]\!], \nu\,\{\!\{u'_x\}\!\}\rangle_\Gamma + \langle [\![\bar{w}_x]\!], \nu\,\{\!\{u'\}\!\}\rangle_\Gamma \\ = (\bar{w}_{xx}, \nu u')_{\Omega_E} + \frac{1}{2}(\bar{w}_x, u'^{\,2})_{\Omega_E} + (\bar{w}, f)_{\Omega_E} \quad \forall\, \bar{w} \in \bar{\mathcal{V}}\end{aligned} \tag{4.29}$$

This weak formulation is identically satisfied by the exact solution. No approximations have been introduced. However, recall that this formulation itself is an insufficient condition to define $\bar{u}$ and u'. One of the main conclusions of Chapter 3 was that a DG formulation is not well posed without additional constraints on the fine scale solution. For this purpose a fine scale surface model is required; step 5 in Section 3.1.3. In the spatial dimension the Burgers equation is similar to the advection-diffusion model problem discussed in Section 3.3. Therefore, the proposed surface model leans heavily on those obtained in the section on advection-diffusion mixed surface models (Section 3.3.4):

$$\begin{cases} \{\!\{u'\}\!\}\Big|_{\hat{x}} = 0 & \hat{x} \in \Gamma \\ \{\!\{u'_x\}\!\}\Big|_{\hat{x}} = -(\frac{1}{2\nu}\{\!\{\bar{u}\}\!\}\Big|_{\hat{x}} + \eta h^{-1})\,[\![\bar{u}]\!]\Big|_{\hat{x}} & \hat{x} \in \Gamma \end{cases} \tag{4.30}$$

This fine scale surface model effectively combines an interior penalty method and an upwinding method with an advective velocity of magnitude $u = \{\!\{\bar{u}\}\!\}$. By substituting these modeling choices into the respective terms in Eq. (4.29), the following well-posed coarse scale weak formulation is obtained.

$$\begin{aligned}(\bar{w}, \bar{u}_t + u'_t)_{\Omega_E} - \frac{1}{2}(\bar{w}_x, \bar{u}^2)_{\Omega_E} - (\bar{w}_x, \bar{u}\,u')_{\Omega_E} + \frac{1}{2}\langle [\![\bar{w}]\!], \{\!\{\bar{u}\}\!\}\,\bar{u}(\lim_{\epsilon\to 0} x - \epsilon\bar{u})\rangle_\Gamma \\ + (\bar{w}_x, \nu\bar{u}_x)_{\Omega_E} - \langle [\![\bar{w}]\!], \nu\,\{\!\{\bar{u}_x\}\!\}\rangle_\Gamma - \langle \{\!\{\bar{w}_x\}\!\}, \nu\,[\![\bar{u}]\!]\rangle_\Gamma + \langle [\![\bar{w}]\!], \eta h^{-1}\,\nu\,[\![\bar{u}]\!]\rangle_\Gamma \\ = (\bar{w}_{xx}, \nu u')_{\Omega_E} + \frac{1}{2}(\bar{w}_x, u'^{\,2})_{\Omega_E} + (\bar{w}, f)_{\Omega_E} \quad \forall\, \bar{w} \in \bar{\mathcal{V}}\end{aligned} \tag{4.31}$$

At this stage all surface terms have been freed of fine scale contributions. Note that still no approximations have been made. The incorporated fine scale surface model is sufficient to fix the separation into $\bar{u}$ and u' for a given exact solution. However, the weak formulation is still not self-contained; volumetric fine scale terms remain. A volumetric fine scale model is required to close the coarse scale formulation. This is dealt with in the last step of the DG-RVMS roadmap.

The volumetric fine scale model will again be based on the space-time fine scale weak formulation. This weak formulation is defined for each separate space-time element. Thereby,

existence of derivatives is ensured.

$$\text{Find } \bar{u}, u' \in \bar{\mathcal{V}}_{Q_K^n} \times \mathcal{V}'_{Q_K^n} \text{ s.t.:}$$
$$\begin{cases} \left(\bar{w}\,,\, \bar{u}_t + u'_t\right)_{Q_K^n} + \frac{1}{2}\left(\bar{w}\,,\, \left((\bar{u}+u')^2\right)_x\right)_{Q_K^n} - \left(\bar{w}\,,\, \nu(\bar{u}_{xx}+u'_{xx})\right)_{Q_K^n} = \left(\bar{w}\,,\, f\right)_{Q_K^n} & \forall\, \bar{w} \in \bar{\mathcal{V}}_{Q_K^n} \\ \left(w',\, \bar{u}_t + u'_t\right)_{Q_K^n} + \frac{1}{2}\left(w',\, \left((\bar{u}+u')^2\right)_x\right)_{Q_K^n} - \left(w',\, \nu(\bar{u}_{xx}+u'_{xx})\right)_{Q_K^n} = \left(w',\, f\right)_{Q_K^n} & \forall\, w' \in \mathcal{V}'_{Q_K^n} \end{cases} \tag{4.32}$$

The second equation in Eq. (4.32), the space-time fine scale weak formulation, can be rewritten into Eq. (4.33). The quadratic advective term is expanded and the coarse scale components are brought to the right hand side. These components are collected into the coarse scale residual, which is paired with the fine scale test function.

$$\begin{aligned} \left(w', u'_t\right)_{Q_K^n} + \left(w', u'u'_x\right)_{Q_K^n} + \left(w', \bar{u}_x u'\right)_{Q_K^n} + \left(w', \bar{u}u'_x\right)_{Q_K^n} - \left(w', \nu u'_{xx}\right)_{Q_K^n} = \\ \left(w', -\bar{u}_t - \frac{1}{2}(\bar{u}^2)_x + \nu \bar{u}_{xx} + f\right)_{Q_K^n} = \left(w', \mathcal{R}_{\bar{u}}\right)_{Q_K^n} \end{aligned} \tag{4.33}$$

This is exactly the weak formulation of Eq. (4.17), although now confined to element K. Just like before it is assumed that the fine scale solution is small compared to the coarse scale solution. The advective effect of u' is therefore neglected, which effectively removes any nonlinear fine scale terms. These approximations warrant the use of the finite element approximation u_h in place of the true coarse scale solution $\bar{u}$. The corresponding strong form is different in a DG setting than it was in the isogeometric setting of Section 4.3. The fine scale solution now does include element-boundary values. These must be included as boundary conditions:

$$\begin{cases} u'_t + u_{hx}\, u' + u_h\, u'_x - \nu\, u'_{xx} = \mathcal{R}_{u_h} & x, t \in Q_K^n \\ u' = u'_{\mathcal{P}} & x, t \in \partial K \times [\, t^n\,,\, t^n + \Delta t\,] \equiv \chi \\ u' = 0 & x, t \in K \times \{t^n, t^{n+1}\} \equiv \Upsilon^n \cup \Upsilon^{n+1} \end{cases} \tag{4.34}$$

The initial value is still assumed to be zero, since no history variable is introduced.

As discussed in Section 3.3 and Appendix A the volumetric fine scale term is treated as follows:

$$u' \approx \tau \mathcal{R}_{u_h} + \gamma_0 \nu u'_j - \gamma_1 \nu u'_{j+1} \tag{4.35}$$

Treatment of the τ parameter has been discussed in the previous section. It is based on the Green's function of the differential operator provided in Eq. (4.36). This equation also shows the adjoint differential operator, and the accompanying surface integrals. The γ terms are obtained based on these surface integrals. This is elaborated on in Appendix A. To obtain their expression the boundary values from Eq. (4.34) must be substituted into the surface integrals. Additionally, the Green's function is substituted in place of w'. Due to the zero initial value and since the Green's function is by definition zero on the boundary ∂K, only

the term that involves the derivative of the Green's function remains.

$$\begin{aligned}
\mathscr{L} &= \frac{\mathrm{d}}{\mathrm{d}t} + u_{hx} + u_h \frac{\mathrm{d}}{\mathrm{d}x} - \nu \frac{\mathrm{d}^2}{\mathrm{d}x^2} \\
\mathscr{L}^* &= -\frac{\mathrm{d}}{\mathrm{d}t} + u_{hx} - u_h \frac{\mathrm{d}}{\mathrm{d}x} - \nu \frac{\mathrm{d}^2}{\mathrm{d}x^2} \\
k(w', u') &= -\langle w', n u' \rangle_{\Upsilon^n} + \langle w', u' \rangle_{\Upsilon^{n+1}} + \\
&\qquad \langle w'\, n\, , u_h u' \rangle_\chi - \langle w'\, n, \nu u'_x \rangle_\chi + \langle w'_x, \nu\, n\, u' \rangle_\chi
\end{aligned} \tag{4.36}$$

The τ was constructed based on asymptotic scaling arguments. Refer to Eq. (4.24). In a similar fashion the γ values are also based on the separate differential operators (temporal, reactive, advective and diffusive). As shown in Appendix A only the γ corresponding to the diffusion operator is nonzero. The τ, γ_0 and γ_1 that will be used for the numerical computations are:

$$\tau = \frac{1}{\sqrt{\frac{4h^2}{\Delta t^4} C_1^{2-2k} + u_{h_x}^2 C_2^{2-2p} + \frac{4{u_h}^2}{h^2} C_2^{2-2p} + \frac{144\nu^2}{h^4} C_2^{2-2p}}} \tag{4.37}$$

$$\gamma_0 = C_3^{1-1p} \gamma_{D,0} = C_2^{1-1p} \frac{1}{2\nu} \tag{4.38}$$

$$\gamma_1 = C_3^{1-1p} \gamma_{D,1} = -C_2^{1-1p} \frac{1}{2\nu} \tag{4.39}$$

In these expressions the coefficients C_1, C_2 and C_3 aim to take into account the effect of the higher order discretization. Hence p is the polynomial order of the basis functions, and k is the order of the local truncation error of the time stepping scheme. This is elaborated on in more detail in the previous section.

The final step is to obtain expressions for u'_j and u'_{j+1}. These are fixed by virtue of the fine scale surface model that was introduced earlier. In particular Eq. (4.30) dictates that $\{\!\{u'\}\!\} = 0$ on the border. Additionally, the continuity condition of u requires $[\![u']\!] = -[\![\bar{u}]\!]$. Thereby:

$$\begin{aligned}
u'_j &= \frac{1}{2}[\![u']\!]\Big|_{x_j} \cdot n_j &&= -\frac{1}{2}[\![\bar{u}]\!]\Big|_{x_j} \cdot n_j &&\approx \frac{1}{2}[\![u_h]\!]\Big|_{x_j} \\
u'_{j+1} &= \frac{1}{2}[\![u']\!]\Big|_{x_{j+1}} \cdot n_{j+1} &&= -\frac{1}{2}[\![\bar{u}]\!]\Big|_{x_{j+1}} \cdot n_{j+1} &&\approx -\frac{1}{2}[\![u_h]\!]\Big|_{x_{j+1}}
\end{aligned} \tag{4.40}$$

With the use of these surface values the volumetric fine scale model in a DG framework is proposed as follows:

$$u' \approx u'_h = \tau \mathscr{R}_{u_h} + \frac{1}{4} C_3^{1-1p} [\![u_h]\!]\Big|_{x_j} - \frac{1}{4} C_3^{1-1p} [\![u_h]\!]\Big|_{x_{j+1}} \tag{4.41}$$

Note the new notation u'_h as the approximation to u'. This volumetric fine scale model is substituted into the coarse scale formulation of Eq. (4.31). Additionally, the time derivative of the fine scale solution is neglected, as it is assumed this has a negligible average effect. Thereby, the following global, closed, finite element formulation is obtained. Recall that the finite element solution u_h is used in place of $\bar{u}$, to indicate that the previously described approximations will yield an approximate coarse scale solution.

$$\begin{aligned}(\bar{w}, u_{ht})_{\Omega_E} - \frac{1}{2}(\bar{w}_x, {u_h}^2)_{\Omega_E} - (\bar{w}_x, u_h\, u'_h)_{\Omega_E} + \frac{1}{2}\langle [\![\bar{w}]\!], \{\!\{u_h\}\!\}\, u_h(\lim_{\epsilon\to 0} x - \epsilon u_h)\rangle_\Gamma \\ + (\bar{w}_x, \nu u_{hx})_{\Omega_E} - \langle [\![\bar{w}]\!], \nu\, \{\!\{u_{hx}\}\!\}\rangle_\Gamma - \langle \{\!\{\bar{w}_x\}\!\}, \nu\, [\![u_h]\!]\rangle_\Gamma + \langle [\![\bar{w}]\!], \eta h^{-1}\, \nu\, [\![u_h]\!]\rangle_\Gamma \\ = (\bar{w}_{xx}, \nu u'_h)_{\Omega_E} + \frac{1}{2}(\bar{w}_x, {u'_h}^2)_{\Omega_E} + (\bar{w}, f)_{\Omega_E} \quad \forall\, \bar{w} \in \bar{\mathcal{V}}\end{aligned} \tag{4.42}$$

The implementation of this DG-RVMS model will again make use of an explicit Runge-Kutta time stepping algorithm. Just like in the R-VMS model of Section 4.3 the coarse scale residual is obtained from each previous α-step in the Runge-Kutta scheme (refer to Section 4.1.2). For the fine scale volumetric model the jump terms are also explicitly obtained from the previous coarse scale solution.

4.4.2 Numerical results

The proposed model is implemented with the RK4 time stepping scheme of Table 4.2. The numerical experiments make use of a time step of $\Delta t = \pi/(8\,p\,N)$. Again $k = 5$ due to the fifth order accurate local truncation error of the RK4 scheme. Figures 4.14 and 4.15 show the resulting solutions at times $t = 7.5\pi$ and $t = 8\pi$ respectively. At $t = 7.5\pi$ the wave front lies in the center of an element. The results of two different sets of DG-RVMS coefficients are shown in the figures.

An important thing to note from these solutions is that the no-model solution is performing relatively well by itself. The oscillations are nearly confined within the element that neighbors the shock wave. This is part of the reason why it was chosen to focus most on energy measures to assess the quality of the solutions. The good L^2-norm behavior of the no-model solution in this 1D Burgers case might not translate to good L^2-norm behavior in a complex 3D Navier-Stokes simulation. However, when the model aims to achieve accurate scale interaction, in terms of energy transfer, then this may be expected to have a positive impact also in the case of complex problems.

That being said, the C_1 and C_2 coefficients of the DG-RVMS model could also be optimized to reduce the L^2 error. This can be observed by comparing the two DG-RVMS solutions in Figures 4.14 and 4.14. The computation that made use of higher values for the coefficients C_1 and C_2 results in a finite element solution that adheres closer to the DNS solution. However, it turns out that the finite element solution that used lower values for these coefficients actually yields a lower error in total energy. A similar conclusion was drawn in Section 4.3.3. There it was argued that the B-spline R-VMS solution might stabilize further when higher coefficients were used. Also in that case the optimal L^2 result was not the solution that minimizes the error in total energy. Both cases show that different choices of coefficients are required for different objectives.

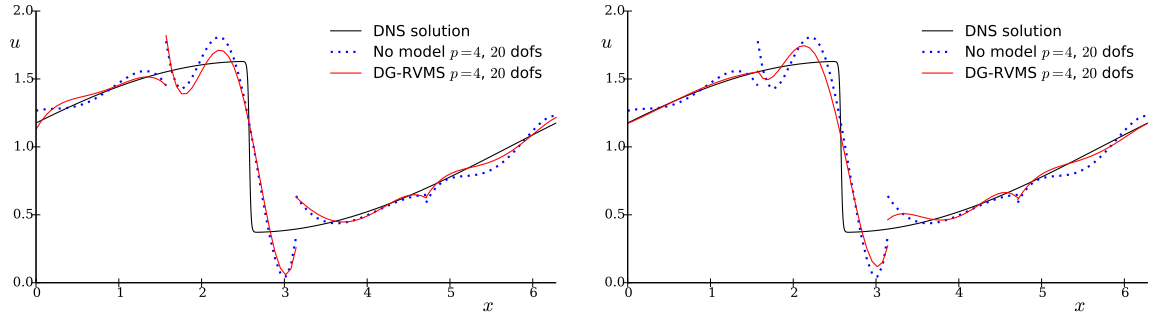

(a) Model with $C_1 = 2$, $C_2 = 0.7$ and $C_3 = 0.3$. **(b)** Model with $C_1 = 5$, $C_2 = 5$ and $C_3 = 0.3$.

Fig. 4.14: *Example solutions at $t = 7.5\pi$, with and without proposed DG-RVMS model. Using a total of 4 $p = 4$ discontinuous elements.*

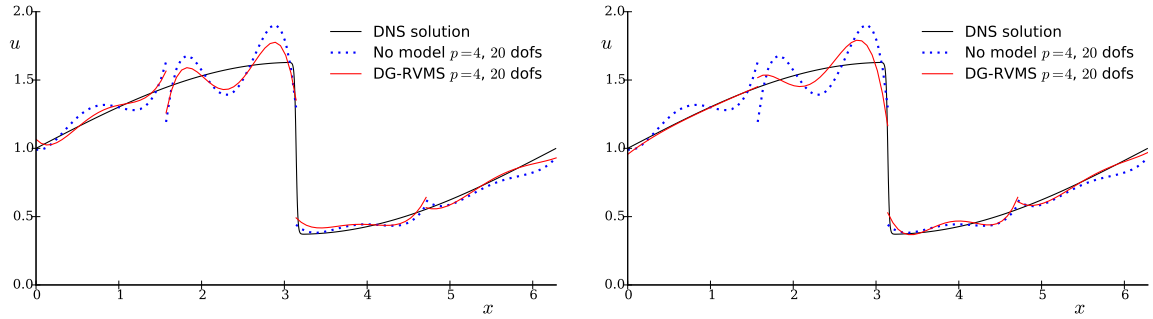

(a) Model with $C_1 = 2$, $C_2 = 0.7$ and $C_3 = 0.3$. **(b)** Model with $C_1 = 5$, $C_2 = 5$ and $C_3 = 0.3$.

Fig. 4.15: *Example solutions at $t = 8\pi$, with and without proposed DG-RVMS model. Using a total of 4 $p = 4$ discontinuous elements.*

Next, the convergence in total energy of the solution is examined at time $t = 8\pi$. A relative error is obtained by means of the average total energy of the DNS solution at $6\pi \leq t \leq 8\pi$. Three sets of experiments were executed to asses the convergence quality of the proposed DG-RVMS model. One of the curves in Figures 4.16a, 4.17a and 4.18a refers to a solution that includes the complete fine scale volumetric model as described in Eq. (4.41). Another solution, called the 'Naive R-VMS' solution, omits the jump terms from the model of Eq. (4.41). Implementation wise this means $C_3 = 0$. The last curve is the reference solution that excludes the volumetric fine scale term altogether. Each of the figures comes with a table that shows the coefficients that were used.

The increase in performance of the DG-RVMS model spans the complete range of degrees of freedom, for all polynomial orders. This is different from the previous (R-)VMS models, which purely saw a performance boost for coarse discretizations. Interestingly the naive R-VMS implementation ($C_3 = 0$) hardly sees any performance increase. The curves in the

convergence plots make use of C_1 and C_2 coefficients that minimize the error, yet for the naive R-VMS version this had little effect. Apparently it is the effect of the fine scale boundary conditions that is of primary importance to the R-VMS model in discontinuous Galerkin framework. This is precisely the modeling aspect that is new compared to the classical R-VMS model. The DG-RVMS curves that did include these terms made use of constant coefficients $C_1 = C_2 = 0.7$ throughout all computations. This was felt to yield the most consistent test frame. Potentially the tweaking of these two coefficients could increase the performance of the DG-RVMS implementation even further. On the other hand, the C_3 coefficients were optimized for each DG-RVMS computation. Generally, it was found that this parameter should decrease with element size.

Finally, the energy spectra are examined for one particular solution of each convergence study. Figures 4.16b, 4.17b and 4.18b show the first 11 wave numbers of respectively a $p = 2$, $p = 3$ and $p = 4$ polynomial order discretization. The total number of degrees of freedom used for the computation changes per graph, but the wave number of 11 is always close to the approximate Nyquist cut-off frequency. Only a low range of wave numbers is of interest, as the higher frequencies will by polluted by the effect of the jumps. Recall that the spectral energy is obtained via a fast Fourier transform of an interpolated set of pointwise solution values. The energy spectra are time averaged in the range $6\pi \leq t \leq 8\pi$.

The performance increase in terms of spectrum smoothness is less pronounced for the DG implementation than it was for either previous VMS model (i.e., the eddy viscosity model and the B-spline implementation). This is in line with the high performance of the DG implementation that was observed in Figures 4.14 and 4.15, even without a fine scale volumetric model. Nonetheless a careful inspection of the figures shows that the DG-RVMS method consistently outperforms the no-model variant. The spectral energy of the lowest wave numbers more closely follows the DNS spectrum. This becomes more apparent for the higher order polynomial basis functions. These computations include fewer discontinuous element for the same number of degrees of freedom, so they behave more like the continuous Galerkin results obtained in Section 4.2.3. For the highest polynomial orders the spectrum also behaves more smoothly.

Overall these results are very convincing. The fact that the error is reduced by a significant factor across a wide range of discretizations indicates that the model truly incorporates a missing component of the formulation. This improvement is the result of relatively simple expressions for the τ and γ parameters. Conceivably more involved expressions would improve solution behavior even further.

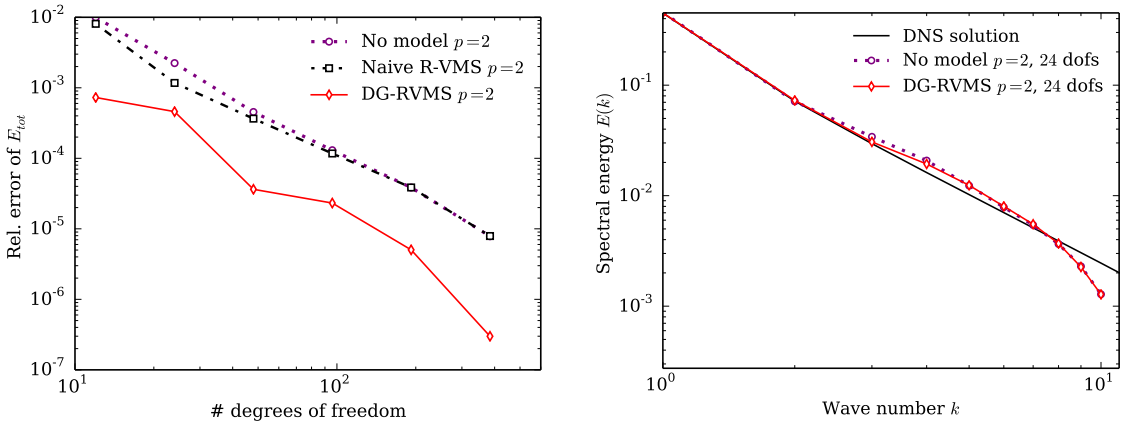

(a) Relative error in total energy at $t = 8\pi$.

(b) Spectral energy of the first 11 wave numbers. Average in $6\pi \leq t \leq 8\pi$.

Fig. 4.16: *Obtained energy convergence and spectrum for 2nd order polynomial basis functions. Including and excluding the DG-RVMS model.*

Table 4.6: *Parameters used for the numerical experiments in Figure 4.16.*

	DG-RVMS						Naive R-VMS					
Dofs:	12	24	48	96	192	384	12	24	48	96	192	384
C_1	0.7	0.7	0.7	0.7	0.7	0.7	3	3	2	2	0.7	0.7
C_2	0.7	0.7	0.7	0.7	0.7	0.7	0.7	0.7	0.7	0.7	0.7	0.7
C_3	0.1	0.1	0.1	0.1	0.1	0.1	0	0	0	0	0	0

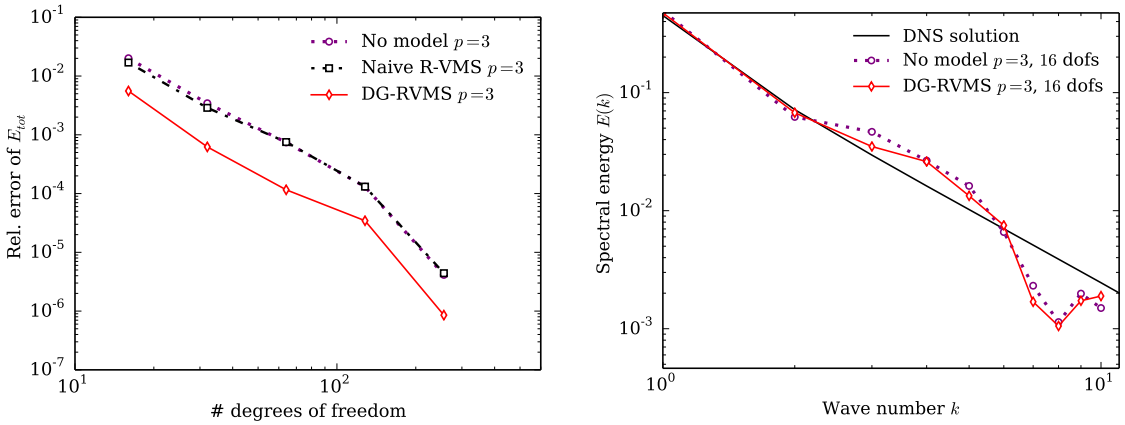

(a) Relative error in total energy at $t = 8\pi$.

(b) Spectral energy of the first 11 wave numbers. Average in $6\pi \leq t \leq 8\pi$.

Fig. 4.17: *Obtained energy convergence and spectrum for 3rd order polynomial basis functions. Including and excluding the DG-RVMS model.*

Table 4.7: *Parameters used for the numerical experiments in Figure 4.17.*

	DG-RVMS					Naive R-VMS				
Dofs	16	32	64	128	256	16	32	64	128	256
C_1	0.7	0.7	0.7	0.7	0.7	3	3	2	0.7	0.7
C_2	0.7	0.7	0.7	0.7	0.7	0.7	0.7	0.7	0.7	0.7
C_3	0.3	0.2	0.2	0.1	0.025	0	0	0	0	0

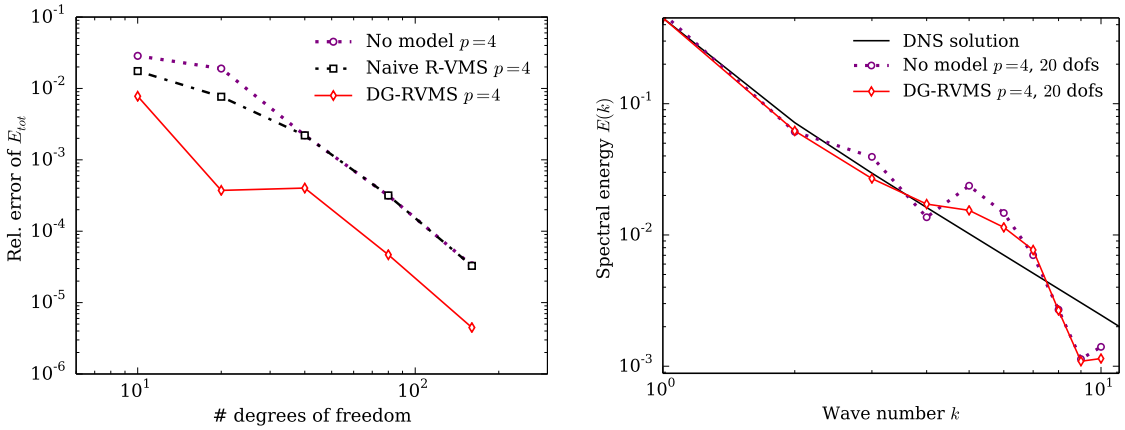

(a) Relative error in total energy at $t = 8\pi$

(b) Spectral energy of the first 11 wave numbers. Average in $6\pi \leq t \leq 8\pi$.

Fig. 4.18: *Obtained energy convergence and spectrum for 4th order polynomial basis functions. Including and excluding the DG-RVMS model.*

Table 4.8: *Parameters used for the numerical experiments in Figure 4.18.*

	DG-RVMS					Naive R-VMS				
Dofs	10	20	40	80	160	10	20	40	80	160
C_1	0.7	0.7	0.7	0.7	0.7	3	3	2	0.7	0.7
C_2	0.7	0.7	0.7	0.7	0.7	0.7	0.7	0.7	0.7	0.7
C_3	0.3	0.3	0.3	0.3	0.025	0	0	0	0	0

Chapter 5

Synopsis and outlook

The classical residual-based variational multiscale method leans heavily on the continuity of the finite element basis. The additional volumetric term includes higher order derivatives of both the test function and the trial function. An insufficiently smooth solution basis would lead to inconsistent integration due to the occurrence of Dirac layers between elements. The use of a discontinuous solution basis therefore requires significant conceptual changes to the R-VMS method.

First of all, the coarse scale weak formulation cannot immediately extend past a single element. This would introduce the problematic Dirac layers. Secondly, it has been shown that within such an element the coarse scale and fine scale function spaces share basis functions. This is problematic since the split into the two weak formulations is no longer sufficiently constrained. The DG-RVMS methodology that was developed mitigates both issues while capturing (and making use of) the multiscale nature of the solution. The proposed roadmap can be condensed into three sections:

Part 1: Obtaining a global formulation. Whilst the weak formulation has to be contained within each element, intra-element coupling is required to solve the global system of equations. It is shown that the element coupling can be enforced by manipulating the fine scale per-element boundary terms. In particular the identities in Eq. (5.1) are used. These identities hold for $\mathscr{C}^1$ continuous exact solutions. The coarse scale element-to-element coupling is thus dictated by the multiscale nature of the solution.

$$\begin{aligned} \llbracket u' \rrbracket = -\llbracket \bar{u} \rrbracket \qquad &\Rightarrow \qquad u'^{\pm}\, n^{\pm} \quad = \{\!\{ u' \}\!\}\, n^{\pm} - \frac{1}{2} \llbracket \bar{u} \rrbracket \\ \llbracket \nabla u' \rrbracket = -\llbracket \nabla \bar{u} \rrbracket \qquad &\Rightarrow \qquad \nabla u'^{\pm} \cdot n^{\pm} = \{\!\{ \nabla u' \}\!\} \cdot n^{\pm} - \frac{1}{2} \llbracket \nabla \bar{u} \rrbracket \end{aligned} \tag{5.1}$$

Part 2: Introducing a fine scale surface model. The globally coupled coarse scale weak formulation is not well posed due to the second point that was brought up. In order to constrain the formulations further, a fine scale surface model is required. The surface

model will be substituted into the remaining fine scale terms in the global coarse scale weak formulation. Thereby, the coarse scale weak formulation becomes well defined. It has been shown that many known DG formulations can be interpreted as a variational multiscale formulation with a particular choice of fine scale surface model. In case of a second order elliptic operator this has been investigated for the interior penalty method, the NIPG method and the Baumann-Oden method. For example, the interior penalty formulation for a Laplace problem was shown to implicitly enforce the fine scale surface model of Eq. (5.2). The implicit fine scale surface model for an upwind numerical flux has also been looked at for both advection dominated, and advection-diffusion problems. The overall conclusion is that the numerical traces introduced in many classical DG derivations are not, in fact, approximations to the true solution. Instead, they enforce a fine scale surface model that poses a sufficient constraint on the global system of equations.

$$\begin{cases} \{\!\{u'\}\!\}\Big|_{\hat{x}} = 0 & \hat{x} \in \Gamma \\ [\![u']\!]\Big|_{\hat{x}} = 2d\,\{\!\{\nabla u'\}\!\}\Big|_{\hat{x}} & \hat{x} \in \Gamma \end{cases} \tag{5.2}$$

Part 3: Introducing a fine scale volumetric model. Once the formulation has been sufficiently constrained by means of a fine scale surface model, the volumetric fine scale terms are dealt with. These are the terms of focus in the classical R-VMS methods. They capture the volumetric effect of the fine scale solution onto the coarse scale discretization. In a DG framework this term is generally not taken into account. For advection based PDEs this introduces a modeling error. It is shown that the use of upwind fluxes serves as an ad hoc remedy for the omission of the fine scale volumetric term. More accurate schemes can be developed by incorporating residual-based models.

Prior R-VMS formulations have always assumed zero element boundary values for the fine scale problem. Within a DG framework this would be a particularly erroneous approximation. The discontinuous nature of the fine scale solution directly implies a significant fine scale boundary contribution, as per Eq. (5.1). Knowledge of the discontinuity can be leveraged to obtain a better volumetric fine scale model. The fine scale boundary conditions can be inspired (or in some cases obtained) from the fine scale surface information that is enforced by the fine scale surface model. In particular, the fine scale surface model of Eq. (5.2) can be substituted into Eq. (5.1) to obtain an expression for the fine scale solution at the element boundary. This expression can be leveraged to complement the classical residual-based model:

$$u' \approx \tau \mathscr{R}_{\bar{u}} + \gamma_0 \frac{1}{2}[\![\bar{u}]\!]\Big|_{x_j} + \gamma_1 \frac{1}{2}[\![\bar{u}]\!]\Big|_{x_{j+1}} \tag{5.3}$$

In this equation the j and $j+1$ iterators indicates values on the left and right element boundaries. $\mathscr{R}_{\bar{u}}$ is the coarse scale residual, and $[\![\bar{u}]\!]$ the jump of the coarse scale solution across the element boundary. The γ and τ parameters depend on the fine scale problem. In the current work they were obtained from average Green's function quantities. Their expressions, as well as the formulation of Eq. (5.3), have been verified for a 1D advection-diffusion equation. Remarkably the $\tau\mathscr{R}_{\bar{u}}$ term is the same as in classical VMS formulations. Even the equation

for τ is identical. The predominant difference for the R-VMS method in a DG framework thus lies in the addition of the $\gamma\frac{1}{2}[\![\bar{u}]\!]$ terms.

With a firm foundation of the DG-RVMS methodology at hand, the remaining of the work investigated its effectiveness in the context of the Burgers equation. The 1D Burgers equation is known to exhibit turbulent behavior that has a strong multiscale nature. Energy traverses from low frequency modes to high frequency modes. This feature, plus the more complex nonlinear, transient, structure of the PDE makes it a suitable test case. The numerical experiments that were performed indicated a strong effect of the γ terms. Addition thereof reduced the relative error of the total energy by nearly an order of magnitude for a range of discretizations. On the other hand, the effect of τ was far less pronounced than it was for the experiments that made use of B-spline basis functions and a classical R-VMS model. This indicated that the change of fine scale model as proposed in Eq. (5.3) is well suited for DG formulations.

The newly developed DG-RVMS framework can serve as the groundwork on which further research may be based. Specific suggestion for future work are:

↪ More sophisticated fine scale volumetric models could be implemented. For instance, the dynamics subgrid scale model by Codina *et al.* could be introduced [72]. The transient nature of the fine scales is incorporated in the coarse scale formulation. Another potential aspect of improvement is the expression of the γ's. In the current implementation they are based on each of the separate components of the Burgers equation. Effectively these reduce to the γ's associated to a Laplace operator. More involved expressions could be derived that also incorporate the fine scale advective nature.

↪ The fine scale surface model interpretation may serve as a basis for the development of novel DG formulations. Potentially fine scale surface models can be developed that aim to retrieve the coarse scale solution corresponding to a particular projection (e.g. an L^2 projection).

↪ More appropriate fine scale surface models and volumetric fine scale models could be inspired by known physical behavior of the system. A typical example is the energy cascade observed in turbulent flow.

↪ Along the same line, the performance of the current DG-RVMS method may be assessed in the context of Navier-Stokes turbulence.

↪ The theory may be tailored to suit a cut-cell implementation. In such a framework the domain cuts through the elements. This alleviates the complexity of the meshing procedure. Locally these cut elements may be interpreted as DG elements [75]. Stabilization issues have been reported for these elements [76]. Potentially a local DG-RVMS method may inspire new stabilization procedures.

↪ The proposed DG-RVMS framework can be applied to a mixed method formulation. Appendix B shows that the classical DG formulations for a Laplace operator are obtained from a mixed formulation. Perhaps additional classical DG formulations can be retrieved by using the DG-RVMS strategy on the same original setting. Many of the classical formulations include so-called lifting operators. These are volumetric terms that include

element boundary jump contributions. It is conceivable that these can be interpreted as part of the DG-RVMS volumetric fine scale model. Additionally, a mixed formulation origin may provide more angles for manipulation of the fine scale terms.

The value of the DG-RVMS framework extends past this list of potential applications. The framework serves as a new point of view from which discontinuous Galerkin formulations may be understood. The framework explains the curious stability behavior of the Baumann-Oden method, and the effectiveness of concepts such as upwinding. These insights flow naturally from the discontinuous Galerkin residual-based variational multiscale methodology proposed in this work. I am curious to see what further shadowy facets of the discontinuous Galerkin method will be illuminated by its utilization.

References

[1] T. J. R. Hughes, G. R. Feijóo, L. Mazzei, and J.-B. Quincy. The variational multiscale method – a paradigm for computational mechanics. *Computer Methods in Applied Mechanics and Engineering*, 166(1-2):3–24, 1998.

[2] Y. Bazilevs, V. M. Calo, J. A. Cottrell, T. J. R. Hughes, A. Reali, and G. Scovazzi. Variational multiscale residual-based turbulence modeling for large eddy simulation of incompressible flows. *Computer Methods in Applied Mechanics and Engineering*, 197(1-4):173–201, 2007.

[3] S. Loehnert and T. Belytschko. A multiscale projection method for macro/microcrack simulations. *International Journal for Numerical Methods in Engineering*, 71(12):1466–1482, 2007.

[4] N. Hutchins and I. Marusic. Large-scale influences in near-wall turbulence. *Philosophical Transactions of the Royal Society A: Mathematical, Physical and Engineering Sciences*, 365(1852):647–664, 2007.

[5] C. G. Moreno. Turbulence, Vibrations, Noise and Fluid Instabilities. Practical Approach. In *Computational Fluid Dynamics*. InTech, 2010.

[6] L. Corradi. On compatible finite element models for elastic plastic analysis. *Meccanica*, 13(3):133–150, 1978.

[7] A. Hund and E. Ramm. Locality constraints within multiscale model for non-linear material behaviour. *International Journal for Numerical Methods in Engineering*, 70(13):1613–1632, 2007.

[8] T. J. R. Hughes, G. Scovazzi, and L. P. Franca. Multiscale and stabilized methods. In E. Stein, R. De Borst, and T. J. R. Hughes, editors, *Encyclopedia of computational mechanics*, chapter 4. John Wiley & Sons, Ltd, 2004.

[9] V. M. Calo. *Residual–based Multiscale Turbulence modeling: Finite Volume simulations of bypass transition.* PhD thesis, Stanford University, 2004.

[10] B. Cockburn, E. K. George, and C.-W. Shu. *Discontinuous Galerkin methods: Theory, Computation and Applications.* Springer, Berlin, Heidelberg, 11th edition, 2000.

[11] D. N. Arnold, F. Brezzi, B. Cockburn, and L. D. Marini. Unified Analysis of Discontinuous Galerkin Methods for Elliptic Problems. *SIAM Journal on Numerical Analysis*, 39(5):1749–1779, 2002.

[12] J. Peraire and P.-O. Persson. High-Order Discontinuous Galerkin Methods for CFD. In Z. J. Wang, editor, *Adaptive high-order methods in computational fluid dynamics*, volume 2, chapter 5. 2011.

[13] Z. J. Wang, K. Fidkowski, R. Abgrall, F. Bassi, D. Caraeni, A. Cary, H. Deconinck, R. Hartmann, K. Hillewaert, H. T. Huynh, N. Kroll, G. May, P.-O. Persson, B. van Leer, and M. Visbal. High-Order CFD Methods: Current Status and Perspective. *International Journal for Numerical Methods in Fluids*, 72(8):811–845, 2013.

[14] B. Cockburn, J. Gopalakrishnan, and R. Lazarov. Unified hybridization of discontinuous Galerkin, mixed, and continuous Galerkin methods for second order elliptic problems. *SIAM Journal on Numerical Analysis*, 47(2):1319–1365, 2009.

[15] N. C. Nguyen, J. Peraire, and B. Cockburn. A hybridizable discontinuous Galerkin method for Stokes flow. *Computer Methods in Applied Mechanics and Engineering*, 199(9):582–597, 2010.

[16] N. C. Nguyen, J. Peraire, and B. Cockburn. An implicit high-order hybridizable discontinuous Galerkin method for linear convection–diffusion equations. *Journal of Computational Physics*, 228(9):3232–3254, 2009.

[17] R. M. Kirby, S. J. Sherwin, and B. Cockburn. To CG or to HDG: A comparative study. *Journal of Scientific Computing*, 51(1):183–212, 2012.

[18] A. Huerta, A. Angeloski, X. Roca, and J. Peraire. Efficiency of high-order elements for continuous and discontinuous Galerkin methods. *International Journal for Numerical Methods in Engineering*, 96(9):529–560, 2013.

[19] HiOCFD4 4th International Workshop on High-Order CFD Methods. `https://how4.cenaero.be/`. Accessed: June 16th 2017.

[20] I. Akkerman, Y. Bazilevs, V. M. Calo, T. J. R. Hughes, and S. J. Hulshoff. The role of continuity in residual–based variational multiscale modeling of turbulence. *Computational Mechanics*, 41(3):371–378, 2008.

[21] T. J. R. Hughes. Multiscale phenomena: Green's functions, the Dirichlet–to–Neumann formulation, subgrid scale models, bubbles and the origins of stabilized methods. *Computer Methods in Applied Mechanics and Engineering*, 127(1-4):387–401, 1995.

[22] T. J. R. Hughes and J. R. Stewart. A space–time formulation for multiscale phenomena. *Journal of Computational and Applied Mathematics*, 74(1-2):217–229, 1996.

[23] T. J. R. Hughes, L. Mazzei, and K. E. Jansen. Large Eddy Simulation and the variational multiscale method. *Computing and Visualization in Science*, 3(1-2):47–59, 2000.

[24] E. A. Munts, S. J. Hulshoff, and R. De Borst. A Space-Time Variational Multiscale Discretization for LES. In *34th AIAA Aerospace Sciences Meeting and Exhibit*, Portland, Oregon, 2004.

[25] T. J. R. Hughes, V. M. Calo, and G. Scovazzi. Variational and multiscale methods in turbulence. *Mechanics of the 21st Century*, pages 153–163, 2005.

[26] Y. Bazilevs. *Isogeometric analysis of turbulence and fluid-structure interaction.* PhD thesis, The University of Texas at Austin, 2006.

[27] F. Brezzi, L. P Franca, and A. Russo. Further considerations on residual-free bubbles for advective-diffusive equations. *Computer Methods in Applied Mechanics and Engineering*, 166(1-2):25–33, 1998.

[28] T. J. R. Hughes and G. Sangalli. Variational multiscale analysis: The fine-scale Green's function, projection, optimization, localization, and stabilized methods. *Society for Industrial and Applied Mathematics*, 45(2):539–557, 2007.

[29] F. Brezzi, L. P. Franca, T. J. R. Hughes, and A. Russo. $b = \int g$. *Computer Methods in Applied Mechanics and Engineering*, (145):329–339, 1997.

[30] J. Donéa and A. Huerta. *Finite element methods for flow problems.* John Wiley & Sons, Ltd, Hoboken, New Jersey, 2003.

[31] A. N. Brooks and T. J. R. Hughes. Streamline upwind/Petrov–Galerkin formulations for convection dominated flows with particular emphasis on the incompressible Navier–Stokes equations. *Computer Methods in Applied Mechanics and Engineering*, 32(1-3):199–259, 1982.

[32] T. J. R. Hughes, L. P. Franca, and G. M. Hulbert. A new finite element formulation for computational fluid dynamics: VIII. The Galerkin/least–squares method for advective–diffusive equations. *Computer Methods in Applied Mechanics and Engineering*, 73(2):173–189, 1989.

[33] T. E. Tezduyar. Stabilized Finite Element Formulations for Incompressible Flow Computations. *Advances in Applied Mechanics*, 28(C):1–44, 1991.

[34] T. E Tezduyar and Y. Osawa. Finite element stabilization parameters computed from element matrices and vectors. *Computer Methods in Applied Mechanics and Engineering*, 190(3-4):411–430, 2000.

[35] B. M. F. de Veubeke. Displacement and equilibrium models in the finite element method. In O. C. Zienkiewicz and G. S. Holister, editors, *Stress Analysis*, chapter 9, pages 145–197. John Wiley & Sons, Ltd, 1965.

[36] F. Brezzi and A. Russo. Choosing bubbles for advection-diffusion problems. *Mathematical Models and Methods in Applied Sciences*, 4(04):571–587, 1994.

[37] S. S. Collis. The DG/VMS Method for Unified Turbulence Simulation. In *32nd AIAA Fluid Dynamics Conference and Exhibit*, Reston, Virigina, 2002.

[38] S. S. Collis. Discontinuous Galerkin Methods for Turbulence Simulation. In *Studying Turbulence Using Numerical Simulation Databases – IX: Proceedings of the 2002 Summer Program*, Stanford, California, 2002.

[39] S. Ramakrishnan and S. S. Collis. Turbulence Control Simulation Using the Variational Multiscale Method. *AIAA Journal*, 42(4):745–753, 2004.

[40] C. D. Argyropoulos and N. C. Markatos. Recent advances on the numerical modelling of turbulent flows. *Applied Mathematical Modelling*, 39(2):693–732, 2014.

[41] C. Coley and J. A. Evans. Variational Multiscale Modeling with Discontinuous Subscales: Analysis and Application to Scalar Transport. *arXiv preprint arXiv:1705.00082*, 2017.

[42] G. Sangalli. A discontinuous residual-free bubble method for advection-diffusion problems. *Journal of Engineering Mathematics*, 49(2):149–162, 2004.

[43] T. J. R. Hughes, G. Scovazzi, P. B. Bochev, and A. Buffa. A multiscale discontinuous Galerkin method with the computational structure of a continuous Galerkin method. *Computer Methods in Applied Mechanics and Engineering*, 195(19):2761–2787, 2006.

[44] A. Buffa, T. J. R. Hughes, and G. Sangalli. Analysis of a multiscale discontinuous Galerkin method for convection-diffusion problems. *SIAM Journal on Numerical Analysis*, 44(4):1420–1440, 2006.

[45] P. Bochev, T. J. R. Hughes, and G. Scovazzi. A multiscale discontinuous Galerkin method. In *International Conference on Large-Scale Scientific Computing*, pages 84–93. Springer, 2005.

[46] T. J. R. Hughes, J. A. Cottrell, and Y. Bazilevs. Isogeometric analysis: Cad, finite elements, nurbs, exact geometry and mesh refinement. *Computer methods in applied mechanics and engineering*, 194(39):4135–4195, 2005.

[47] D. Arnold, F. Brezzi, B. Cockburn, and D. Marini. Discontinuous Galerkin methods for elliptic problems. In B. Cockburn, G. E. Karniadakis, and C. W. Shu, editors, *Discontinuous Galerkin Methods. Theory, Computation and Applications*, volume 11 of *Lecture Notes in Computational Science and Engineering*, pages 89–101. Springer-Verlag, Berlin, Heidelberg, 2000.

[48] F. Bassi and S. Rebay. A High-Order Accurate Discontinuous Finite Element Method for the Numerical Solution of the Compressible Navier–Stokes Equations. *Journal of Computational Physics*, 131(2):267 – 279, 1997.

[49] F. Brezzi, G. Manzini, D. Marini, P. Pietra, and A. Russo. Discontinuous finite elements for diffusion problems. In F. Brioschi, editor, *Atti Convegno in onore*, pages 197–217, Milan, Italy, 1997.

[50] B. Cockburn and C.-W. Shu. The Local Discontinuous Galerkin Method for Time–Dependent Convection–Diffusion Systems. *SIAM Journal on Numerical Analysis*, 35(6):2440–2463, 1998.

[51] J. Douglas and T. Dupont. Interior penalty procedures for elliptic and parabolic Galerkin methods. *Computing methods in applied sciences*, pages 207–216, 1976.

[52] F. Bassi, S. Rebay, G. Mariotti, S. Pedinotti, and M. Savini. A high-order accurate discontinuous finite element method for inviscid and viscous turbomachinery flows. In R. Decuypere and G. Dibelius, editors, *Proceedings of 2nd European Conference on Turbomachinery, Fluid Dynamics and Thermodynamicst*, pages 99–108, Antwerpen, Belgium, 1997.

[53] C. E. Baumann and J. T. Oden. A discontinuous *hp*-finite element method for convection-diffusion problems. *Computer Methods in Applied Mechanics and Engineering*, 175(3–4):311–341, 1999.

[54] B. Rivière, M. F. Wheeler, and V. Girault. Improved energy estimates for interior penalty, constrained and discontinuous Galerkin methods for elliptic problems. Part I. *Computational Geosciences*, 3(3):337–360, 1999.

[55] I. Babuška and M. Zlámal. Nonconforming elements in the finite element method with penalty. *SIAM Journal of Numerical Analysis*, 10(5):863–875, 1973.

[56] F. Brezzi, G. Manzini, D. Marini, P. Pietra, and A. Russo. Discontinuous Galerkin approximations for elliptic problems. *Numerical Methods for Partial Differential Equations*, 16(4):365–378, 2000.

[57] W. H. Reed and T. R. Hill. Triangular Mesh Methods for the Neutron Transport Equation. *Proceedings of the American Nuclear Society*, 836:1–23, 1973.

[58] J. M. Burgers. A mathematical model illustrating the theory of turbulence. *Advances in applied mechanics*, 1:171–199, 1948.

[59] J. Bec and K. Khanin. Burgers turbulence. *Physics Reports*, 447(1–2):1–66, 2007.

[60] G. G. Stokes. On a difficulty in the theory of sound. *The London, Edinburgh, and Dublin philosophical magazine and journal of science*, 33(223):349–356, 1848.

[61] P. J. Oliver. *Introduction to Partial Differential Equations*. Springer, Berlin, Heidelberg, 1 edition, 2014.

[62] J. D. Cole. On a quasi-linear parabolic equation occurring in aerodynamics. *Quarterly of applied mathematics*, 9(3):225–236, 1951.

[63] E. Hopf. The partial differential equation $u_t + u\,u_x = \mu u_{xx}$. *Communications on Pure and Applied mathematics*, 3(3):201–230, 1950.

[64] A. Tsinober. *An Informal Introduction to Turbulence*, volume 92 of *Fluid Mechanics and Its Applications*. Springer, Berlin, Heidelberg, 2009.

[65] W. H. Press, S. A. Teukolsky, W. T. Vetterling, and B. P. Flannery. *Numerical recipes: the art of scientific computing*. Cambridge University Press, New York, 3rd edition, 2007.

[66] Y. Kaneda, T. Ishihara, M. Yokokawa, K. Itakura, and A. Uno. Energy dissipation rate and energy spectrum in high resolution direct numerical simulations of turbulence in a periodic box. *Physics of Fluids*, 15(2):L21–L24, 2003.

[67] S. Hoyas and J. Jiménez. Scaling of the velocity fluctuations in turbulent channels up to Re_τ=2003. *Physics of Fluids*, 18(1):011702, 2005.

[68] M. Lee, N. Malaya, and R. D. Moser. Petascale direct numerical simulation of turbulent channel flow on up to 786K cores. *Proceedings of the International Conference for High Performance Computing, Networking, Storage and Analysis*, 13(61):1–11, 2013.

[69] A. N. Kolmogorov. Local structure of turbulence in an incompressible fluid at very high Reynolds number. *Doklady Akademiia Nauk SSSR*, 30:301–305, 1941.

[70] A. N. Kolmogorov. Dissipation of Energy in the Locally Isotropic Turbulence. *Proceedings: Mathematical and Physical Sciences*, 434(1890):15–17, 1941.

[71] S. J. Hulshoff. Implicit subgrid-scale models in space-time variational-multiscale discretizations. *International Journal for Numerical Methods in Fluids*, 47(10-11):1093–1099, 2004.

[72] R. Codina, J. Principe, O. Guasch, and S. Badia. Time dependent subscales in the stabilized finite element approximation of incompressible flow problems. *Computer Methods in Applied Mechanics and Engineering*, 196(21):2413–2430, 2007.

[73] M.-C. Hsu, I. Akkerman, and Y. Bazilevs. Wind turbine aerodynamics using ALE–VMS: validation and the role of weakly enforced boundary conditions. *Computational Mechanics*, 50(4):499–511, 2012.

[74] J. A. Cottrell, T. J. R. Hughes, and Y. Bazilevs. *Isogeometric analysis: toward integration of CAD and FEA*. John Wiley & Sons, 1st edition, 2009.

[75] D. Schillinger, I. Harari, M.-C. Hsu, D. Kamensky, S. K. F. Stoter, Y. Yu, and Y. Zhao. The non-symmetric Nitsche method for the parameter-free imposition of weak boundary and coupling conditions in immersed finite elements. *Computer Methods in Applied Mechanics and Engineering*, 309:625–652, 2016.

[76] F. Xu, D. Schillinger, D. Kamensky, V. Varduhn, C. Wang, and M.-C. Hsu. The tetrahedral finite cell method for fluids: Immersogeometric analysis of turbulent flow around complex geometries. *Computers & Fluids*, 2015.

[77] P. A. Raviart and J. M. Thomas. A mixed finite element method for second order elliptic problems. In *Proceedings of Symposia in Mathematical Aspects of the Finite Element Method (Rome, 1975)*, volume 606 of *Lecture Notes in Math*, pages 292–315. Springer-Verlag, Berlin, Germany, 1977.

Appendix A

Volumetric fine scale model from Green's functions

The fine scale equation can be written in a form that introduces the residual of the coarse scale solution as a forcing term:

$$\left(w', \mathscr{L}u'\right)_K = \left(w', f\right)_K - \left(w', \mathscr{L}\bar{u}\right)_K = \left(w', \mathscr{R}\right)_K \tag{A.1}$$

One approach to introduce the Green's function is the following. Define the per element Green's function as:

$$\begin{cases} \mathscr{L}^* g(x,y) = \delta_x & \text{for } y \in K \\ g(x,y) = 0 & \text{for } y \in \partial K \end{cases} \tag{A.2}$$

Note that when $\bar{\mathscr{V}}$ is constructed using linear basis functions, then the boundary conditions ensure that function g lies in the subspace $\mathscr{V}'(0)$. In this particular case the homogeneous boundary conditions 'remove' the coarse scale components from $g \in \mathscr{V}$, which leaves $g \in \mathscr{V}'(0)$, meaning that the classical Green's function *is* the fine scale Green's function. As such the notation will make use of $g(x,y) = g'(x,y)$. It is thus important to realize that the following expressions which use the fine scale Green's function only hold for a linear coarse scale basis.

$$(p, \mathscr{L}q)_K = (\mathscr{L}^* p, q)_K + k(p, q; \partial K) \tag{A.3}$$

The fine scale model is obtained by substituting $p = g'(x,y)$ and $q = u'$ into the general form of Green's identity (A.3). Additionally the definitions of (A.2) are used.

$$\begin{aligned} \left(g'(x,y), \mathscr{L}u'\right)_K &= \left(\mathscr{L}^* g'(x,y), u'\right)_K + k(g'(x,y), u'; \partial K) \\ &= \left(\delta_x, u'\right)_K + k(g'(x,x), u'; \partial K) \\ &= u'(x) + k(g'(x,y), u'; \partial K) \end{aligned} \tag{A.4}$$

Note that the parameter of integration and differentiation in this equation is y.

Finally since $g' \in \mathcal{V}'(0)$ it is a valid candidate for the test function w'. As such the left hand side can be replaced by the result from equation (A.1). Rearranging and writing out the integrals results in

$$u'(x) = \int_K g'(x,y)\, \mathcal{R}_{\bar{u}}\, \mathrm{d}y - k(g'(x,y), u'; \partial K) \tag{A.5}$$

Recall that $k(p, q; \partial K)$ constitutes an integration across the element boundary. In particular for the 1D cases considered in the exploratory numerical experiments the boundary terms can be expanded. Here x_j and x_{j+1} refer to the left and right node of the element.

$$u'(x) = \int_K g'(x,y)\, \mathcal{R}_{\bar{u}}\, \mathrm{d}y - k(g'(x,y), u'; x_j) - k(g'(x,y), u'; x_{j+1}) \tag{A.6}$$

Further simplifications can be made when this (exact) equation for u' is used in the coarse scale equation.

$$(\mathscr{L}^*\bar{w}, u') = \Big(\mathscr{L}^*\bar{w}, \int_K g'(x,y)\, \mathcal{R}_{\bar{u}}\, \mathrm{d}y - k(g'(x,y), u'; x_j) - k(g'(x,y), u'; x_{j+1})\Big)_K \tag{A.7}$$

In the examples that are considered the residual $\mathcal{R}$ is constant due to the use of linear basis functions and constant model parameters. Similarly $\mathscr{L}^*\bar{w}$ is constant, and the boundary values $u'(x_j)$ and $u'(x_{j+1})$ are also not spatially varying. As such these factors can be extracted from their respective integrals, which reduces the integrals to multiplications with average Green's function quantities:

$$(\mathscr{L}^*\bar{w}, \tau\mathcal{R}_{\bar{u}} + \gamma_0 u'(x_j) - \gamma_1 u'(x_{j+1}))_K \tag{A.8}$$

This expression is obtained for the example where $k(g'(x,y), u'; \partial K) = \int_{\partial K} g'_y(x,y) \cdot n\, u'(y)$, which closely corresponds to that obtained for the PDEs investigated later. The average quantities can be obtained according to:

$$\tau = \frac{1}{|K|} \int_K \int_K g'(x,y)\, \mathrm{d}y\, \mathrm{d}x \tag{A.9}$$

$$\gamma = \frac{1}{|K|} \int_K \int_{\partial K} g'_y(x,y)\, \mathrm{d}y\, \mathrm{d}x \tag{A.10}$$

The γ_0 and γ_1 in Eq. (A.8) are obtained from Eq. (A.10) in the 1D case where the surface integral can be split up in the addition of the two nodal values. The form shown in Eq. (A.10) would 'be applicable for a multidimensional problem. In this case u' would not be constant across all of ∂K this would always lead to an approximation.

Diffusion operator

$$\mathscr{L} = -\nu\Delta \qquad \mathscr{L}^* = -\nu\Delta \qquad k(w', u'; \partial K) = -\langle w', \nu n \cdot u'_y \rangle_{\partial K} + \langle w'_y \cdot n, \nu u' \rangle_{\partial K}$$

In the case of linear basis functions $\mathscr{L}^*\bar{w} = 0$. As such there is no contribution from the volumetric fine scale term. When higher order basis functions are used, then the Green's function can no longer be obtained with the method just described. As such the volumetric fine scale term is not considered in the Poisson problem discussed in Section 3.2. However the τ that is used in Section 4.3 is based on relative scaling of its advection, diffusion and reaction components. Therefore the τ and γ based on the diffusion component are still of interest. They are obtained as follows.

The Green's function for a one dimensional diffusion operator is defined according to:

$$\begin{cases} -\nu \dfrac{\mathrm{d}^2}{\mathrm{d}y^2} g(x,y) = \delta_x & \text{for } y \in K_j \quad = (x_j, x_{j+1}) \\ g(x,y) = 0 & \text{for } y \in \partial K_j = \{x_j, x_{j+1}\} \end{cases} \tag{A.11}$$

Integration of the first line yields a step function of step magnitude $-\nu^{-1}$:

$$\frac{\mathrm{d}}{\mathrm{d}x} g(x,y) = \begin{cases} C_1 & \text{when } y < x \\ C_1 - \frac{1}{\nu} & \text{when } y \geq x \end{cases} \tag{A.12}$$

A second integration results in a Green's function that is piecewise linear. The slope is defined according to Eq. (A.12). The following structure also satisfies the boundary conditions.

$$g(x,y) = \begin{cases} g_1(x,y) = C_1 \, (y - x_j) & \text{when } y < x \\ g_2(x,y) = \left(C_1 - \frac{1}{\nu}\right)(y - x_{j+1}) & \text{when } y \geq x \end{cases} \tag{A.13}$$

A discontinuous Green's function would result in Dirac delta distributions after a first derivative. The second derivative would include derivatives of Dirac delta distributions. These do not appear in Eq. (A.11). Therefore the final condition to obtain C_1 is based on the required continuity of $g(x,y)$:

$$g_2(x,x) = g_1(x,x) = C_1 \, (x - x_j) = (C_1 - \nu^{-1})(x - x_{j+1}) \tag{A.14}$$

$$\Rightarrow \; C_1 = -\frac{1}{\nu} \frac{x - x_{j+1}}{x_{j+1} - x_j} \tag{A.15}$$

After simplification the Green's function for a Diffusion operator becomes:

$$g(x,y) = \begin{cases} g_1(x,y) = -\frac{1}{\nu} \left(\frac{x - x_{j+1}}{x_{j+1} - x_j}\right) (y - x_j) & \text{when } y < x \\ g_2(x,y) = -\frac{1}{\nu} \left(\frac{x - x_j}{x_{j+1} - x_j}\right) (y - x_{j+1}) & \text{when } y \geq x \end{cases} \tag{A.16}$$

The averaged quantity τ is obtained from its definition Eq. (A.9). To simplify the integration the domain of the PDE is translated to the origin. Thereby x_j and x_{j+1} are replaced by 0 and h respectively.

$$\begin{aligned}
\tau &= \frac{1}{h}\int_0^h\int_0^h g(x,y)\,\mathrm{d}x\,\mathrm{d}y = \frac{1}{h}\int_0^h\int_0^x g_1(x,y)\,\mathrm{d}y\,\mathrm{d}x + \frac{1}{h}\int_0^h\int_x^h g_2(x,y)\,\mathrm{d}y\,\mathrm{d}x \\
&= -\frac{1}{h\nu}\int_0^h\int_0^x \left(\frac{x}{h}-1\right) y\,\mathrm{d}y\,\mathrm{d}x - \frac{1}{h\nu}\int_0^h\int_x^h \frac{x}{h}\,(y-h)\,\mathrm{d}y\,\mathrm{d}x \\
&= -\frac{1}{h\nu}\int_0^h \left(\frac{x}{h}-1\right)\,\frac{1}{2}x^2\,\mathrm{d}x - \frac{1}{h\nu}\int_0^h \frac{x}{h}\,(-\frac{1}{2}x^2 - \frac{1}{2}h^2 + hx)\,\mathrm{d}x \\
&= -\frac{1}{h\nu}\int_0^h \left(\frac{x^2}{2} - \frac{x\,h}{2}\right)\,\mathrm{d}x = -\frac{1}{h\nu}\left(\frac{h^3}{6} - \frac{h^3}{4}\right) = \frac{h^2}{12\nu}
\end{aligned} \tag{A.17}$$

The γ values are obtained according to Eq. (A.10). The integrals along ∂K can be split up in the two point-values at the element boundary $y = 0$ and $y = h$. The two associated γ values become:

$$\begin{aligned}
\gamma_0 &= \frac{1}{h}\int_0^h \frac{\mathrm{d}}{\mathrm{d}y}g(x,y)\Big|_{y=0}\,\mathrm{d}x = \frac{1}{h}\int_0^h \frac{\mathrm{d}}{\mathrm{d}y}g_1(x,y)\Big|_{y=0}\,\mathrm{d}x = -\frac{1}{\nu h}\int_0^h \left(\frac{x}{h}-1\right)\,\mathrm{d}x \;\; = \frac{1}{2\nu} \\
\gamma_1 &= \frac{1}{h}\int_0^h \frac{\mathrm{d}}{\mathrm{d}y}g(x,y)\Big|_{y=h}\,\mathrm{d}x = \frac{1}{h}\int_0^h \frac{\mathrm{d}}{\mathrm{d}y}g_2(x,y)\Big|_{y=h}\,\mathrm{d}x = \quad -\frac{1}{\nu h}\int_0^h \frac{x}{h}\,\mathrm{d}x \quad = -\frac{1}{2\nu}
\end{aligned} \tag{A.18}$$

Reaction operator

$$\mathscr{L} = s \qquad \mathscr{L}^* = s \qquad k(w',u';\partial K) = 0$$

The second contribution to the Burgers equation's fine scale problem is the reactive component. This component does not include any differential operators, but a corresponding τ may still be computed. First obtain the Green's problem as:

$$\begin{cases} s\,g(x,y) = \delta_x & \text{for } y \in K_j \;\; = (x_j, x_{j+1}) \\ g(x,y) = 0 & \text{for } y \in \partial K_j = \{x_j, x_{j+1}\} \end{cases} \tag{A.19}$$

Which has the simple solution

$$g(x,y) = \frac{1}{s}\delta_x \tag{A.20}$$

Then τ is obtained by double integration according to:

$$\tau = \frac{1}{h}\int_0^h \int_0^h \frac{1}{s}\delta_x = \frac{1}{h}\int_0^h \frac{1}{s} = \frac{1}{s} \tag{A.21}$$

Since $g(x,y)$ is independent of y, and thereby $g_y(x,y) = 0$, it follows that:

$$\gamma_0 = 0 \tag{A.22}$$

$$\gamma_1 = 0 \tag{A.23}$$

Advection operator

$$\mathscr{L} = a \cdot \nabla \qquad \mathscr{L}^* = -a \cdot \nabla \qquad k(w', u'; \partial K) = \langle w', a \cdot n u' \rangle_{\partial K}$$

The final component of the fine scale problem of the Burgers equation is an advection operator. Note that a pure advection problem only has a single boundary condition, so the Greens problem has to be restricted to:

$$\begin{cases} -a\dfrac{\mathrm{d}}{\mathrm{d}y}g(x,y) = \delta_x & \text{for } y \in K_j \quad = (x_j, x_{j+1}) \\ g(x,x_j) = 0 \quad \text{or} \quad g(x,x_{j+1}) = 0 \end{cases} \tag{A.24}$$

Integration of the first line in this set of equations yields the Greens function:

$$g(x,y) = \begin{cases} C_1 & \text{when } y < x \\ C_1 - \dfrac{1}{a} & \text{when } y \geq x \end{cases} \tag{A.25}$$

The obtained τ value is anticipated to be positive. A negative value would 'remove' the forcing from the solution field. The advection operator adds the forcing contribution (in upwind direction) instead. A positive τ is obtained when the boundary condition of Eq. (A.24) is satisfied on the right side. Therefore $C_1 = 1/a$ and:

$$g(x,y) = \begin{cases} \dfrac{1}{a} & \text{when } y < x \\ 0 & \text{when } y \geq x \end{cases} \tag{A.26}$$

Finally τ is obtained according to:

$$\tau = \frac{1}{h}\int_0^h \int_0^x \frac{1}{a}\,\mathrm{d}y\,\mathrm{d}x = \frac{1}{h}\int_0^h \frac{x}{a}\,\mathrm{d}x = \frac{h}{2a} \tag{A.27}$$

The temporal differential operator $\frac{\mathrm{d}}{\mathrm{d}t}$ can be viewed as an advective operator with advection speed 1. The τ expression changes slightly. The weak formulation employed in Chapter 4 makes use of a 1D finite element mesh in space, and a finite difference scheme in time. Since τ is an *element* average the factor $\frac{1}{|K|}$ remains $\frac{1}{h}$. However the x-coordinate in the Green's function runs from t^n to t^{n+1}, or when translated from 0 to Δt. This is thus the domain of integration. As such:

$$\tau = \frac{1}{h}\int_0^{\Delta t}\int_0^{x} 1 = \frac{1}{h}\int_0^{\Delta t} x = \frac{\Delta t^2}{2h} \tag{A.28}$$

Since this Green's function is piecewise constant the derivative with respect to y is zero. Therefore the γ integrals vanish.

$$\gamma_0 = 0 \tag{A.29}$$

$$\gamma_1 = 0 \tag{A.30}$$

The next problem under consideration is the advection-diffusion problem. The τ obtained for that problem is determined in Eq. (A.46). As is to be expected Eq. (A.27) is equivalent to Eq. (A.46) in the advection dominated case; when ν approaches zero.

Advection-diffusion problem

$$\mathscr{L} = a\cdot\nabla - \nu\Delta \qquad \mathscr{L}^* = -a\cdot\nabla - \nu\Delta$$

$$k(w',u';\partial K) = \langle w', a\cdot n u'\rangle_{\partial K} - \langle w', \nu n\cdot u'_y\rangle_{\partial K} + \langle n\cdot w'_y, \nu u'\rangle_{\partial K}$$

Section 3.3 focuses on an Advection-Diffusion problem. Recall that $w' \in \mathscr{V}'(0)$ which means that $k(w',u';\partial K)$ reduces to $\langle n\cdot w'_y, \nu u'\rangle_{\partial K}$. For linear basis functions the volumetric fine scale component may be treated as shown in Eq. (A.8), however it now requires an additional multiplication by ν for both γ terms.

First the Green's function is obtained. It is split into two components:

$$g(x,y) = \begin{cases} g_1(x,y) & \text{when } y < x \\ g_2(x,y) & \text{when } y \geq x \end{cases} \tag{A.31}$$

By definition $\mathscr{L}^* g(x,y) = \delta_x$, and as such

$$\mathscr{L}^* g_1(x,y) = -a\frac{\mathrm{d}}{\mathrm{d}y}g_1(x,y) - \nu\frac{\mathrm{d}^2}{\mathrm{d}y^2}g_1(x,y) = 0 \qquad \text{when } y < x \tag{A.32}$$

$$\mathscr{L}^* g_2(x,y) = -a\frac{\mathrm{d}}{\mathrm{d}y}g_2(x,y) - \nu\frac{\mathrm{d}^2}{\mathrm{d}y^2}g_2(x,y) = 0 \qquad \text{when } y > x \tag{A.33}$$

Both sections of the Green's functions are thus of the form

$$g_1(x,y) = C_1 e^{-\frac{a}{\nu}y} + D_1 \tag{A.34}$$
$$g_2(x,y) = C_2 e^{-\frac{a}{\nu}y} + D_2 \tag{A.35}$$

Condition 1 & 2: The boundary condition of Eq. (A.2) sets the Green's function to zero on the element boundary.

$$g_1(x,x_j) \quad = C_1 e^{-\frac{a}{\nu}x_j} + D_1 \quad = 0 \quad \Rightarrow \quad D_1 = -C_1 e^{-\frac{a}{\nu}x_j} \tag{A.36}$$
$$g_2(x,x_{j+1}) = C_2 e^{-\frac{a}{\nu}x_{j+1}} + D_2 = 0 \quad \Rightarrow \quad D_2 = -C_2 e^{-\frac{a}{\nu}x_{j+1}} \tag{A.37}$$

Condition 3: The Green's function must be continuous, else the second derivatives in the differential operator would lead to derivatives of Dirac delta distributions rather than plain Dirac delta distributions. Continuity of $g(x,y)$ requires:

$$g_1(x,x) = C_1\left(e^{-\frac{a}{\nu}x} - e^{-\frac{a}{\nu}x_j}\right) = g_2(x,x) = C_2\left(e^{-\frac{a}{\nu}x} - e^{-\frac{a}{\nu}x_{j+1}}\right) \tag{A.38}$$
$$\Rightarrow C_2 = C_1 \frac{e^{-\frac{a}{\nu}x} - e^{-\frac{a}{\nu}x_j}}{e^{-\frac{a}{\nu}x} - e^{-\frac{a}{\nu}x_{j+1}}} \tag{A.39}$$

Condition 4: The final condition is obtained from the following Dirac delta distribution property:

$$\int_{x\uparrow}^{x\downarrow} \mathscr{L}^* g(x,y)\,\mathrm{d}y = \int_{x\uparrow}^{x\downarrow} \delta_x = 1 \tag{A.40}$$

$$-a g(x,y)\Big|_{x\uparrow}^{x\downarrow} - \nu \frac{\mathrm{d}}{\mathrm{d}y} g(x,y)\Big|_{x\uparrow}^{x\downarrow} = \nu \frac{\mathrm{d}}{\mathrm{d}y} g_1(x,y)\Big|_x - \nu \frac{\mathrm{d}}{\mathrm{d}y} g_2(x,y)\Big|_x = 1 \tag{A.41}$$

The first term in the leftmost side of Eq. (A.41) cancels due to the continuity condition. This results in:

$$-aC_1 e^{-\frac{a}{\nu}x} + aC_2 e^{-\frac{a}{\nu}x} = 1 \tag{A.42}$$

Combining relations (A.39) and (A.42) yields the following expression for the Green's function:

$$g(x,y) = \begin{cases} g_1(x,y) = \dfrac{b}{k-1}\left(e^{-\frac{a}{\nu}y} - e^{-\frac{a}{\nu}x_j}\right) & \text{when } y < x \\ g_2(x,y) = \dfrac{k\,b}{k-1}\left(e^{-\frac{a}{\nu}y} - e^{-\frac{a}{\nu}x_{j+1}}\right) & \text{when } y \geq x \end{cases} \tag{A.43}$$

$$k = \frac{e^{-\frac{a}{\nu}x} - e^{-\frac{a}{\nu}x_j}}{e^{-\frac{a}{\nu}x} - e^{-\frac{a}{\nu}x_{j+1}}} \tag{A.44}$$

$$b = \frac{1}{a} e^{\frac{a}{\nu}x} \tag{A.45}$$

Finally this Green's function is used to obtain the per-element constants τ, γ_0 and γ_1. A single expression for these integral quantities can be obtained by translating the element such that $x_j = 0$ and $x_{j+1} = h$. With the aid of definitions (A.9) and (A.10) the following equations are obtained.

$$\begin{aligned}
\tau &= \frac{1}{h}\int_0^h\int_0^h g'(x,y)\,\mathrm{d}x\,\mathrm{d}y = \frac{1}{h}\int_0^h\left[\int_0^x g_1(x,y)\,\mathrm{d}y + \int_x^h g_2(x,y)\,\mathrm{d}y\right]\mathrm{d}x = \frac{h}{2\,a} - \frac{\nu}{a^2} + \frac{h}{a\left(e^{\frac{a}{\nu}h}-1\right)} \\
\gamma_0 &= \frac{1}{h}\int_0^h g'_y(x,0)\,\mathrm{d}x = \frac{1}{h}\int_0^h g_{1,y}(x,0)\,\mathrm{d}x = -\frac{1}{h}\int_0^h \frac{a}{\nu}\frac{b}{k-1}\,\mathrm{d}x \qquad = \frac{\nu - a\,h - \nu e^{-\frac{a}{\nu}h}}{a\,h\,\nu\left(e^{-\frac{a}{\nu}h}-1\right)} \\
\gamma_1 &= \frac{1}{h}\int_0^h g'_y(x,h)\,\mathrm{d}x = \frac{1}{h}\int_0^h g_{2,y}(x,h)\,\mathrm{d}x = -\frac{1}{h}\int_0^h \frac{a}{\nu}\frac{k\,b}{k-1}e^{-\frac{a}{\nu}h}\,\mathrm{d}x = \frac{\nu + a\,h - \nu e^{\frac{a}{\nu}h}}{a\,h\,\nu\left(e^{\frac{a}{\nu}h}-1\right)}
\end{aligned} \tag{A.46}$$

These integrations have been verified using `Matlab`'s symbolic math toolbox.

Appendix B

Classical derivation of discontinuous Galerkin formulations for second order elliptic problems

A primary objective of this report has been to proposes a new point of view for deriving discontinuous Galerkin formulations. To fully appreciate the simplicity and consistence of the framework described in Chapter 3 (in particular its application in Section 3.2), this appendix will provide the classical approach for obtaining the discontinuous Galerkin formulation of a Poisson problem. Different choices of parameters and 'numerical traces' in this derivation result in the different DG formulations collected in Table 3.2. This table is repeated in this appendix for ease of reference; Table B.2.

In the standard continuous Galerkin method the derivative of the finite element solution is discontinuous across elements. Yet in many physical problems involving Laplace operators it is the first derivative quantity that is of interest. Examples are the stress and strain in mechanical problems and the heat flux in heat transfer problems. The mixed-method formulation of the Poisson problem was introduced in the 1960s. Researchers aimed to describe the gradient field by a continuous approximation basis such that it remains well defined on element interfaces. The mixed formulation of the Poisson problem is:

$$\begin{cases} q = \nabla u & \text{in } \Omega \subset \mathbb{R}^d \\ -\nabla \cdot q = f & \text{in } \Omega \\ u = u_D & \text{on } \partial\Omega \subset \mathbb{R}^{(d-1)} \end{cases} \tag{B.1}$$

Where u is the classical state variable, with Dirichlet boundary conditions u_D, and q is the newly introduced flux state variable. This problem is defined on an d-dimensional domain Ω.

The proposed corresponding weak formulation is,

Find $q, u \in V \times W$ s.t.:

$$\begin{cases} (v,q)_\Omega + (\nabla \cdot v, u)_\Omega = \langle v, n \cdot u_D \rangle_{\partial\Omega} & \forall\, v \in V = H(\mathrm{div}, \Omega) \\ -(w, \nabla \cdot q)_\Omega = (w,f)_\Omega & \forall\, w \in W = L^2(\Omega) \end{cases} \tag{B.2}$$

As such the weak formulation consists of two trial functions and two test functions. This formulation is still defined on the complete domain Ω. As such the divergence of q and v must be integrable on the entire domain. This is captured in the $V = H(\mathrm{div}, \Omega)$ space definition, which effectively imposes a certain continuity condition on V. More specifically it is defined as:

$$V = H(\mathrm{div}, \Omega) = \left\{ v \in \left[L^2(\Omega) \right]^d : \nabla \cdot v \in L^2(\Omega) \right\} \tag{B.3}$$

In turn the discretized form of this weak formulations is defined as follows.

Find $q_h, u_h \in V_h \times W_h$ s.t.:

$$\begin{cases} (v,q_h)_\Omega + (\nabla \cdot v, u_h)_\Omega = \langle v, n \cdot u_D \rangle_{\partial\Omega} & \forall\, v \in V_h \subset V \\ -(w, \nabla \cdot q_h)_\Omega = (w,f)_\Omega & \forall\, w \in W_h \subset W \end{cases} \tag{B.4}$$

To prove existence and uniqueness of the solutions q_h and u_h it is required that $\nabla \cdot V_h \supset W_h$. This condition, combined with the condition $V_h \subset H(\mathrm{div}, \Omega)$, has the consequence that the basis functions for the construction of V_h are quite complex. The typical set of basis functions that is used for this type of problem is the Raviant-Thomas basis, introduced in [77].

While the basis functions for V_h are somewhat constrained, the basis functions of W_h are remarkably free of restrictions. No global continuity is required for W_h, which means that the basis functions can be discontinuous across elements. Arbitrary polynomial orders can be used on separate elements, and the element vertices do not need to coincide. This is very different from classical finite element derivations, which require $u_h \in H^1(\Omega)$, and thus $u_h \in \mathscr{C}^0$. The inherent freedom of the approximation space for u_h in the mixed method formulations inspired researchers to use this framework as a basis for discontinuous Galerkin formulations.

To mitigate the continuity requirements of V_h, the weak formulation is defined per element. The discontinuous function space $\mathscr{V}$ is introduced. For the exact solution this becomes:

$$\begin{cases} (v,q)_K + (\nabla \cdot v, u)_K = \langle v, n \cdot u \rangle_{\partial K} & \forall\, K \in \mathscr{T} \quad \forall\, v \in \mathscr{V} \in L^2(\Omega) \\ (\nabla w, q)_K - \langle w, n \cdot q \rangle_{\partial K} = (w,f)_K & \forall\, K \in \mathscr{T} \quad \forall\, w \in W \end{cases} \tag{B.5}$$

With $u = u_D$ on $\partial\Omega$. This weak form is discretized to obtain:

Find $q_h, u_h \in \mathscr{V}_h \times W_h$ s.t.:

$$\begin{cases} (v,q_h)_K + (\nabla \cdot v, u_h)_K = \langle v, n \cdot \hat{u}_h \rangle_{\partial K} & \forall\, K \in \mathscr{T} \quad \forall\, v \in \mathscr{V}_h \\ (\nabla w, q_h)_K - \langle w, n \cdot \hat{q}_h \rangle_{\partial K} = (w,f)_K & \forall\, K \in \mathscr{T} \quad \forall\, w \in W_h \end{cases} \tag{B.6}$$

Where $\hat{u}_h = u_D$ on $\partial\Omega$. The newly introduced parameters $\hat{u}_h$ and $\hat{q}_h$ are called the numerical

traces. They are approximations to u and q on element interfaces. Choice of their definition determines key properties of the method, such as existence/uniqueness, stability, accuracy, consistence and local conservation behavior. Potential choices of the numerical traces will be discussed shortly.

At this stage both spaces $\mathcal{V}$ and W_h do no longer require any form of global continuity. The discontinuous Galerkin method has taken shape. Specifically these spaces are defined according to Eqs. (B.7) and (B.8).

$$\mathcal{V}_h = \left\{ v \in L^2(\Omega) \ : v \in [H(\mathrm{div}, K)]^d \ , \ v\big|_K \in P^m(K) \ \forall K \in \mathcal{T} \right\} \tag{B.7}$$

$$W_h = \left\{ w \in L^2(\Omega) : w\big|_K \in P^n(K) \ \forall K \in \mathcal{T} \right\} \tag{B.8}$$

Note that in principle the polynomial orders m and n could be different for each element.

A global weak formulation is obtained by summing Eq. (B.6) for each element in the mesh. This summation can be performed without loss of generality since the test functions can vary independently per element. By using the identity $(pq)^+ + (pq)^- = \{\!\{p\}\!\}[\![q]\!] + [\![p]\!]\{\!\{q\}\!\}$ we obtain:

Find $q_h, u_h \in \mathcal{V}_h \times W_h$ s.t.:

$$\begin{cases} (v, q_h)_{\Omega_E} + (\nabla \cdot v, u_h)_{\Omega_E} - \langle [\![v]\!], \{\!\{\hat{u}_h\}\!\} \rangle_\Gamma - \langle \{\!\{v\}\!\}, [\![\hat{u}_h]\!] \rangle_\Gamma = \langle v, n \cdot u_D \rangle_{\partial\Omega} & \forall\, v \in \mathcal{V}_h \\ (\nabla w, q_h)_{\Omega_E} - \langle [\![w]\!], \{\!\{\hat{q}_h\}\!\} \rangle_\Gamma - \langle \{\!\{w\}\!\}, [\![\hat{q}_h]\!] \rangle_\Gamma - \langle w, \hat{q}_h \rangle_{\partial\Omega} = (w, f)_{\Omega_E} & \forall\, w \in W_h \end{cases} \tag{B.9}$$

When this new weak formulation is compared to Eq. (B.4) one can observe that the newly introduced terms are effectively taking into account the Dirac layers that would exist between elements when a discontinuous test and trial function would be used in Eq. (B.4).

At this stage the choice of numerical traces is introduced. The consistence and conservativity of the method depends on their definition. A *consistent* scheme satisfies the weak discretized formulation also for the exact solution, i.e. when $u_h := u$, $q_h := \nabla u$ is substituted into the weak forms. In this case Galerkin orthogonality holds, which is a key requirement for error analysis and for achieving optimum convergence rates. Consistent schemes can be constructed by making sure that the numerical traces equal the exact value when the finite element solution is the exact solution, i.e. $\hat{q}_h = \nabla u$ and $\hat{u}_h = u$ when $u_h := u$ and $q_h := \nabla u$. *Conservative* schemes satisfy the property of Eq. (B.10) for any $\hat{K}$, which is an arbitrary union of elements. This property holds when $\hat{q}_h$ is single-valued on element interfaces, i.e. $\hat{q}_h(\lim_{\epsilon \to 0} x - \epsilon) = \hat{q}_h(\lim_{\epsilon \to 0} x + \epsilon)$.

$$\int_{\hat{K}} f + \int_{\partial \hat{K}} \hat{q}_h \cdot n = 0 \tag{B.10}$$

A classical form of both traces is provided in Eq. (B.11). The parameters C_{ij} are per-facet constants. This choice is favorable since it depends linearly on the existing variables u_h and q_h. It results in both consistent and conservative numerical schemes. The original Bassi-Rebay method and the Local DG (LDG) method use numerical traces of this form (refer to Table B.1 for their exact definition). Additionally every known form of the Hybridizable DG

(HDG) method employs these types of traces [14].

$$\begin{aligned}\hat{q}_h &= \{\!\{q_h\}\!\} + C_{11}[\![u_h]\!] + \mathbf{C}_{12}[\![q_h]\!] \\ \hat{u}_h &= \{\!\{u_h\}\!\} + \mathbf{C}_{21}\cdot[\![u_h]\!] + C_{22}[\![q_h]\!]\end{aligned} \tag{B.11}$$

To ensure existence and uniqueness of the DG solution it is required that $\mathbf{C}_{12} + \mathbf{C}_{21} = 0$ and $C_{11}, C_{22} \leq 0$. Additionally it is required that $\mathcal{V}_h(K) \supset \nabla W_h(K)$ for each element in the mesh. These conditions are rather straightforward to derive, but not particularly relevant for the current appendix. Therefore their derivation is left to [11, 14, 47].

The numerical traces in Eq. (B.11) include terms that depend on both states variables u_h and q_h. This means they inherently require mixed-method type implementations. A different choice of $\hat{q}_h$ is provided in Eq. (B.12). This definition purely depends on the solution field u_h. As such the mixed-method can be collapsed into a single weak formulation. The interior penalty method, the nonsymmetric interior penalty Galerkin (NIPG) method and the Baumann-Oden method employ numerical traces of this form. These methods are consistent and conservative.

$$\hat{q}_h = \{\!\{\nabla u_h\}\!\} + C_{11}[\![u_h]\!] + \mathbf{C}_{12}[\![\nabla u_h]\!] \tag{B.12}$$

The traces in Eqs. (B.11) and (B.11) are all single valued. The Babuška-Zlámal method and Brezzi *et al.*'s second method use a non-single-valued construction of $\hat{u}_h$, namely Eq. (B.13). These methods are conservative since their choice of $\hat{q}_h$ is single-valued on element interfaces. However their choice of $\hat{q}_h$ renders the methods non-consistent. See Table B.1.

$$\hat{u}_h(\lim_{\epsilon\to 0} x \pm \epsilon) = u_h(\lim_{\epsilon\to 0} x \pm \epsilon) \tag{B.13}$$

Finally Bassi *et al.*'s method and Brezzi *et al.*'s first and second method can be retrieved by adding a slightly more complex term to the numerical trace $\hat{q}_h$ of either Eq. (B.11) or Eq. (B.12). This term is the following functional.

$$-\eta\,\{\!\{r_e([\![u_h]\!])\}\!\} \quad \text{where } r_e([\![u_h]\!]) \text{ satisfies} \quad \int_\Omega r_e([\![u_h]\!])\cdot\tau = \int_{\partial\Omega} [\![u_h]\!]\cdot\{\!\{\tau\}\!\} \quad \forall\,\tau\in\mathcal{V}_h \tag{B.14}$$

While many DG formulations are implemented in their mixed format, the analysis performed in Section 3.2 derives a single-line weak formulation. This is called the 'primal form'. Much of the body of article [11] is devoted to obtaining the primal form of the methods in Table B.2. Forcing the mixed-formulation into a single-line primal form often results in the so-called lifting operators. These are functionals of the form shown in Eq. (B.14). They are purely introduced for the purpose of mathematical analysis. They have little use from a numerical implementation point of view. Hence it is difficult to find the fine scale model associated to these DG formulations. As such one of the suggestions for further research proposed in the conclusion of this thesis is to investigate the DG-RVMS framework in a mixed-method setting.

That being said, some of the methods in Table 3.2 do not include these lifting operators (e.g. the IP method, the Baumann-Oden method and the NIPG method). These are exactly the methods that use a $\hat{q}_h$ of the form of Eq. (B.12). This form of $\hat{q}_h$ omits the variable

q_h altogether. These are thus not fundamentally mixed methods. The general strategy of obtaining the primal form of the mixed formulation is the following.

Integration by parts is performed on term $(\nabla \cdot v, u_h)_{\Omega_E}$ in the first line of Eq. (B.9). Rewriting yields the formulation:

$$\begin{aligned}(v, q_h)_{\Omega_E} = (v, \nabla \cdot u_h)_{\Omega_E} + \langle [\![v]\!], \{\!\{ \hat{u}_h - u_h \}\!\} \rangle_\Gamma + \\ \langle \{\!\{ v \}\!\}, [\![\hat{u}_h - u_h]\!] \rangle_\Gamma + \langle v, n \cdot u_D \rangle_{\partial\Omega} \quad \forall\, v \in \mathscr{V}_h\end{aligned} \tag{B.15}$$

Since this must hold for any $v \in \mathscr{V}_h$, and since $\mathscr{V}_h(K) \supset \nabla W_h(K)$, one could take $v := \nabla w$. The resulting relation can be substituted into the second line of Eq. (B.9). The general form of the DG formulations for Poisson problems is obtained:

$$\begin{aligned}&(\nabla w, \nabla \cdot u_h)_{\Omega_E} + \langle [\![\nabla w]\!], \{\!\{ \hat{u}_h \}\!\} - \{\!\{ u_h \}\!\} \rangle_\Gamma + \langle \{\!\{ \nabla w \}\!\}, [\![\hat{u}_h]\!] - [\![u_h]\!] \rangle_\Gamma \\ &- \langle [\![w]\!], \{\!\{ \hat{q}_h \}\!\} \rangle_\Gamma - \langle \{\!\{ w \}\!\}, [\![\hat{q}_h]\!] \rangle_\Gamma - \langle w, \hat{q}_h \rangle_{\partial\Omega} = (w, f)_{\Omega_E} - \langle w, n \cdot u_D \rangle_{\partial\Omega} \qquad \forall\, w \in W_h\end{aligned} \tag{B.16}$$

Equation (B.16) imposes the Dirichlet boundary condition weakly. Alternatively one could choose to satisfy these strongly by including them in the definition of the function space W_h. This would result in the following form.

$$W_h(g) = \left\{ w \in L^2(\Omega) : w\big|_K \in P^n(K) \;\; \forall\, K \in \mathscr{T}, w = g \text{ on } \partial\Omega \right\} \tag{B.17}$$

Find $u_h \in W_h(u_D)$ s.t.:

$$\begin{aligned}&(\nabla w, \nabla \cdot u_h)_{\Omega_E} + \langle [\![\nabla w]\!], \{\!\{ \hat{u}_h \}\!\} - \{\!\{ u_h \}\!\} \rangle_\Gamma + \langle \{\!\{ \nabla w \}\!\}, [\![\hat{u}_h]\!] - [\![u_h]\!] \rangle_\Gamma \\ &\qquad - \langle [\![w]\!], \{\!\{ \hat{q}_h \}\!\} \rangle_\Gamma - \langle \{\!\{ w \}\!\}, [\![\hat{q}_h]\!] \rangle_\Gamma = (w, f)_{\Omega_E} \qquad \forall\, w \in W_h(0)\end{aligned} \tag{B.18}$$

The primal formulations provided in Table B.2 can be obtained by substituting the numerical traces from Table B.1 into Eq. (B.18). The methods that are inherently of mixed origin, i.e. those that involve q_h in the trace definitions, result in formulations including lifting operators. The additional information that is discarded by restricting v to ∇w in Eq. (B.15) is retained in the definitions of the lifting operators.

For the sake of completeness it is shown that the primal form of the interior penalty method is obtained from the choices $\hat{u}_h = \{\!\{ u_h \}\!\}$ and $\hat{q}_h = \{\!\{ \nabla u_h \}\!\} - \eta h^{-1} [\![u_h]\!]$. Since these numerical traces are single-valued on element interfaces it follows that $[\![\hat{u}_h]\!] = [\![\hat{q}_h]\!] = 0$, $\{\!\{ \hat{u}_h \}\!\} = \hat{u}_h$ and $\{\!\{ \hat{q}_h \}\!\} = \hat{q}_h$. Therefore:

$$(\nabla w, \nabla \cdot u_h)_{\Omega_E} - \langle \{\!\{ \nabla w \}\!\}, [\![u_h]\!] \rangle_\Gamma - \langle [\![w]\!], \{\!\{ \nabla u_h \}\!\} - \eta h^{-1} \rangle_\Gamma = (w, f)_{\Omega_E} \quad \forall\, w \in W_h \tag{B.19}$$

Which corresponds to its entry in Table B.2.

Table B.1: *Overview of numerical traces used for discontinuous Galerkin formulations of second order elliptic problems. Adapted from [11].*

Method name	$\hat{u}_h(\lim_{\epsilon\to 0} x \pm \epsilon)$	$\hat{q}_h$
Bassi-Rebay [48]	$\{\!\{u_h\}\!\}$	$\{\!\{q_h\}\!\}$
Brezzi *et al.* [49]	$\{\!\{u_h\}\!\}$	$\{\!\{q_h\}\!\} + \eta\,\{\!\{r_e([\![u_h]\!])\}\!\}$
Local DG [50]	$\{\!\{u_h\}\!\} - \beta[\![u_h]\!]$	$\{\!\{q_h\}\!\} + \beta[\![q_h]\!] - \mu[\![u_h]\!]$
Interior penalty [51]	$\{\!\{u_h\}\!\}$	$\{\!\{\nabla u_h\}\!\} - \mu[\![u_h]\!]$
Bassi *et. al* [52]	$\{\!\{u_h\}\!\}$	$\{\!\{\nabla u_h\}\!\} + \eta\,\{\!\{r_e([\![u_h]\!])\}\!\}$
Baumann-Oden [53]	$\{\!\{u_h\}\!\} + n\cdot[\![u_h]\!]$	$\{\!\{\nabla u_h\}\!\}$
NIPG [54]	$\{\!\{u_h\}\!\} + n\cdot[\![u_h]\!]$	$\{\!\{\nabla u_h\}\!\} - \mu[\![u_h]\!]$
Babuška-Zlámal [55]	$u_h(\lim_{\epsilon\to 0} x \pm \epsilon)$	$-\mu[\![u_h]\!]$
Brezzi *et al.* [56]	$u_h(\lim_{\epsilon\to 0} x \pm \epsilon)$	$\eta\,\{\!\{r_e([\![u_h]\!])\}\!\}$

Table B.2: *Copy of Table 3.2. Overview of discontinuous Galerkin formulations for second order elliptic problems. Adapted from [11].*

Method name	**Global weak formulation**
Bassi-Rebay [48]	$(\nabla\bar{w},\nabla\bar{u})_{\Omega_E} - \langle[\![\bar{w}]\!],\{\!\{\nabla\bar{u}\}\!\}\rangle_\Gamma - \langle\{\!\{\nabla\bar{w}\}\!\},[\![\bar{u}]\!]\rangle_\Gamma + \big(r([\![\bar{w}]\!]),r([\![\bar{u}]\!])\big)_{\Omega_E}$
Brezzi *et al.* [49]	$(\nabla\bar{w},\nabla\bar{u})_{\Omega_E} - \langle[\![\bar{w}]\!],\{\!\{\nabla\bar{u}\}\!\}\rangle_\Gamma - \langle\{\!\{\nabla\bar{w}\}\!\},[\![\bar{u}]\!]\rangle_\Gamma + \big(r([\![\bar{w}]\!]),r([\![\bar{u}]\!])\big)_{\Omega_E}$ $-\langle[\![\bar{w}]\!],\mu\,\{\!\{r_e(\bar{u})\}\!\}\rangle_\Gamma$
Local DG [50]	$(\nabla\bar{w},\nabla\bar{u})_{\Omega_E} - \langle[\![\bar{w}]\!],\{\!\{\nabla\bar{u}\}\!\}\rangle_\Gamma - \langle\{\!\{\nabla\bar{w}\}\!\},[\![\bar{u}]\!]\rangle_\Gamma + \langle[\![\bar{w}]\!],\eta\,[\![\bar{u}]\!]\rangle_\Gamma$ $+\langle\beta\cdot[\![\bar{w}]\!],[\![\nabla\bar{u}]\!]\rangle_\Gamma + \langle[\![\nabla\bar{w}]\!],\beta\cdot[\![\bar{u}]\!]\rangle_\Gamma$ $+\big(r([\![\bar{w}]\!]) + l([\![\beta\cdot\bar{w}]\!]),r([\![\bar{u}]\!]) + l([\![\beta\cdot\bar{u}]\!])\big)_{\Omega_E}$
Interior penalty [51]	$(\nabla\bar{w},\nabla\bar{u})_{\Omega_E} - \langle[\![\bar{w}]\!],\{\!\{\nabla\bar{u}\}\!\}\rangle_\Gamma - \langle\{\!\{\nabla\bar{w}\}\!\},[\![\bar{u}]\!]\rangle_\Gamma + \langle[\![\bar{w}]\!],\eta\,[\![\bar{u}]\!]\rangle_\Gamma$
Bassi *et. al* [52]	$(\nabla\bar{w},\nabla\bar{u})_{\Omega_E} - \langle[\![\bar{w}]\!],\{\!\{\nabla\bar{u}\}\!\}\rangle_\Gamma - \langle\{\!\{\nabla\bar{w}\}\!\},[\![\bar{u}]\!]\rangle_\Gamma - \langle[\![\bar{w}]\!],\mu\,\{\!\{r_e(\bar{u})\}\!\}\rangle_\Gamma$
Baumann-Oden [53]	$(\nabla\bar{w},\nabla\bar{u})_{\Omega_E} + \langle[\![\bar{w}]\!],\{\!\{\nabla\bar{u}\}\!\}\rangle_\Gamma - \langle\{\!\{\nabla\bar{w}\}\!\},[\![\bar{u}]\!]\rangle_\Gamma$
NIPG [54]	$(\nabla\bar{w},\nabla\bar{u})_{\Omega_E} + \langle[\![\bar{w}]\!],\{\!\{\nabla\bar{u}\}\!\}\rangle_\Gamma - \langle\{\!\{\nabla\bar{w}\}\!\},[\![\bar{u}]\!]\rangle_\Gamma + \langle[\![\bar{w}]\!],\eta\,[\![\bar{u}]\!]\rangle_\Gamma$
Babuška-Zlámal [55]	$(\nabla\bar{w},\nabla\bar{u})_{\Omega_E} + \langle[\![\bar{w}]\!],\eta\,[\![\bar{u}]\!]\rangle_\Gamma$
Brezzi *et al.* [56]	$(\nabla\bar{w},\nabla\bar{u})_{\Omega_E} - \langle[\![\bar{w}]\!],\mu\,\{\!\{r_e(\bar{u})\}\!\}\rangle_\Gamma$

Appendix C

Global identity to per-term identities of the fine scale terms

In Chapter 3 the implicit fine scale surface models associated to a number of known discontinuous Galerkin formulations is derived. The process equates the exact weak formulation to the classical DG formulation. The identical terms are removed from either side of the equation. This leaves a formulation that captures the fine scale surface model. The terms that involve the same test function operator are individually equated to zero. For example, in the case of the interior penalty method for a Poisson's equation:

$$-\left(\Delta\bar{w}, u'\right)_{\Omega_E} + \left\langle [\![\nabla\bar{w}]\!], \{\!\{u'\}\!\}\right\rangle_\Gamma - \left\langle [\![\bar{w}]\!], \{\!\{\nabla u'\}\!\} + \eta h^{-1}[\![\bar{u}]\!]\right\rangle_\Gamma = 0 \quad \forall\, \bar{w} \in \bar{\mathscr{V}}(0) \tag{C.1}$$

$$\Rightarrow \quad \begin{cases} \left(\Delta\bar{w}, u'\right)_{\Omega_E} = 0 & \forall\, \bar{w} \in \bar{\mathscr{V}}(0) \\ \{\!\{u'\}\!\}\Big|_{\hat{x}} = 0 & \forall\, \hat{x} \in \Gamma \\ \{\!\{\nabla u'\}\!\}\Big|_{\hat{x}} = -\eta h^{-1}[\![\bar{u}]\!]\Big|_{\hat{x}} & \forall\, \hat{x} \in \Gamma \end{cases} \tag{C.2}$$

Recall that the test function must be zero on the domain boundary due to the strong satisfaction of the Dirichlet boundary condition. So by definition Γ is the set of interior interfaces.

The step from Eq. (C.1) to Eq. (C.2) is proven in this appendix. The analysis is restricted to 1D problems. A similar derivation is not possible for multidimensional domains. Extension to such a setting is the focus of Section 3.2.5.

First $\bar{w}$ is chosen to be the continuous piecewise linear function shown in Figure C.1. Within an element the second derivatives are zero, so the first term in Eq. (C.1) is removed from the equation. The jumps of $\bar{w}$ are also zero due to the continuity of the function, and thus also the last term in Eq. (C.1) may be removed. Only at a single element interface the value $[\![\nabla\bar{w}]\!]$ is nonzero, namely the interface with the bend. Clearly a similar test function may be constructed for each element interface. Thereby:

$$\left\langle [\![\nabla\bar{w}]\!], \{\!\{u'\}\!\}\right\rangle_{\hat{x}} = 0 \quad \Rightarrow \quad \{\!\{u'\}\!\}\Big|_{\hat{x}} = 0 \qquad \forall\, \hat{x} \in \Gamma \tag{C.3}$$

Next a test function is chosen that has the shape shown in Figure C.2. Again the second derivative of $\bar{w}$ within an element is zero. Additionally it was just concluded that $\{\!\{u'\}\!\} = 0$ on element interfaces. As such the first and second terms in Eq. (C.1) may be removed. The piecewise linear test function has a jump at some arbitrary element interface. As such:

$$-\langle [\![\bar{w}]\!], \{\!\{\nabla u'\}\!\} + \eta h^{-1} [\![\bar{u}]\!] \rangle_{\hat{x}} = 0 \quad \Rightarrow \quad \{\!\{\nabla u'\}\!\}\Big|_{\hat{x}} = -\eta h^{-1} [\![\bar{u}]\!]\Big|_{\hat{x}} \quad \forall\, \hat{x} \in \Gamma \tag{C.4}$$

When both nodal identities of Eqs. (C.3) and (C.4) are substituted into Eq. (C.1), then the remaining volumetric identity of Eq. (C.2) is obtained. Notice that these identities hold irregardless of mesh topology.

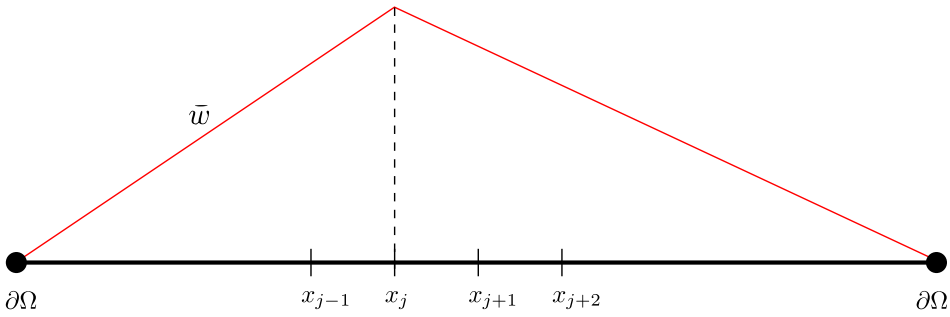

Fig. C.1: *Choice of test function to obtain the* $\{\!\{u'\}\!\}$ *identities.*

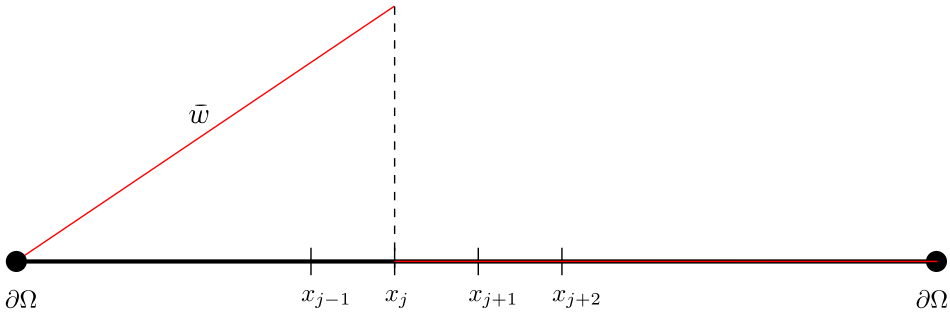

Fig. C.2: *Choice of test function to obtain the* $\{\!\{\nabla u'\}\!\} + \eta h^{-1} [\![\bar{u}]\!]$ *identities.*

Appendix D

Further numerical results for the Burgers equation

An extensive overview of finite element solutions for the Burgers equation is provided in this appendix. All solutions are shown at $t = 8\pi$. These concern the three-scale eddy viscosity model of Section 4.2, the B-spline R-VMS model of Section 4.3 and the DG-RVMS model developed in Section 4.4. Each of the models corresponds to different computational parameters that are provided in the respective section. Recall the weak formulations:

Three-scale eddy viscosity weak formulation

Find $\bar{u}\,, \tilde{u} \in \bar{\mathscr{M}} \times \tilde{\mathscr{M}}$ s.t.:

$$\begin{cases} \big(\bar{w}, \bar{u}_t + \tilde{u}_t\big)_\Omega = \frac{1}{2}\big(\bar{w}_x, (\bar{u} + \tilde{u})^2\big)_\Omega - \big(\bar{w}_x, \nu(\bar{u}_x + \tilde{u}_x)\big)_\Omega + \big(\bar{w}, f\big)_\Omega & \forall\, \bar{w} \in \bar{\mathscr{M}} \\ \big(\tilde{w}, \bar{u}_t + \tilde{u}_t\big)_\Omega = \frac{1}{2}\big(\tilde{w}_x, (\bar{u} + \tilde{u})^2\big)_\Omega - \big(\tilde{w}_x, \nu\, \bar{u}_x\big)_\Omega - \big(\tilde{w}_x, (\nu + \nu_T)\, \tilde{u}_x\big)_\Omega + \big(\tilde{w}, f\big)_\Omega & \forall\, \tilde{w} \in \tilde{\mathscr{M}} \end{cases} \tag{D.1}$$

B-spline residual-based variational multiscale weak formulation

Find $u_h \in \bar{\mathbb{Q}}$ s.t.:

$$\begin{aligned} \big(\bar{w}, u_{ht}\big)_\Omega - \frac{1}{2}\big(\bar{w}_x, u_h^2\big)_\Omega - \big(\bar{w}_x, u_h\, \tau \mathscr{R}_{u_h}\big)_\Omega + \big(\bar{w}_x, \nu u_{hx}\big)_\Omega = \\ \big(\bar{w}_x, f\big)_\Omega + \big(\bar{w}_{xx}, \nu\tau \mathscr{R}_{u_h}\big)_\Omega + \frac{1}{2}\big(\bar{w}_x, (\tau \mathscr{R}_{u_h})^2\big)_\Omega \qquad \forall\, \bar{w} \in \bar{\mathbb{Q}} \end{aligned} \tag{D.2}$$

Discontinuous Galerkin residual-based variational multiscale weak formulation

Find $u_h \in \bar{\mathscr{V}}$ s.t.:

$$\begin{aligned} &\big(\bar{w}, u_{ht}\big)_{\Omega_E} - \frac{1}{2}\big(\bar{w}_x, {u_h}^2\big)_{\Omega_E} - \big(\bar{w}_x, u_h\, \tilde{u}'\big)_{\Omega_E} + \frac{1}{2}\big\langle [\![\bar{w}]\!] \{\!\{ u_h \}\!\}\, u_h(\lim_{\epsilon \to 0} x - \epsilon u_h)\big\rangle_\Gamma \\ &+ \big(\bar{w}_x, \nu u_{hx}\big)_{\Omega_E} - \big\langle [\![\bar{w}]\!], \nu \{\!\{ u_{hx} \}\!\}\big\rangle_\Gamma - \big\langle \{\!\{ \bar{w}_x \}\!\}, \nu [\![u_h]\!]\big\rangle_\Gamma + \big\langle [\![\bar{w}]\!], \eta h^{-1} \nu [\![u_h]\!]\big\rangle_\Gamma \\ &\qquad = \big(\bar{w}_{xx}, \nu u_h'\big)_{\Omega_E} + \frac{1}{2}\big(\bar{w}_x, {u_h'}^2\big)_{\Omega_E} + \big(\bar{w}, f\big)_{\Omega_E} \quad \forall\, \bar{w} \in \bar{\mathscr{V}} \end{aligned} \tag{D.3}$$

Three-scale eddy viscosity model

Polynomial degree $p = 2$

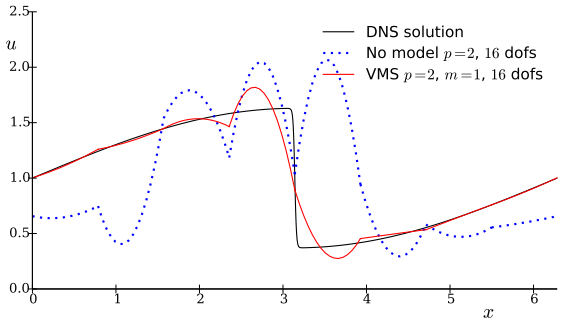

Fig. D.1: *Eddy viscosity VMS model, 16 degrees of freedom, $\nu_T/\nu = 11.2$.*

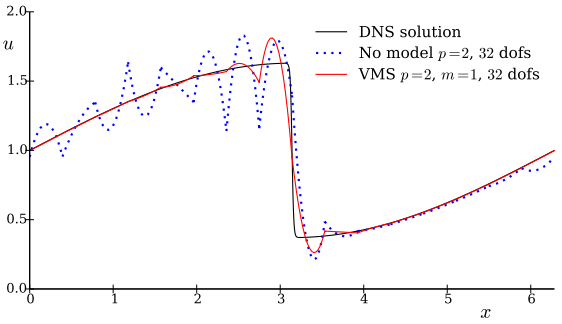

Fig. D.2: *Eddy viscosity VMS model, 32 degrees of freedom, $\nu_T/\nu = 4.86$.*

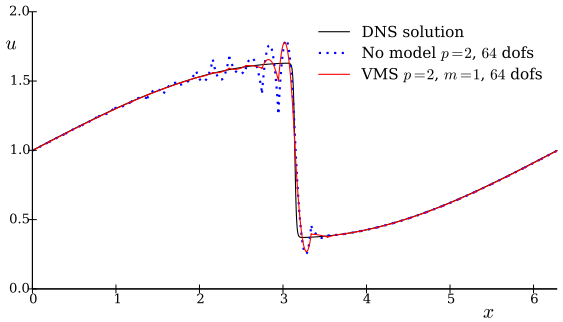

Fig. D.3: *Eddy viscosity VMS model, 64 degrees of freedom, $\nu_T/\nu = 1.80$.*

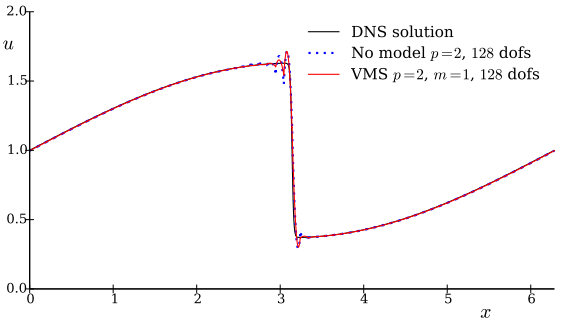

Fig. D.4: *Eddy viscosity VMS model, 128 degrees of freedom, $\nu_T/\nu = 0.480$.*

Polynomial degree $p = 4$

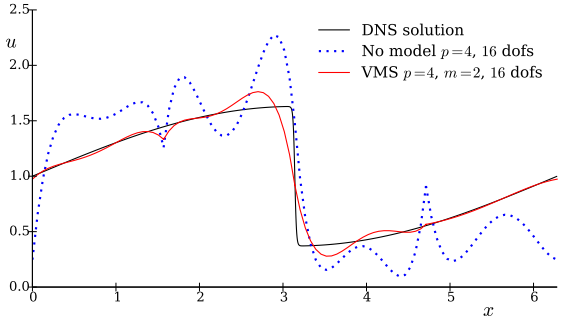

Fig. D.5: *Eddy viscosity VMS model, 16 degrees of freedom, $\nu_T/\nu = 11.2$.*

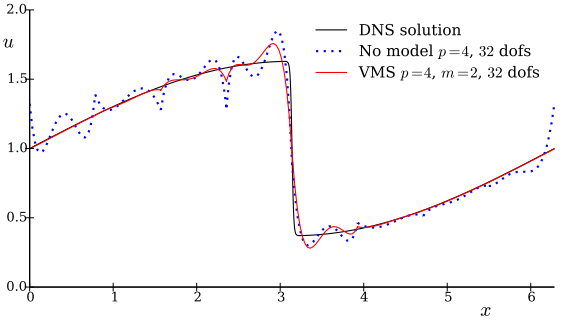

Fig. D.6: *Eddy viscosity VMS model, 32 degrees of freedom, $\nu_T/\nu = 4.86$.*

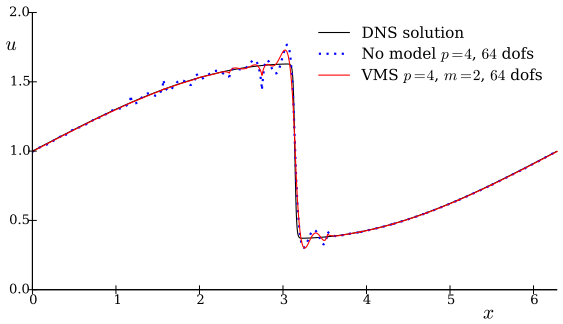

Fig. D.7: *Eddy viscosity VMS model, 64 degrees of freedom, $\nu_T/\nu = 1.80$.*

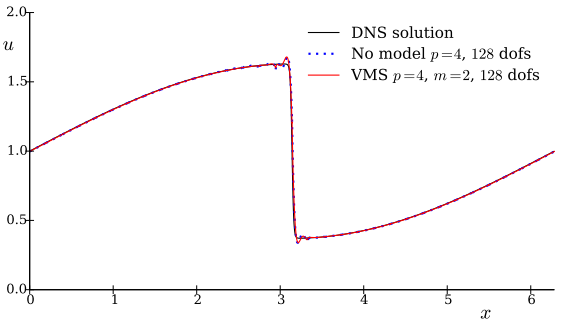

Fig. D.8: *Eddy viscosity VMS model, 128 degrees of freedom, $\nu_T/\nu = 0.480$.*

Polynomial degree $p = 8$

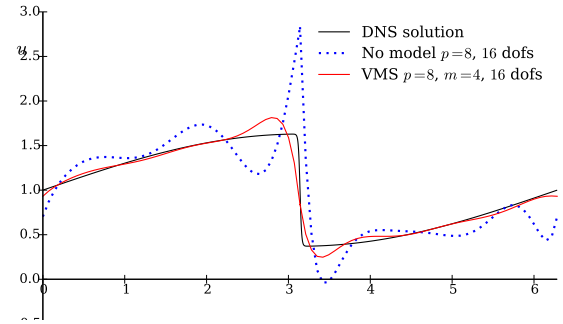

Fig. D.9: *Eddy viscosity VMS model, 16 degrees of freedom, $\nu_T/\nu = 11.2$.*

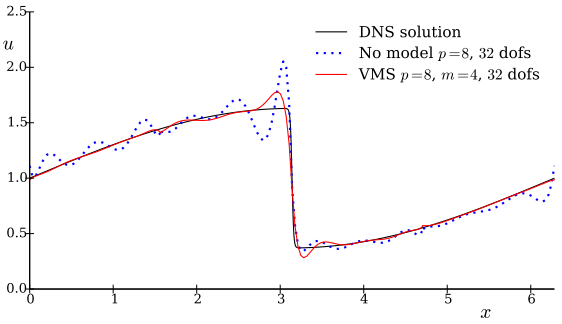

Fig. D.10: *Eddy viscosity VMS model, 32 degrees of freedom, $\nu_T/\nu = 4.86$.*

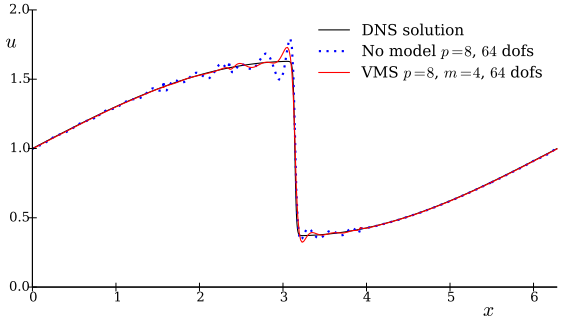

Fig. D.11: *Eddy viscosity VMS model, 64 degrees of freedom, $\nu_T/\nu = 1.80$.*

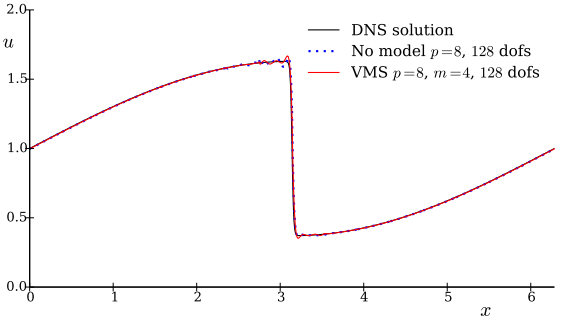

Fig. D.12: *Eddy viscosity VMS model, 128 degrees of freedom, $\nu_T/\nu = 0.480$.*

B-Spline based R-VMS model

Polynomial degree $p = 2$

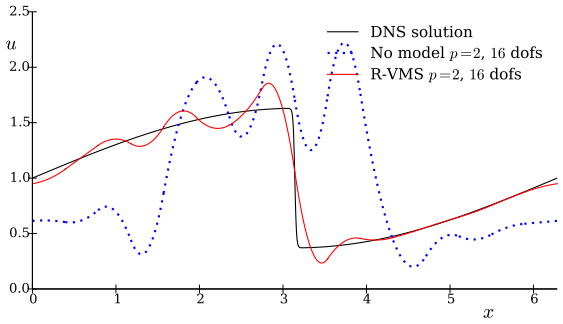

Fig. D.13: *B-spline R-VMS model, 16 degrees of freedom, $C_1 = 2$, $C_2 = 0.7$.*

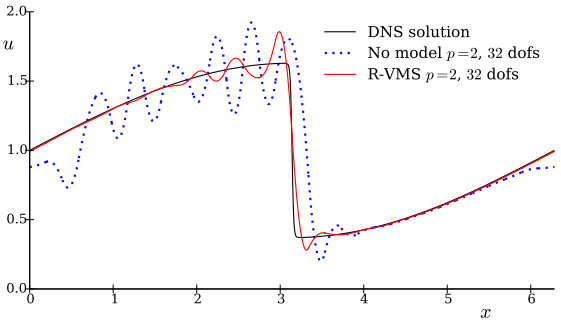

Fig. D.14: *B-spline R-VMS model, 32 degrees of freedom, $C_1 = 2$, $C_2 = 0.7$.*

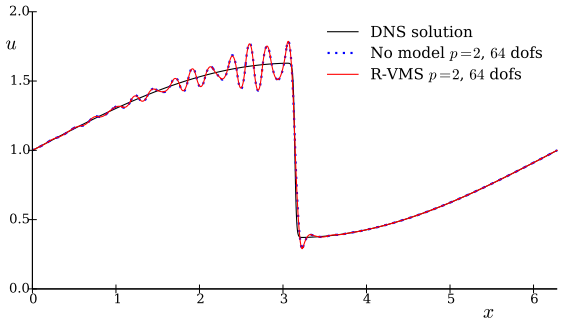

Fig. D.15: *B-spline R-VMS model, 64 degrees of freedom, $C_1 = 0.7$, $C_2 = 0.7$.*

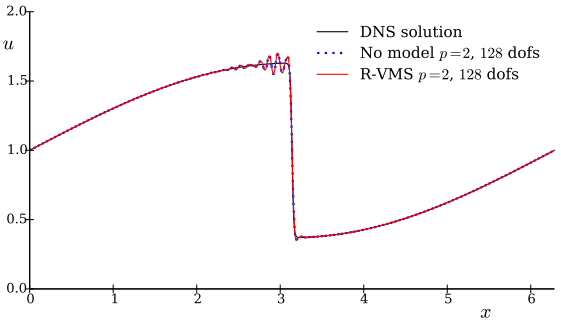

Fig. D.16: *B-spline R-VMS model, 128 degrees of freedom, $C_1 = 0.7$, $C_2 = 0.7$.*

Polynomial degree $p = 3$

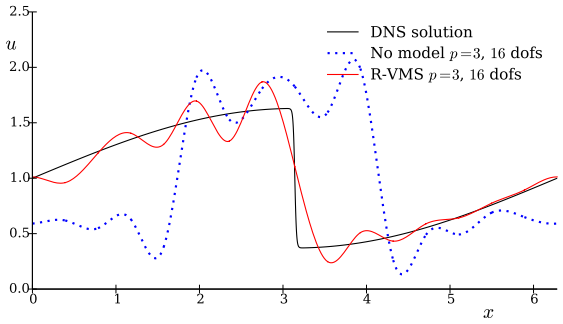

Fig. D.17: *B-spline R-VMS model, 16 degrees of freedom, $C_1 = 2$, $C_2 = 0.7$.*

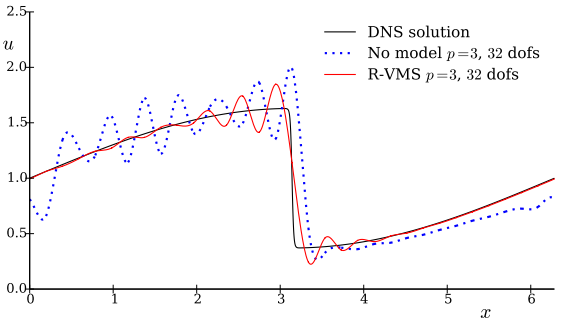

Fig. D.18: *B-spline R-VMS model, 32 degrees of freedom, $C_1 = 2$, $C_2 = 0.7$.*

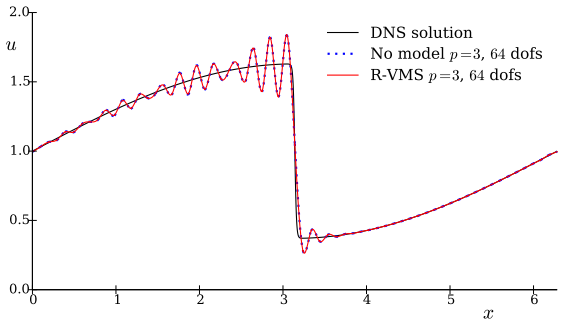

Fig. D.19: *B-spline R-VMS model, 64 degrees of freedom, $C_1 = 0.7$, $C_2 = 0.7$.*

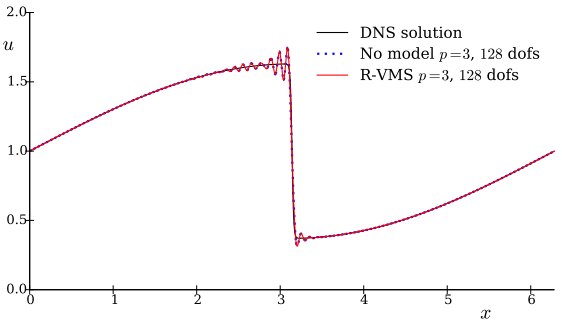

Fig. D.20: *B-spline R-VMS model, 128 degrees of freedom, $C_1 = 0.7$, $C_2 = 0.7$.*

Polynomial degree $p = 4$

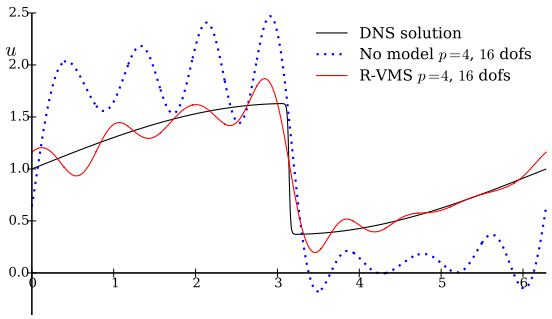

Fig. D.21: *B-spline R-VMS model, 16 degrees of freedom, $C_1 = 2$, $C_2 = 0.7$.*

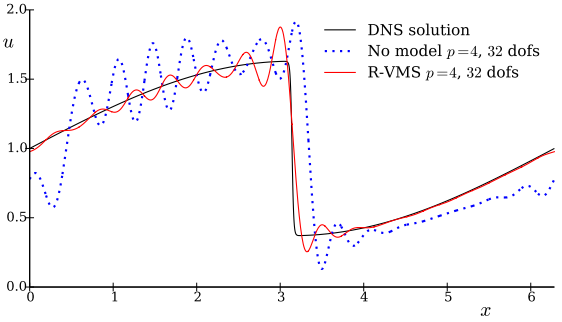

Fig. D.22: *B-spline R-VMS model, 32 degrees of freedom, $C_1 = 2$, $C_2 = 0.7$.*

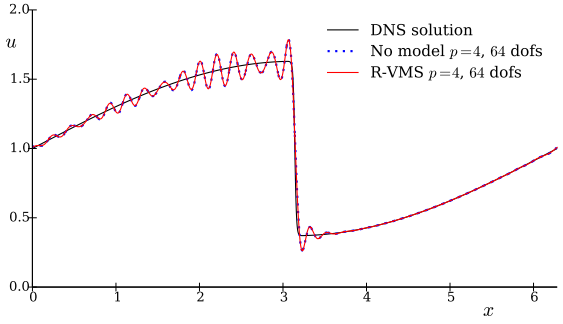

Fig. D.23: *B-spline R-VMS model, 64 degrees of freedom, $C_1 = 0.7$, $C_2 = 0.7$.*

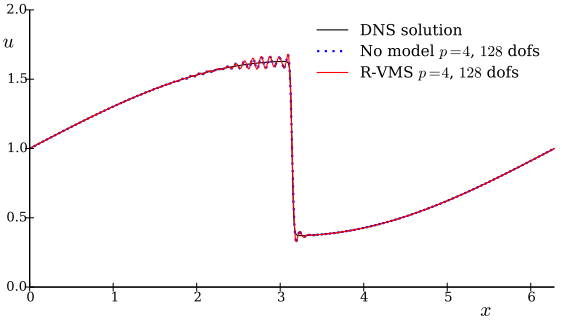

Fig. D.24: *B-spline R-VMS model, 128 degrees of freedom, $C_1 = 0.7$, $C_2 = 0.7$.*

DG-RVMS model

Polynomial degree $p = 2$

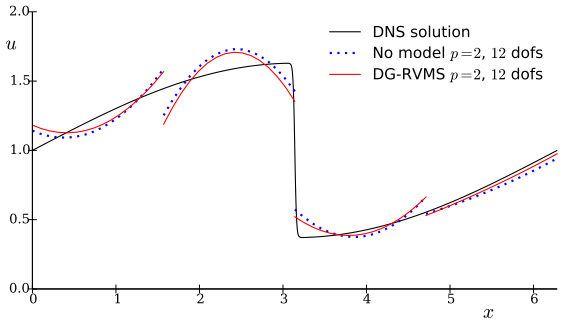

Fig. D.25: *DG-RVMS model, 12 degrees of freedom, $C_1 = 0.7$, $C_2 = 0.7$, $C_3 = 0.1$.*

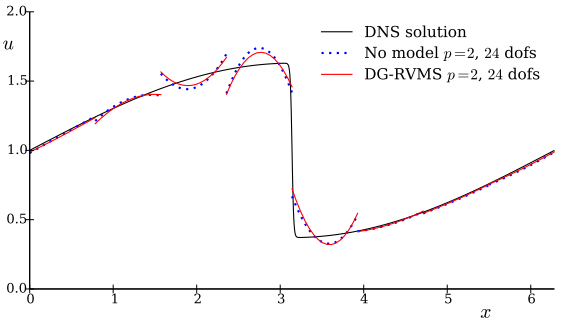

Fig. D.26: *DG-RVMS model, 24 degrees of freedom, $C_1 = 0.7$, $C_2 = 0.7$, $C_3 = 0.1$.*

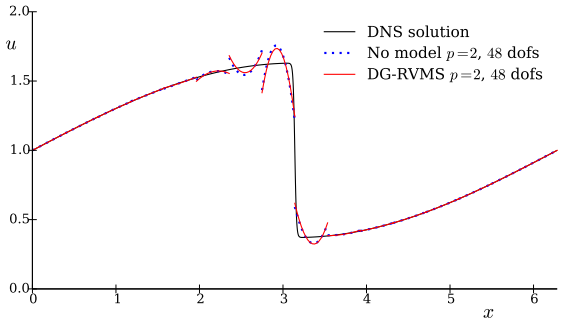

Fig. D.27: *DG-RVMS model, 48 degrees of freedom, $C_1 = 0.7$, $C_2 = 0.7$, $C_3 = 0.1$.*

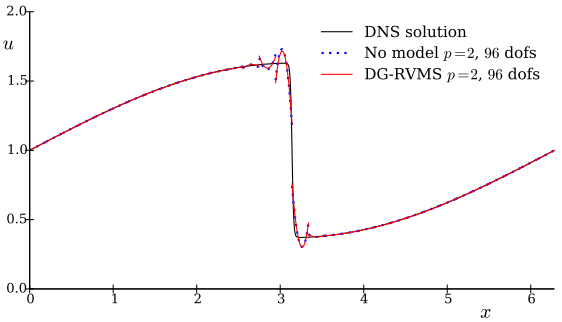

Fig. D.28: *DG-RVMS model, 96 degrees of freedom, $C_1 = 0.7$, $C_2 = 0.7$, $C_3 = 0.1$.*

Polynomial degree $p = 3$

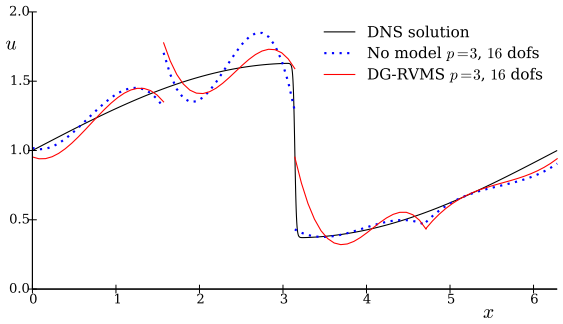

Fig. D.29: *DG-RVMS model, 16 degrees of freedom, $C_1 = 0.7$, $C_2 = 0.7$, $C_3 = 0.3$.*

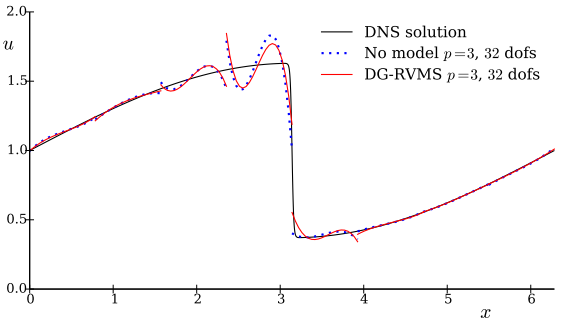

Fig. D.30: *DG-RVMS model, 32 degrees of freedom, $C_1 = 0.7$, $C_2 = 0.7$, $C_3 = 0.2$.*

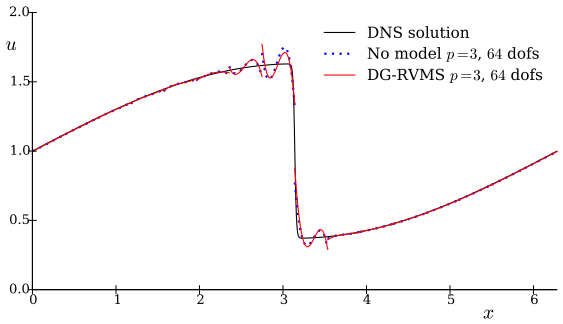

Fig. D.31: *DG-RVMS model, 64 degrees of freedom, $C_1 = 0.7$, $C_2 = 0.7$, $C_3 = 0.2$.*

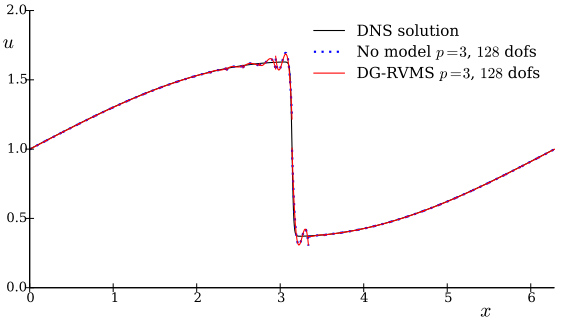

Fig. D.32: *DG-RVMS model, 128 degrees of freedom, $C_1 = 0.7$, $C_2 = 0.7$, $C_3 = 0.1$.*

Polynomial degree $p = 4$

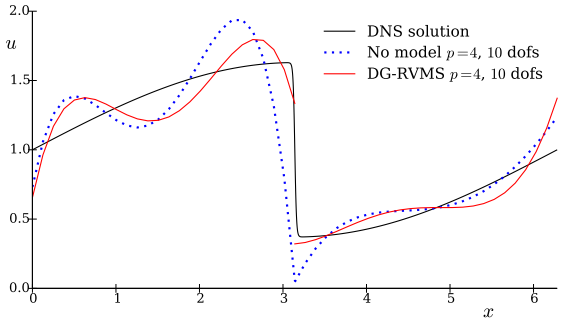

Fig. D.33: *DG-RVMS model, 10 degrees of freedom, $C_1 = 0.7$, $C_2 = 0.7$, $C_3 = 0.3$.*

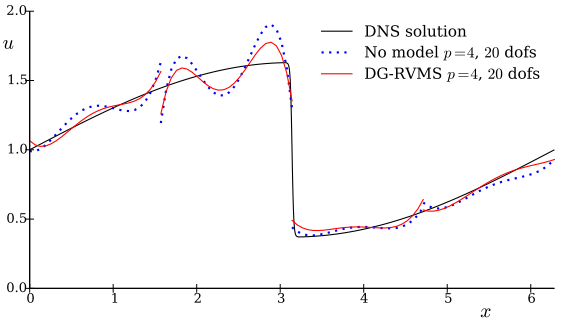

Fig. D.34: *DG-RVMS model, 20 degrees of freedom, $C_1 = 0.7$, $C_2 = 0.7$, $C_3 = 0.3$.*

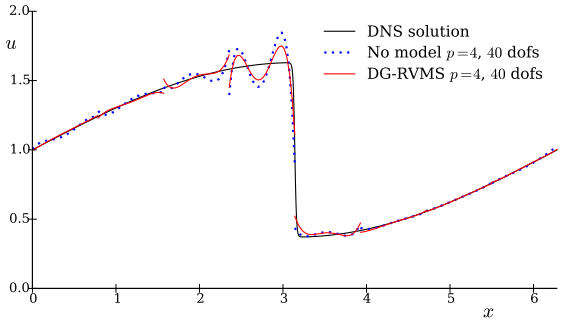

Fig. D.35: *DG-RVMS model, 40 degrees of freedom, $C_1 = 0.7$, $C_2 = 0.7$, $C_3 = 0.3$.*

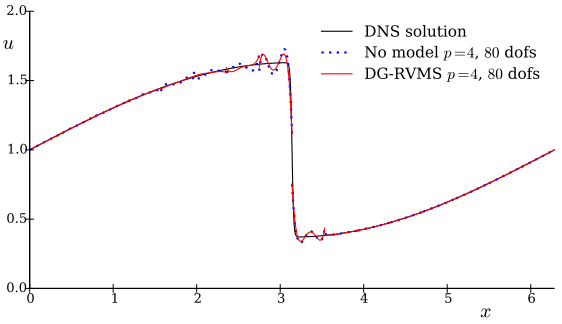

Fig. D.36: *DG-RVMS model, 80 degrees of freedom, $C_1 = 0.7$, $C_2 = 0.7$, $C_3 = 0.3$.*